AGH UNIVERSITY OF KRAKOW

FIELD OF SCIENCE ENGINEERING AND TECHNOLOGY

SCIENTIFIC DISCIPLINE MATERIALS ENGINEERING

DOCTORAL THESIS

Design and investigation of physical properties of the components for all-oxide photovoltaic cells

Author: Katarzyna Ungeheuer

First supervisor: Konstanty W. Marszałek, PhD, DSc, Prof. AGH
Assisting supervisor: Krzysztof Mars, PhD

Completed in: Faculty of Computer Science, Electronics, and Telecommunications

Kraków, 2024

Firstly, I want to thank my supervisors prof. Konstanty Marszałek and dr Krzysztof Mars for all the work and good advice through all my doctoral studies. I wish to thank my coworkers Janusz Rybak, Katarzyna Dyndał, Gabriela Lewińska, and Jerzy Sanetra for all the help and good advice they gave me. I would like to thank for successful collaboration: Artur Rydosz, Jerzy Sokulski, Edward Kusior from Faculty of Computer Science, Electronics and Telecommunications; Piotr Jeleń and Maciej Sitarz from Faculty of Materials Engineering and Ceramics; Marzena Mitura-Nowak, Marcin Perzanowski and Marta Marszałek from Institie of Nuclear Physics Polish Academy of Sciences; Rafał Knura at CBRTP S.A.; Robert Socha from Jerzy Haber Institute of Catalysis and Surface Chemistry Polish Academy of Sciences; Aurelian C. Galca and Amelia E. Bocirnea from National Institute of Materials Physiscs in Magurele, Romania. Finally, I want to especially thank my fiancé , Alex, for constant support and motivation, and my parents for providing me with this opportunity of great education.

Abstract

This work addresses the design and development of an all-oxide solar cell. Proposed cell used copper oxide as absorber layer and zinc oxide as window layer. The electrodes are aluminium as rear electrode and aluminium doped zinc oxide (AZO) or indium tin oxide (ITO) as front transparent electrode.

A central objective is to enhance the electrical and optical properties of copper oxide thin films by doping with chromium. To achieve this thin films deposited via reactive magnetron sputtering were implanted with chromium ions and then annealed. The work presents studies of implanted CuO, Cu_2O and Cu_4O_3, where the first oxide is examined in more detail. To assess theoretically the ion implantation process simulations were done in Stopping and Range of Ions in Matter (SRIM) software and using Density Funcional Theory (DFT). The main conclusion from the conducted research is that Cr ion implantation reduces the absorption and conductivity of the layers, while annealing restores their values. For an implantation energy of 10 keV and a dose of $1x10^{14}$ cm^{-2}, the sample after annealing had better properties than the annealed non-implanted layer, confirming the desired effect of doping CuO with chromium.

The use of X-ray photoelectron spectroscopy (XPS) allowed for the observation of interesting behaviour of Cu_2O layers. The layer after annealing in Ar atmosphere exhibited a surface dominated by CuO, while samples after implantation retained a surface composed of Cu_2O. This phenomenon may prove useful in the fabrication of solar cells with this oxide as the absorber layer, as researchers have previously pointed out the issue of Cu_2O surface contamination with CuO, which reduces the efficiency of the fabricated cells. Stabilising the Cu_2O phase could be a solution to this problem.

Another topic addressed in this work is the resistance of materials to conditions in space environment, specifically the corpuscular part of cosmic radiation. Thin films of CuO, AZO and ITO were irradiated with a proton beam and then characterised. Studies of the samples before and after irradiation revealed no changes in the structural properties of any of the materials. For ITO, no changes were observed in the optical and electrical properties. However, for AZO, the transmission decreased, and the conductivity of the layer increased. XPS analysis suggested that this rise in conductivity might be due to an increased number of defects after irradiation. The CuO layer after irradiation had lower light absorption and worse surface conductivity. The proton dose used

in the experiment corresponds to several hundred years of material exposure in low Earth orbit conditions. Therefore, the main conclusion is that the tested materials exhibit good resistance to proton radiation, indicating them as suitable candidates for future space applications.

To create a working solar cell forty devices were prepared, out of which two exhibited a diode-like current-voltage characteristic. Fabricating solar cells with good photovoltaic properties requires further optimisation of the layer deposition technology, particularly in terms of sample storage and surface condition control between successive layer deposition processes.

Streszczenie

Praca ta dotyczy projektowania i przygotowania ogniwa słonecznego wykonanego na bazie materiałów tlenkowych. Proponowane ogniwo wykorzystuje tlenek miedzi jako warstwę absorbującą oraz tlenek cynku jako warstwę okienną. Elektrody to aluminium jako tylna elektroda oraz tlenek cynku domieszkowany aluminium (AZO) lub tlenek indu i cyny (ITO) jako przezroczysta elektroda przednia.

Głównym zadaniem jest poprawa właściwości elektrycznych i optycznych cienkich warstw tlenku miedzi poprzez domieszkowanie chromem. W tym celu cienkie warstwy, osadzone metodą reaktywnego rozpylania magnetronowego, zostały implantowane jonami chromu, a następnie wygrzewane. Praca przedstawia badania nad implantowanymi warstwami CuO, Cu_2O i Cu_4O_3, z których pierwszy tlenek został przeanalizowany bardziej szczegółowo. W celu teoretycznej oceny procesu implantacji jonów wykonano symulacje w programie Stopping and Range of Ions in Matter (SRIM) oraz przy użyciu Teorii Funkcjonalu Gęstości (DFT). Główny wniosek z przeprowadzonych badań jest taki, że implantacja jonami chromu zmniejsza absorpcję i przewodność warstw, natomiast wygrzewanie przywraca te właściwości. Dla energii implantacji wynoszącej 10 keV i dawki $1x10^{14}$ cm^{-2} próbka po wgrzewaniu miała lepsze właściwości niż wygrzewana warstwa nieimplantowana, co potwierdza pożądany efekt domieszkowania CuO chromem.

Zastosowanie rentgenowskiej spektroskopii fotoelektronów (XPS) pozwoliło zaobserwować interesujące zachowanie warstw Cu_2O. Warstwa po wygrzewaniu w atmosferze argonu wykazała powierzchnię zdominowaną przez fazę CuO, podczas gdy próbki po implantacji zachowały powierzchnię składającą się z fazy Cu_2O. Zjawisko to może być użyteczne przy produkcji ogniw słonecznych z tym tlenkiem jako warstwą absorbującą, ponieważ badacze wcześniej wskazywali na problem zanieczyszczenia powierzchni Cu_2O przez CuO, co zmniejsza wydajność wytworzonych ogniw. Stabilizacja fazy Cu_2O mogłaby stanowić rozwiązanie tego problemu.

Kolejnym zagadnieniem poruszonym w tej pracy jest odporność materiałów na warunki środowiska kosmicznego, a konkretnie na korpuskularną część promieniowania kosmicznego. Cienkie warstwy CuO, AZO i ITO zostały napromieniowane wiązką protonów, a następnie scharakteryzowane. Badania próbek przed i po napromieniowaniu nie wykazały zmian w strukturze żadnego z materiałów. W przypadku ITO nie zaobserwowano zmian w właściwościach optycznych i elektrycznych. Jednak w przypadku AZO transmisja zmalała, a przewodność warstwy

wzrosła. Analiza XPS zasugerowała, że wzrost ten może wynikać ze zwiększonej liczby defektów po napromieniowaniu. Warstwa CuO po napromieniowaniu wykazała niższą absorpcję światła i gorszą przewodność powierzchniową. Dawka protonów użyta w eksperymencie odpowiada kilkusetletniej ekspozycji materiału na warunki na niskiej orbicie okołoziemskiej. Główny wniosek tej części badań jest taki, że badane materiały wykazują dobrą odporność na promieniowanie protonowe, co czyni je odpowiednimi kandydatami do przyszłych zastosowań w kosmosie.

Aby stworzyć działające ogniwo słoneczne, przygotowano czterdzieści układów, z których dwa wykazały charakterystykę prądowo-napięciową typową dla diody. Wytwarzanie ogniw słonecznych o dobrych właściwościach fotowoltaicznych wymaga dalszej optymalizacji technologii osadzania warstw, szczególnie pod względem przechowywania próbek i kontroli stanu powierzchni między kolejnymi procesami osadzania warstw.

Contents

Motivation and aim of work **2**

1 Introduction **3**

2 Theoretical background and all-oxide solar cells state of the art **5**

2.1 Photovoltaic cells generations 5

2.2 The parameters of a photovoltaic cell 9

2.3 All-oxide solar cells 11

2.4 Copper oxides 15

2.5 Ion implantation 21

2.6 Photovoltaics in space 24

3 Thin films deposition **29**

3.1 Reactive magnetron sputtering - copper oxides thin films deposition 29

3.2 Atomic Layer Deposition - transparent electrode made of Al-doped zinc oxide . . . 31

3.3 DC magnetron sputtering - ZnO thin films deposition 32

3.4 Thermal evaporation of metallic Al electrode 32

4 Investigation of copper oxide thin films modified by Cr ion implantation **33**

4.1 Ion implantation 33

4.2 SRIM simulations 33

4.3 CuO 37

4.3.1 Structural properties 37

4.3.2 Density of states calculation with Density Functional Theory 42

4.3.3 Optical properties 44

4.3.4 Surface homogeneity and chemical states 52

4.3.5 Electrical properties 61

4.3.6 Depth profiling 62

4.4 Cu_2O and Cu_4O_3 66

4.4.1 Structural properties 66

4.4.2 Optical properties 69

4.4.3 Surface homogeneity . . . 75
4.4.4 Surface chemical state of Cu_2O . . . 79
4.5 Conclusions . . . 81

5 Influence of proton irradiation - simulation of space conditions 83
5.1 Proton irradiation experiment . . . 84
5.2 CuO . . . 84
5.2.1 Structural properties . . . 84
5.2.2 Optical properties . . . 85
5.2.3 Electrical properties . . . 87
5.2.4 Surface chemical state . . . 87
5.3 Transparent conductive oxides ITO and AZO . . . 90
5.3.1 Structural properties . . . 90
5.3.2 Optical properties . . . 90
5.3.3 Surface homogeneity . . . 93
5.3.4 Electrical properties . . . 97
5.3.5 Surface chemical state . . . 97
5.4 Conclusions . . . 99

6 Design of all-oxide photovoltaic systems 101
6.1 Solar cell system preparation . . . 101
6.2 Conclusions . . . 104

7 Summary 105

Bibliography 109

List of publications 125

List of Figures 125

List of Tables 130

Motivation and aim of work

The world is now more in need of new materials and technologies for renewable energy production. While photovoltaic energy generation, particularly silicon-based, is well-developed and widely commercialised, there are other materials beyond silicon that can be utilized in photovoltaic devices. Research into new materials or modifications of existing ones will expand our understanding and lead to innovative photovoltaic technologies. These alternatives, such as thin-film photovoltaic cells, offer advantages like lower weight and reduced material consumption compared to crystalline silicon. In the future, thin-film solar cells could be integrated into everyday life, enabling solar energy harvesting through flexible substrates embedded in clothing, vehicles, and outdoor equipment. Thin films can often be deposited using cost-effective wet methods, though these are less scalable, whereas vacuum deposition methods, which are scalable and widely used in industries like glass manufacturing, offer better prospects. Choosing oxide-based thin films as functional layers enables the use of non-toxic, inexpensive source materials that offer greater stability compared to perovskites or organic compounds. However, the performance of oxide-based thin-film photovoltaics remains limited, and further research is essential to improve their efficiency and realise their full potential.

This work focuses on the study of metal oxide thin films essential for constructing an all-oxide solar cell. The primary emphasis is on the modification of copper oxide thin films, specifically those used as absorber layers in photovoltaic systems. Copper oxides, including CuO, Cu_2O, and Cu_4O_3, were doped with chromium through the ion implantation method. Detailed studies were conducted primarily on CuO thin films, identified as the most promising due to its superior stability and optimised deposition parameters. The objective is to enhance the optical and electrical properties of CuO and Cu_2O thin films through Cr ion implantation.

Additionally, the research includes a simulation of space environment and its impact on materials used in space applications. In this study, thin films of two transparent conductive oxides, along with a CuO film, were irradiated with proton beam. The aim of this study was to demonstrate that these materials possess good resilience to irradiation, making them viable candidates for future space applications.

The final task task is preparation of a working solar cell based on oxide materials. The design incorporates a transparent electrode, copper oxide as absorber layer, zinc oxide as window layer and aluminium as rear electrode.

The main theses of this work are:

- chromium implantation into copper oxide thin films and subsequent annealing improves its optical and electrical properties.
- the distribution of chromium in implanted thin film has a peak, while after annealing the distribution is uniform.
- CuO, ITO, and AZO thin films after irradiation with 226.5 MeV proton beam retain their optical and electrical properties.

Chapter 1

Introduction

The development of renewable energy sources requires search for new solutions and materials. Currently, the dominant technology is silicon-based solar cells, but the use of thin-film materials can provide savings in production, both in terms of raw material and energy consumption. One of the promising candidates among thin film technologies are all-oxide solar cells, which can be made using non-toxic and abundant materials. Tough, the performance of all-oxide solar cells has been poor so far, and one of many possible ways of improvement is modification of functional layers in the device. Copper oxides are widely used as absorber layer and to achieve better photovoltaic performance they should be modified to improve electrical properties with remaining high absorption of this material. Thin film solar cell due to their small weight are a good candidate for space applications. Any material used in outer space must be resilient to the specific space environment, and one way to simulate its influence is using proton irradiation.

The thesis begins with a theoretical overview and a review of the current state of research. The chapter discusses photovoltaic technologies, fundamental photovoltaic principles, and the latest advances in all-oxide solar cells. A detailed description of copper oxides follows, highlighting their material properties. The chapter also reviews the ion implantation method, its impact on materials, and finally approaches for simulating the effects of space conditions especially proton irradiation.

The third chapter describes the deposition methods used for all studied samples, detailing specific deposition parameters. Copper oxide samples were prepared by reactive magnetron sputtering, ZnO films for the solar cell were deposited via DC magnetron sputtering, Al electrode was thermally evaporated, and AZO films were prepared with atomic layer deposition methods.

In the fourth chapter, the properties of chromium-implanted copper oxide films are examined. The samples were characterization by X-ray diffraction (XRD), UV-Vis spectrophotometry, spectroscopic ellipsometry, four-point probe sheet resistance measurement, atomic force microscopy (AFM), Raman spectroscopy, infrared spectroscopy, X-ray photoelectron spectroscopy (XPS) and secondary neutral mass spectrometry (SNMS). Chosen CuO and Cu_2O samples were characterised also after annealing for 6 hours at 400 °C.

The fifh chapter presents studies on the effects of proton irradiation on CuO, AZO, and ITO films to simulate space environment influence. The beam was of 226.5 MeV energy and $1x10^{11}$ cm^{-2} fluence was used. Before and post-irradiation characterisation included XRD, spectroscopic ellipsometry, spectrophotometry, XPS, Raman spectroscopy and scanning electron microscopy (SEM).

The sixth chapter describes the preparation of the solar cell samples and addresses issues encountered during current-voltage measurements. The final chapter summarizes key findings and conclusions of the research, highlighting the main insights gained from this work.

This research was performed at the Institute of Electronics, Faculty of Computer Science, Electronics and Telecommunications, AGH University of Krakow. Presented studies are result of collaboration with many institutions, specifically:

- Faculty of Materials Science and Ceramics - Raman spectrocopy, FTIR, SEM observations, AFM, XRD
- Henryk Niewodniczański Institute of Nuclear Physics, Polish Academy of Sciences, Kraków - ion implantation, XRD measurements, proton irradiation
- Jerzy Haber Institute of Catalysis and Surface Chemistry, Polish Academy of Sciences, Kraków - ZnO films deposition
- National Institute of Materials Physics, Bucarest, Romania - XPS measurements, XRD, SEM, Raman, spectroscopic ellipsometry with VASE
- CBRTP S.A. - AZO films deposition with ALD
- Faculty of Metals Engineering and Industrial Computer Science, AGH University of Krakow - SEM observations
- ATOMKI Institute for Nuclear Research, Hungarian Academy of Sciences, Debrecen - SNMS measurement

Chapter 2

Theoretical background and all-oxide solar cells state of the art

2.1 Photovoltaic cells generations

Human activity and rapid civilizational development in the last two centuries have caused excessive emissions of greenhouse gases into the atmosphere, which lead to global warming [1]. This process is associated with the destabilisation of our known climate and the deterioration of living conditions on our planet, which we are experiencing more and more nowadays [2]. One of the main sources of the greenhouse gases is the burning of fossil fuels that are used especially for energy production but also synthetic materials production. The fossil fuels are limited in supply, thus being a non-renewable source of energy. Electricity production is currently largely based on the use of non-renewable energy sources, while the needs for electricity generation are growing along with the increasing number of people on Earth [3]. It is projected that in 2050, electricity production will be 44.26 PWh (which is 10^{15} Wh), of which nearly 50% will be renewable sources, and renewable energy sources will surpass the energy produced from coal in 2025. There is therefore a need to search for new and develop existing renewable and more environmentally friendly sources of energy.

While in 2023 the most important renewable energy technologies were hydropower, wind and photovoltaics, which contributed 14.2%, 7.8% and 5.4% of total energy production, respectively [4]. In 2021 the share of electricity production by photovoltaics was 3.6% worldwide, so there is an ongoing growth of the market. It is estimated that energy produced by photovoltaic cells will surpass energy produced from wind around 2030 [4]. Photovoltaic technology based on Si-wafer accounted for more than 95% of the total production, of which 84% is mono-crystalline silicon [5]. The market consists mostly of rooftop installations and industrial photovoltaic farms, which are more and more common, e.g. in Europe. Another possible application of solar cells is small-scale personal products, like cells integrated with clothing, house and office appliances or sports and

outdoor products. Such applications require cells based on materials that are more mechanically stable than silicon and can be used on elastic substrates. A great solution is to use thin film solar cells, where some materials have already been developed, but there is much more to achieve with new technologies that use cheaper and more abundant materials.

Types of photovoltaic cells technologies are classified according to the chronological order in which they appeared and on technological similarities. We can distinguish the so-called generations of photovoltaic cells: the first generation, to which belong cells based on mono- and polycrystalline silicon, in the second generation there are thin-film cells, the third generation is the latest technologies that are under research, e.g. organic, perovskite or oxide based solar cells. The division of photovoltaic cell technologies into generations is shown in Figure 2.1.

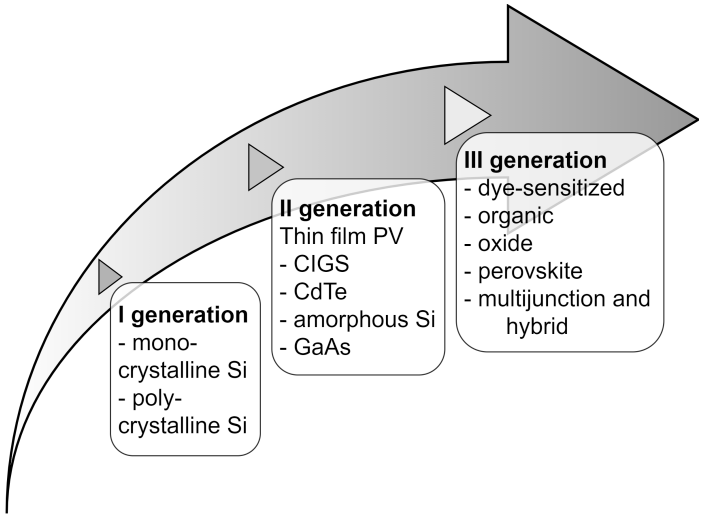

Figure 2.1. Generations of photovoltaic technologies [3]

Although the photovoltaic effect has been first observed in materials other than silicon, it is silicon-based cells that constitute the first generation and dominate the photovoltaic market. Silicon is a semiconductor with an energy gap of 1.12 eV [6]. This element owes its wide application to its semiconductor properties and the possibility of relatively easy doping, which allows for the production of p-type and n-type semiconductors and then p-n junctions, and further various electronic elements, such as diodes and transistors. An important factor of the wide use of silicon is the Czochralski method used to grow monocrystals, developed by a Polish scientist in XXth century.

The working of most solar cells is based on the existence of a p-n junction, which means that a solar cell is a diode. To prepare a solar cell, silicon wafers are doped in such a way that a 180-300 μm thick p-type layer is obtained, followed by an approximately 2 μm thick n-type silicon layer. When p-type and n-type materials contact, they form a p-n junction. At this junction, charge carriers diffuse towards the region with fewer carriers of each type: electrons move into the p-type material, and holes into the n-type material, where they recombine with counterpart charge

carriers. Thus, a depletion region is created which is almost devoid of free charge carriers and its existence results in a built-in voltage at the junction. The energy levels in the materials align so that the Fermi level remains continuous, as illustrated in the energy band diagram in Figure 2.2a.

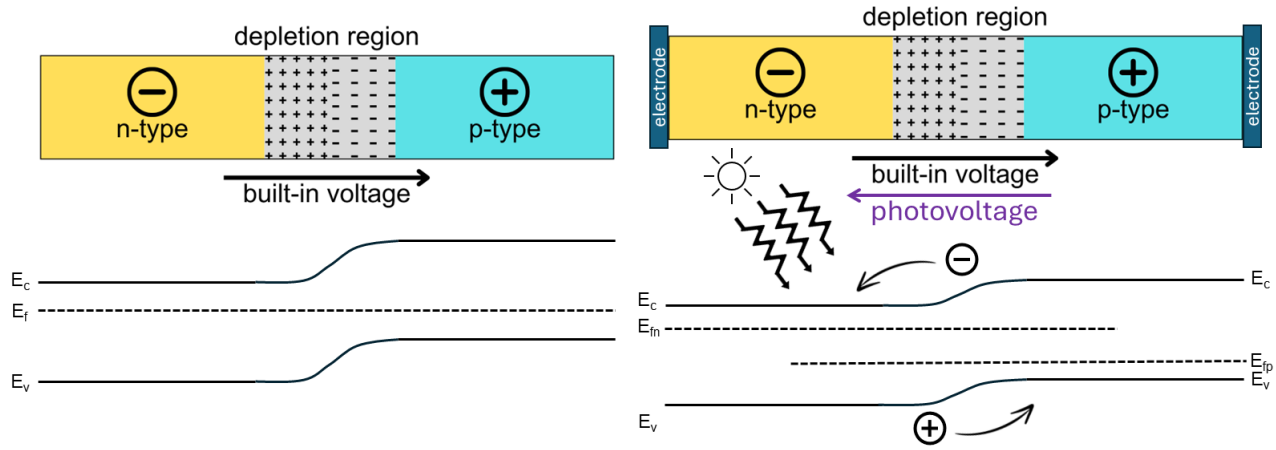

(a) (b)

Figure 2.2. Band gap diagram of p-n junction (a) in dark; (b) after illumination. *E*c - conduction band, E_v - valence band, E_f - fermi energy level, E_{fp} - quasi-Fermi level of p-type semiconductor, E_{fn} - quasi-Fermi level of n-type semiconductor.

When photons strike the material, their energy can be absorbed by electrons, causing their excitation and leaving behind holes. These generated charge carriers are then separated at the junction and transported to the electrodes. The voltage created between the anode and cathode, known as the photovoltage, opposes the built-in voltage. This photovoltage, combined with the electron flow in the external circuit, produces usable electrical energy [7].

A simple scheme of silicon solar cell is presented in Figure 2.3a. To improve the performance of silicon based solar cells, many approaches are applied. The n-type layer is often modified by etching to obtain a textured surface that reduces the reflectance of light from the solar cell surface. Another common modification is deposition of anti-reflective (AR) coatings which allow more light to reach the active layer of the cell. The industry developed and still works on many improvements of silicon solar cell construction. Some technologies worth attention are: PERC (Passivated Emitter Rear Cell) where an additional passivating layer at the back of the cell ensures less recombination, protection from corrosion and reflects radiation back into the cell; HIT (Heterojunction with Intrinsic Thin layer) which combines crystalline and amorphous silicon, this technology enables bifaciality of modules, improves efficiency and durability of modules; PERL (Passivated Emitter Rear Locally-diffused) which improved the efficiency and simplified production processes [8]. These developments are reaching the limit of possible energy conversion efficiency using sili-

con as base material. Now a lot of research is focused on creating hybrid cells, where e.g. using a perovskite layer on top of silicon can enable even higher efficiency [6].

Other technologies use different materials to create a p-n junction. In the second generation of photovoltaics, generation of thin film cells, technologies based on following materials are used: CIGS (copper indium galium selenide), CdTe (cadmium telluride), a-Si (amorphous silicon). Modules from these technologies use less material for production than first generation solar cells, and as they consist of thin film materials, they can be deposited on flexible substrates. CIGS is a compound that has high absorption coefficient, a 1µm layer results with the same light absorption as a 100 µm silicon layer [9]. With changing the amount of gallium in $CuIn_{1-x}Ga_xSe_2$ the band gap can be changed from 1 eV to 1.7 eV. The n-type layer, called window layer is usually CdS, a transparent electrode is at the top of CIGS cell, it can be ZnO:Al or ITO (Figure 2.3b) [10]. CdTe also shows very high absorption coefficient, it has band gap of 1.45 eV which is favourable for photovoltaic application. A typical configuration of a CdTe solar cell is presented in Figure 2.3c [11]. Both of these technologies are used in industry, where their main disadvantage is the toxicity of cadmium, which complicates production and more importantly the disposal of old modules.

Modules that are based on a-Si use multilayered p-i-n or n-i-p configuration. Amorphous silicon has unordered crystal structure, it can be produced with simpler and less expensive methods than crystalline silicon. Although this form of silicon has higher band gap (1.7 eV for a-Si, 1.1 eV for c-Si), it shows higher absorption than crystalline counterpart [12]. A simple p-i-n structure of a-Si cell is presented in Figure 2.3d.

The third generation of photovoltaic technologies is also called the emerging technologies. Here we can distinguish organic, perovskite, dye-sensitised, quantum dot, and oxide photovoltaics. The first two are being extensively developed by scientists in recent years. The National Renewable Energy Laboratory gathers information about the best obtained efficiency of solar cell in different technologies, and publish a chart of these achievements every year since 1976. The chart from 2024 is presented in Figure 2.4. The emerging photovoltaics show the most rapid increase of obtained efficiency, the organic photovoltaics had considerable leaps in performance in 2011 and 2019, current best efficiency is 19.2%. The first cell based on perovskite materials was reported in 2013 and the research on these materials, and the supporting layers has been going on since. The best current efficiency of perovskite solar cell is 26.1%. Though not distinguished as much, solar cell based only on inorganic materials, especially oxide thin films are also of interest of scientists, recently even more [13]. Further details on this type of solar cell can be found in section 2.3.

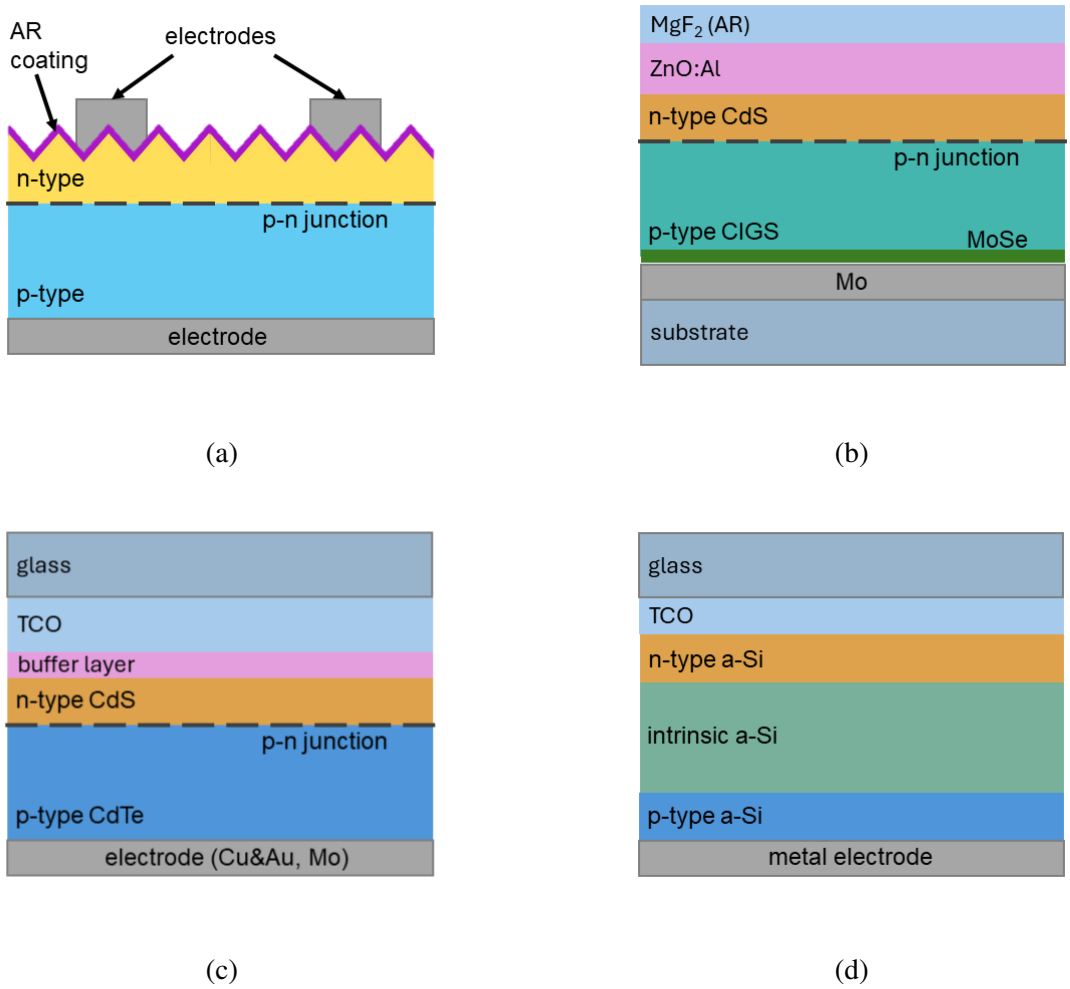

Figure 2.3. Structures of typical photovoltaic cells based on (a) crystalline Si, (b) copper indium gallium selenide (CIGS), (c) cadmium telluride (CdTe), and (d) amorphous Si.

2.2 The parameters of a photovoltaic cell

Solar cell performance is characterised with a few parameters:

- fill factor FF,
- short circuit current I_{SC},
- open circuit voltage V_{OC}
- efficiency η,
- current of maximum power point I_{mpp},
- voltage of maximum power point V_{mpp}.

In Figure 2.5 all these parameters are marked on an example of a solar cell's current-voltage characteristic.

The fill factor parameter is defined as in equation 2.1 and its unit is %.

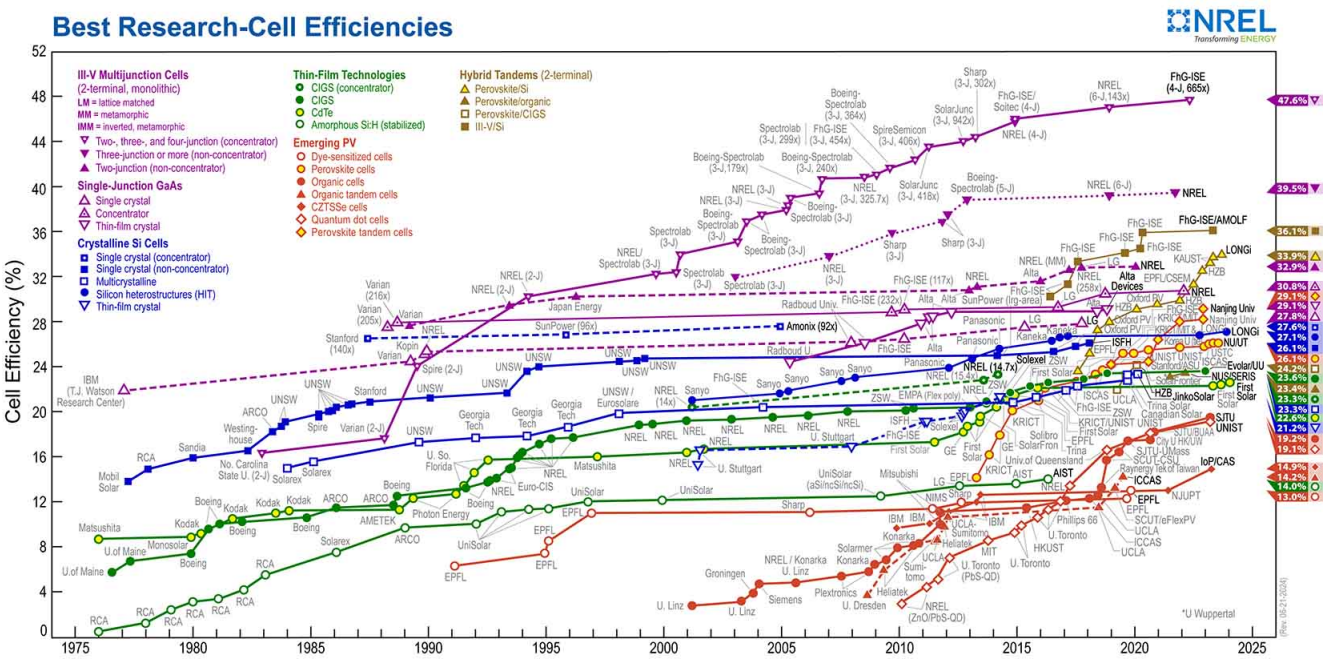

Figure 2.4. Best research-cell efficiency chart by National Renewable Energy Laboratory from 2024. This plot is courtesy of the National Renewable Energy Laboratory, Golden, CO.

$$FF = \frac{I_{mpp}V_{mpp}}{I_{sc}V_{oc}} \tag{2.1}$$

Efficiency of a solar cell is calculated as in equation 2.2, with unit of % as well.

$$\eta = \frac{I_{mpp}V_{mpp}}{P_{in}} = \frac{I_{sc}V_{oc}FF}{P_{in}} \tag{2.2}$$

where P_{in} is the incident radiation power.

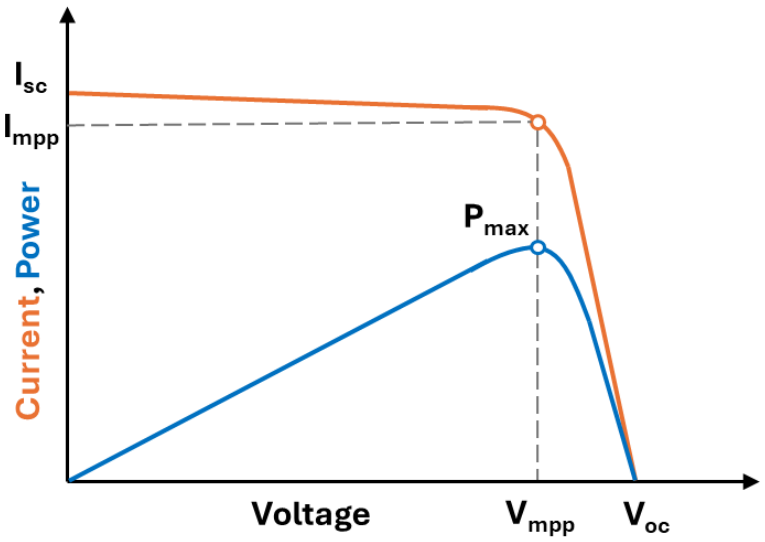

Figure 2.5. Current-voltage and power-voltage curves of a solar cell with marked maximum power point and basic parameters: I_{SC}, V_{OC}, I_{mpp}, V_{mpp}.

To compare different cells, and modules Standard Test Conditions (STC) have been developed [14]. These conditions are as follow:

- illumination intensity: 1000 W/m^2,
- light spectrum: AM1.5 solar spectrum as defined by IEC 60904-3,
- temperature of device during measurement: 25°C.

2.3 All-oxide solar cells

The evolution of photovoltaic technology is driven by the need for high-efficiency, cost-effective, and environmentally sustainable solar cells. Traditional silicon-based solar cells and advanced multijunction cells have achieved remarkable efficiencies, but they often come with significant drawbacks in terms of cost and environmental impact. Production of crystalline silicon consumes a lot of energy, CdTe uses toxic cadmium, CIGS low abundant indium and the now rapidly evolving perovskite and organic photovoltaics are unstable due to weak immunity to temperature and humidity. All-oxide solar cells present a promising alternative by leveraging oxide materials known for their stability, eco-friendliness, and scalability.

It is important to say that oxides are already used in electronics, in photovoltaics as well. Oxides in solar cells can be found as layers that enable or improve the transport of electrons or holes, as part of conductive electrodes, including transparent ones, and finally as an absorbing layer that facilitates the photon to electron energy conversion [15] [16].

All-oxide solar cells utilise a variety of metal oxides with different electronic properties to form the core components of the device. These materials include wide band gap semiconductors like zinc oxide (ZnO) and titanium dioxide (TiO_2), as well as narrow band gap semiconductors such as cuprous oxide (Cu_2O), cupric oxide CuO, and cobalt oxide (Co_3O_4). Further this work focuses on the solar cells that use copper oxides as the absorber layer.

A basic structure of an all-oxide solar cell (Figure 2.6) includes:

1. transparent conducting oxide (TCO) coated on a substrate (usually glass);
2. window or buffer layer, which is a wide band-gap n-type semiconductor;
3. light absorbing layer (absorber), which is most commonly a p-type semiconductor;
4. metal back contact.

This assembly can be expanded with additional buffer or transport layers [17].

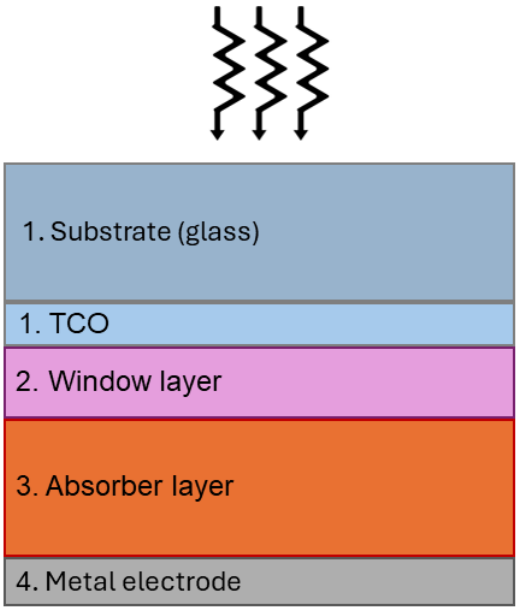

Figure 2.6. Basic structure of an all-oxide solar cell.

The transparent conductive oxides are used not only in electronics but also in other optoelectronic devices, such as led displays, electrochromic systems, or semitransparent devices [18]. The most well-known is indium tin oxide (ITO). Other good examples are fluorine tin oxide or doped titanium oxide. Recently doping of zinc oxide with aluminum showed good performance, and AZO is used as an alternative TCO. ITO shows better transparency and conductivity than AZO, but ITO suffers from issue of low abundance, high cost and toxicity of indium, which are not a problem for AZO [19].

The buffer layer role in e.g. CIGS based solar cells is to improve the band alignment between the heterojunction and the transparent electrode, as well as to reduce the shunt resistance of the cell, as the window layer has relatively high conductivity. In all-oxide solar cells, the window layer is often the same as one of the materials that make the heterojunction [20]. The two oxides that are most often used as the window layer for copper oxides based absorbers are ZnO and TiO_2. They both have appropriate band gaps of 3.3 eV and 3.2 eV, respectively [21] [22]. Modifications of these materials to achieve ternary or quaternary oxides is often a topic of research.

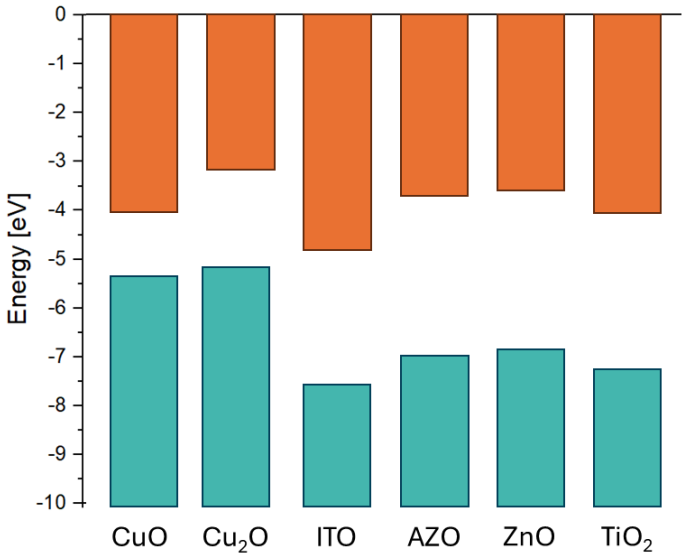

Figure 2.7. Conduction bands (orange) and valence band (blue) of commonly used oxides in all-oxide solar cells featuring two transparent electrodes, two absorber materials, and two window layer materials.

The p-type material to be used as the absorber layer should have high absorption coefficient, in ideal case the band gap value should be of 1.4 eV, but all the values between 1.0 and 2.0 eV are useful. The minority carrier diffusion length, carrier mobilities, and amount of impurities all are important parameters regarding the undesired recombination of carriers that occurs in the material. Among oxides Cu_2O is used most often as the absorber layer. But other oxides have promising properties as well, where two other copper oxides are good examples CuO and Cu_4O_3. Other oxides with high absorption and proper value of energy band gap are cobalt, nickel and iron oxides.

The transport properties of oxide semiconductors depend on defects and impurities present in the material. In electron transport (n-type) semiconductor oxides, like TiO_2, the oxygen vacancies are the source of free charge carriers. In hole transport oxides (p-type), for example CuO, transport properties depend on metal vacancies, in this case copper vacancies. The amount and type of defects are affected by the synthesis method, the doping level and species, the post treatment of material and functionalisation of the surface, among others.

The performance of all-oxide solar cells is significantly influenced by the electronic band structure of the materials used and their alignment at the junctions. The alignment of the conduction band and valence band between the p-type and n-type materials at the junction is crucial for efficient charge separation and transport. The conduction and valence bands with the energy band gap of most common materials used in all-oxide solar cells are presented in Figure 2.7. Proper band alignment ensures that photo-generated electrons in the p-type layer can move easily to the n-type layer, while holes in the n-type layer can migrate to the p-type layer. This reduces recombination losses and enhances the efficiency of the solar cell. Mismatched band alignments can create energy barriers that impede the flow of electrons and holes, leading to reduced efficiency. The interface between different oxide layers also plays a critical role in the device's performance. Defects or impurities at these interfaces can create traps for charge carriers, increasing recombination rates and lowering the efficiency. In case of Cu_2O based cells, the fact that Cu rich phase emerges at the surface has a negative influence [20].

All-oxide solar cells most commonly use Cu_2O as the absorber layer. It is usually combined with ZnO as the counterpart in the heterojunction. Some works show solar cells made with copper oxide homojunctions, but it was proved impossible to achieve n-type copper oxide [23]. Some chosen examples of solar cell prepared using copper oxides as the absorber layer, are listed in Table 2.1. Many approaches are used to improve the performance of a solar cell, doping of absorber layer, using ternary oxides as window layer, adding new layer to improve the band alignment [24], and also using new forms of copper oxides as nanostructures [25] or in a form of bulk heterojunction with ZnO [26].

The current best all-oxide solar cells are from Minami et. al. [27] and Shibasaki et. al. [28]. The first group presented structure of MgF_2/AZO/$Zn_{0.38}Ge_{0.62}$-O/Cu_2O:Na. Copper oxide was grown thermally on copper metal plate, it was doped with Na using NaCl. The window layer is a ternary oxide, and its composition optimises the band alignment at the junction. Additionally, an anti-reflective layer of MgF_2 was used, and the AZO was the transparent electrode. Pulsed laser deposition was used to deposit ZnO layers, and evaporation to deposit MgF_2. On of the produced cells showed efficiency of 8.1% measured at STC. The second group achieved 8.4% efficiency with AZO/$Zn_{1-x}Sn_xO_y$/Ga_2O_3/Cu_2O/SnO_2:Sb/ITO system. Cu_2O thin films were deposited using reactive sputtering onto TCO on a glass substrate. This TCO was composed of double layers of SnO_2:Sb (ATO) and ITO. Then Ga_2O_3 and ZTO layers were fabricated by atomic layer deposition onto the Cu_2O thin film. Lastly sputtering deposition was used to deposit AZO as front transparent electrode, and a plastic microlens was attached as an anti-reflective film. It must be noticed that the best systems used many forms of doping to achieve their performance.

Table 2.1. Structure and performance of chosen all-oxide solar cells.

Cell structure	V_{oc}, V	J_{sc}, mA/cm^2	FF, %	Efficiency, %	Ref.
Cu/Cu_2O:Na/$(Ga_{0.975}Al_{0.025})_2O_3$/AZO	0.84	10.95	0.66	6.10	[29]
MgF_2/AZO/$Zn_{0.38}Ge_{0.62}$-O/Cu_2O:Na	1.1	11.0	-	8.10	[27]
FTO/ZnO/CuO/MoO_3/Au	0.468	9.5	48.43	2.11	[24]
ITO/ZnO/CuO/Cu_xO nanostructures/Ag	0.4	20.90	34.3	2.88	[25]
FTO/ZnO-CuO/Al	0.41	6.37	46	1.17	[26]
Cu/Cu_2O/ZnO/AZO	0.52	9.8	58	3.22	[30]
AZO/$Zn_{1-x}Sn_xO_y$/Ga_2O_3/Cu_2O/SnO_2:Sb/ITO	1.13	20.63	69	8.4	[28]
ITO/$Zn_{0.79}Mg_{0.21}O$/Cu_2O/Cu	0.65	6.9	0.49	2.20	[31]
Au/CuO/AZO nanorods/FTO	0.39	3.45	57.12	0.76	[32]
Ag/Cu_2O/ZnO/AZO/ITO	0.52	2.92	38	0.7	[33]

2.4 Copper oxides

Copper oxides, an essential class of semiconductor materials, have gained significant attention due to their diverse electronic properties and potential applications in various technological fields. The most common copper oxides are cuprous oxide (Cu_2O) and cupric oxide (CuO), and less studied paramelaconite (Cu_4O_3). In room temperature at atmospheric pressure CuO is the thermodynamically stable phase. With higher temperatures and smaller oxygen partial pressure first Cu_2O is the most stable phase and then Cu becomes the most stable as shown in phase diagram in Figure 2.8 [34] [35]. Each of copper oxides exhibits unique properties that make them suitable for applications in optoelectronics, solar energy conversion, and sensing devices. Cuprous oxide is one of the oldest known light-sensitive materials with first analysis of such properties from 1916 by A. H. Pfund [36]. In the next decades L. O. Grondahl worked on the first devices that adopted copper oxide [37] [38]. The interest in semiconducting properties of copper oxides diminished with the development of Czochralski method which started the era of silicon in electronics and later photovoltaics. CuO and Cu_4O_3 are less studied materials, although CuO has recently gained more interest as being an alternative to Cu_2O in solar cell applications [39].

Each copper oxide has a different crystal structure: Cu_2O crystallises in cubic system space group Pn3m number 224, CuO crystallises in monoclinic or tetragonal phase, where the monoclinic tenorite structure is more stable (space group C2/c number 15), Cu_4O_3 crystallises in tetragonal system space group I41/amd number 141. The unit cells of CuO and Cu_2O are presented in Figure 2.9.

The p-type semiconducting properties of copper oxides originate from Cu vacancies in the structure of the oxide. There is an ongoing discussion if n-type conductivity is possible. There are

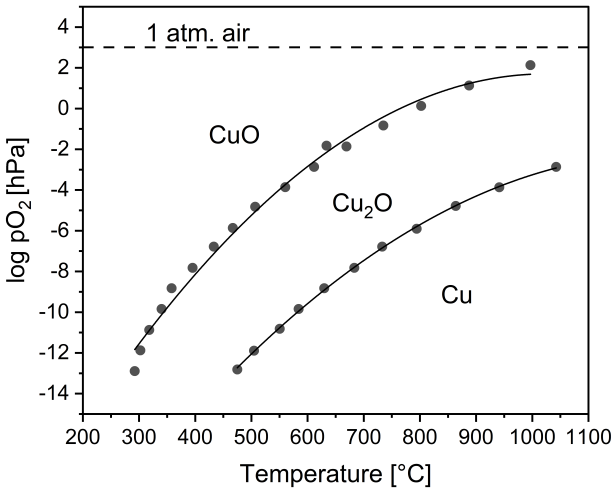

Figure 2.8. Pressure-temperature phase stability diagram of Cu-Cu_2O-CuO system. [34]

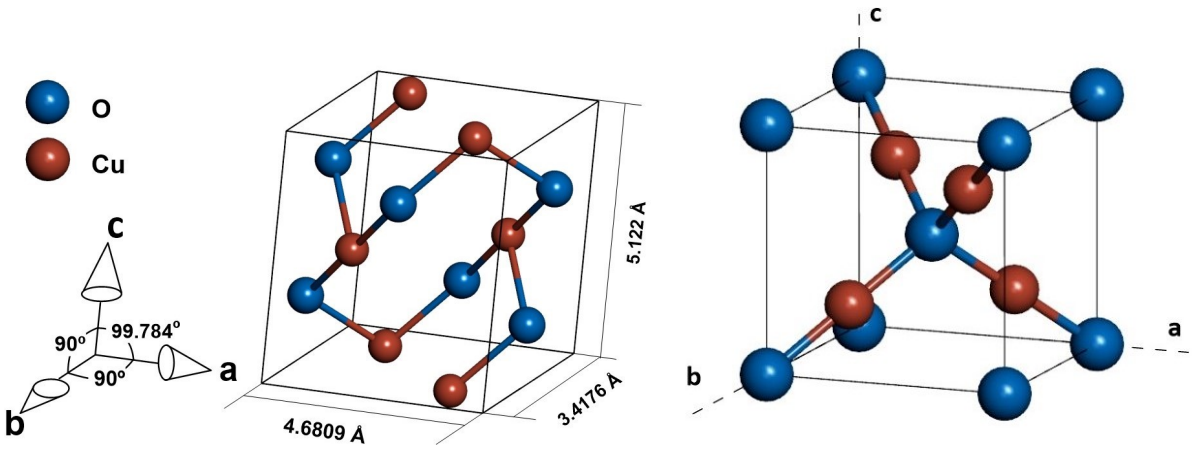

(a) (b)

Figure 2.9. Unit cells of (a) CuO and (b) Cu_2O.

some reports of electrodeposited Cu_2O with intrinsic n-type conductivity, however D.O. Scanlon and G.W. Watson showed that it is not possible [23]. They discussed that the reported n-type conductivity origins from an inversion layer formed during electrodeposition, and possible external impurity doping. Achieving n-type copper oxides via doping is possible tough very hard, with p-type doping being easier due to the binding energies of donors and acceptors [39].

Both CuO and Cu_2O have bang gap values promising for photovoltaic applications. The energy band gap of CuO ranges from 1 eV to 1.9 eV [40, 41, 42, 43]. The bang gap of Cu_2O is reported to be between 2.0 and 2.5 eV [44, 45, 46, 47]. For these materials the Shockley-Queisser limit predicts efficiency of single junction at level of 30% and 20%, respectively. Where the optimal band gap of a material for maximum possible energy conversion efficiency is 1.3 eV. But the efficiency of photovoltaic device depends in a complex way on the optical properties of materials, the present

defects, thermodynamics and fabrication methods [48]. Cu_2O has the band gap of direct forbidden nature, while CuO type of transition is indirect and allowed [49]. The band structure and density of states for all three copper oxides are presented in Figure 2.10 (a).

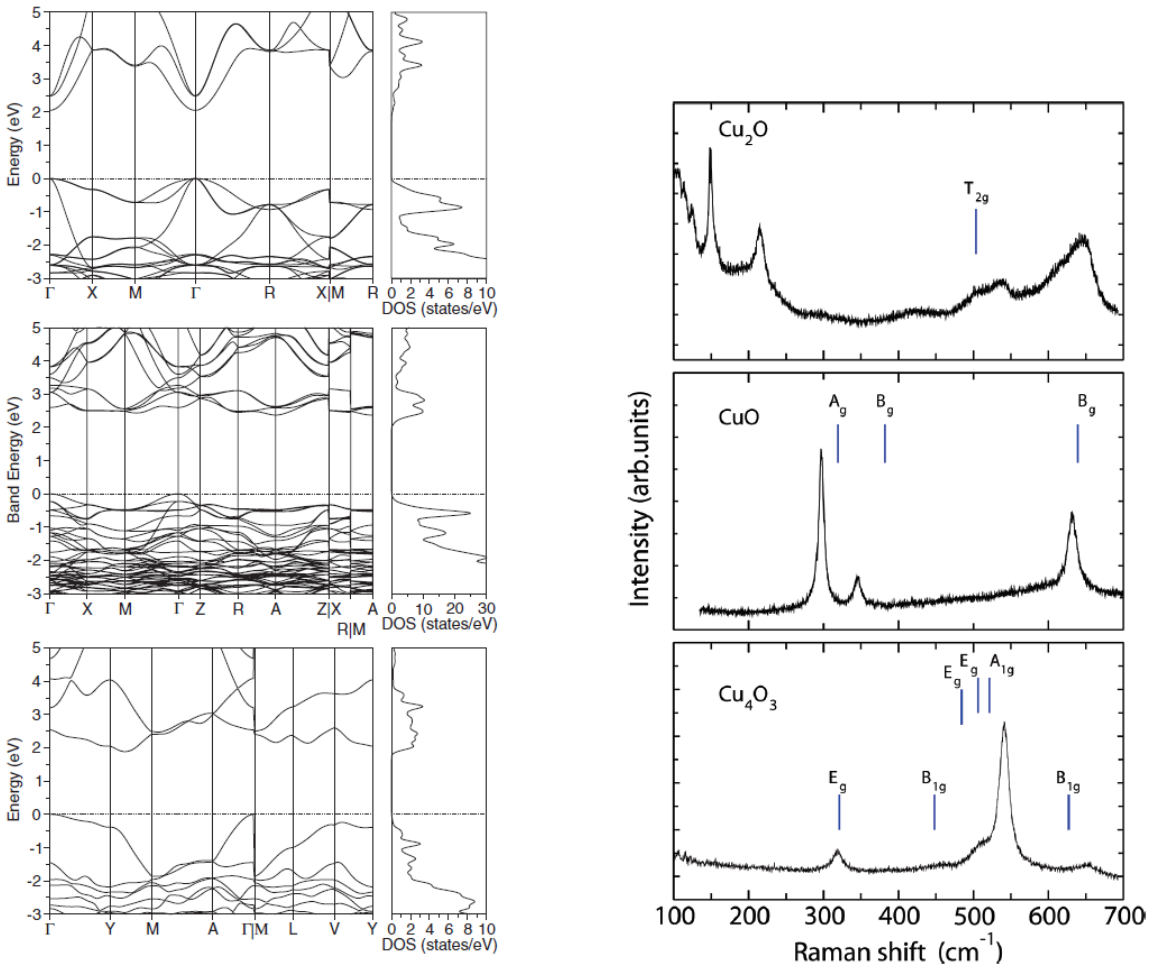

(a) (b)

Figure 2.10. (a) Electronic band structure and density of states of CuO, Cu_2O and Cu_4O_3; (b) experimental Raman spectra of CuO, Cu_2O and Cu_4O_3 marked with the most important vibrational modes [49] [50].

All the copper oxides exhibit allowed vibrational modes in both Raman and infrared spectroscopy. The main Raman modes are presented in Figure 2.10 (b) after Debbichi et al. experiment [50]. They used also first-principle density functional theory calculations to analyse the vibrational properties of CuO, Cu_4O_3 and Cu_2O. All calculated modes of CuO and Cu_2O with allowed modes of Cu_4O_3 are collected in Table 2.2.

Copper oxides are considered good candidates for absorber layer as they have high absorption coefficient with value of order of 10^5 cm^{-1}. The absorption of light takes place by numerous possible electron transitions in the material. L. Yu and A. Zunger proposed an alternate to Shockley-

Table 2.2. Calculated frequencies of all vibrational modes for Cu_2O and CuO, and only allowed modes for Cu_4O_3 [50].

oxide	mode	activity	frequency [cm^{-1}]
Cu_2O	T_{2u}	silent	60
	E_u	silent	72
	T_{1u}	IR	144
	A_{2u}	silent	338
	T_{2g}	Raman	503
	T_{1u}	IR	616
CuO	B_u	IR	141
	A_u	IR	164
	A_g	Raman	319
	A_u	IR	327
	B_g	Raman	382
	A_u	IR	457
	B_u	IR	503
	B_u	IR	568
	B_g	Raman	639
Cu_4O_3	E_u	IR	50
	E_u	IR	99
	E_u	IR	121
	A_{2u}	IR	127
	E_u	IR	168
	E_u	IR	214
	A_{2u}	IR	224
	A_{2u}	IR	309
	E_g	Raman	321
	B_{1g}	Raman	448
	E_u	IR	454
	E_g	Raman	484
	E_g	Raman	506
	A_{1g}	Raman	521
	E_u	IR	538
	A_{2u}	IR	576
	E_u	IR	603
	B_{1g}	Raman	627
	A_{2u}	IR	649

Queisser limit selection metric - spectroscopic limited maximum efficiency SLME [48]. They take into consideration the nature of electron transitions in the material and the absorption coefficient spectrum. Zivkovic et al. used this method to calculate the predicted efficiencies for copper oxides, and results were 0.54% for Cu_2O and 1.40% for Cu_4O_3. The resulted value of efficiency for CuO was negligible, and without modifications efficiency over 1% would be hard to achieve [49]. Thus, modifications of copper oxide thin films are necessary to aim for good photovoltaic performance.

A main way to improve the properties of semiconductor materials is doping. There are many works where one of copper oxides were doped with different methods of deposition and doping elements applied.

Mostly p-type dopants are used in case of copper oxides. Ishizuka et al. used nitrogen to improve the properties of Cu_2O thin films deposited by reactive magnetron sputtering [51]. They investigated the effects of nitrogen used as a p-type dopant, which effectively increases the hole density in the films, making it a viable method for controlling the electrical properties of Cu_2O. The study found that the acceptor level of nitrogen is around 0.14 eV, and nitrogen doping achieved the lowest reported resistivity for Cu_2O thin films at 15.2 Ωcm. Despite the doping, there were no significant degradation in the structural and optical properties of the films. This research highlights nitrogen's potential as a beneficial dopant in developing efficient Cu_2O-based photovoltaic devices [51]. Another work that used nitrogen as dopant was done by Malerba et al. [52]. This study also investigates the effects of nitrogen doping on the optical and electrical properties of Cu_2O thin films produced using reactive RF-magnetron sputtering. The researchers found that nitrogen doping induced clear absorption bands below the fundamental optical band gap, with the intensity of these bands correlating with the nitrogen concentration. The most heavily doped samples achieved the lowest reported resistivity for Cu_2O, at 1.14 Ωcm [52]. Other dopants and deposition techniques used were: vanadium and sol-gel with dip-coating [53], nickel and solution combustion method [54], chloride and electrodeposition [55], fluorine and electrodeposition to achieve n-type Cu_2O and create a homojunction solar cell [56].

Zivkovic et al. [49] used first principle calculation to explore the potential enhancement of Cu_2O as a p-type semiconductor for photovoltaic applications through the doping of first-row transition metals. Using hybrid density functional theory (DFT), the study investigates how these dopants, incorporated at copper sites, create a range of defect states that tune the band gap of Cu_2O. The presence of copper vacancies, intrinsic to Cu_2O, stabilises these defect formations and enhances the material's optical absorption. The study identifies that transition metals like Ni, Fe, and Zn are particularly effective in improving the photovoltaic conversion efficiency by introducing beneficial changes in the electronic structure. The results suggest that transition metal doping could significantly boost the overall light absorption and efficiency of Cu_2O-based photovoltaic devices.

Chromium is a transition metal which was used as a dopant in few studies with application of copper oxides thin films in sensors. Szkudlarek and Rydosz [57] explored the use of CuO thin films doped with various metals (Ag, Au, Cr, Pd, Pt, Sb, Si) for gas sensor applications, specifically targeting propane detection in exhaled breath as a potential biomarker for diseases like diabetes. The films, deposited on low-temperature cofired ceramics substrates using magnetron sputtering, demonstrate improved gas-sensing properties when doped, with Cr-doped CuO showing the highest sensor response. In their next work they focused on Cr doping and explored more the effect of Cr as a dopant in CuO. The study reveals that Cr doping introduces a shallow donor band, which reduces the charge carrier concentration, enhancing sensor response and selectivity towards acetone, even in high humidity conditions. Characterisation techniques such as X-ray diffraction (XRD), X-ray photoelectric spectroscopy (XPS), Energy Dispersive Spectrosocopy (EDS), Scannng Electron Miscroscopy (SEM), and Atomic-force Microscopy (AFM) confirm the substitutional incorporation of Cr into the CuO lattice. Density Functional Theory (DFT) calculations further explain the electronic properties, showing that Cr doping increases baseline resistance and facilitates electron-hole recombination, thereby reducing conductivity. The research suggests that Cr-doped CuO thin films, produced through a controlled and scalable fabrication process, have promising commercial applications in gas sensors, catalysis, photovoltaics, and other optoelectronic devices [58]. Other researchers used Cr doping in CuO nanoparticles to enhance sensing of ammonia and NO_2, the particles were prepared with hydrothermal and chemical precipitation methods [59, 60].

A study on electrical and optical properties of Cr doped CuO was done by Baturay et al. [61]. This article investigates the synthesis and characterization of undoped and Cr-doped CuO thin films deposited on soda-lime glass (SLG) and p-type Si (100) substrates using the spin coating method, followed by annealing at 500°C. The structural analysis via XRD reveals that all films possess a monoclinic polycrystalline structure, with characteristic peaks (-111) and (111) observed. The optical properties, examined through UV–Vis spectroscopy, show that Cr doping influences the transmittance and energy band gap of the films, with the band gap ranging from 1.67 to 2.03 eV as Cr concentration increases. The films' transmittance reached up to 33% with 3% Cr doping in the visible range. Electrical properties, analysed using I–V and C–V characteristics, indicate that the 1% Cr-doped CuO/p-Si diode exhibits the best rectification ratio and light sensitivity. Additionally, C–V measurements show that Cr doping affects the devices' electrical parameters, such as barrier height and ideality factor. The findings suggest that Cr-doped CuO films, particularly with 3% doping, hold promise for applications in photovoltaic devices due to their enhanced photoelectrical properties.

In this work Cr doping of copper oxides is performed with ion implantation methods, and the influence of this process on material is studied with numerous characterization methods. The ion implantation technique and its advantages are discussed in the next section.

2.5 Ion implantation

Ion implantation is a pivotal technique for doping semiconductors, offering precise control over dopant distribution, crucial for modern electronics [62, 63]. The process involves bombarding a semiconductor with high-energy ions, introducing defects into the substrate. The energies used in ion implantation are usually in range of 10 – 200 keV yet experiments with ions of high MeV order energy are also performed [64]. This method stands out for its accuracy, allowing specific regions of a semiconductor to be doped with minimal diffusion compared to thermal methods. The process's versatility enables the formation of various junction types and the modification of electrical properties across different materials. The changes introduced to material can be aimed to differ various properties including mechanical [65], corrosion resistance [66], electrical [67, 68], and optical [69, 70].

A typical ion implantation system consists of an ion source, accelerator, and target chamber. A simple scheme of the apparatus used in ion implantation - the implantator, is presented in Figure 2.11. In this setup the most important element is the mass analyser, which enables creation of a coherent beam consisting of one type of ion. Electromagnets bend the beam in a way to pass only the desired ions, the analyser is marked in Figure 2.11 as a green pentagon, the ion source is marked as an orange box on the left side, and the target chamber as a green box on the right side of the Figure 2.11. The apparatus utilised in this work has a system of three diffusion pumps that enables pressure levels of order of 10^{-6} Pa in the target chamber and 10^{-3} Pa in the rest of the system. Two rotary pumps are used as fore vacuum pumps.

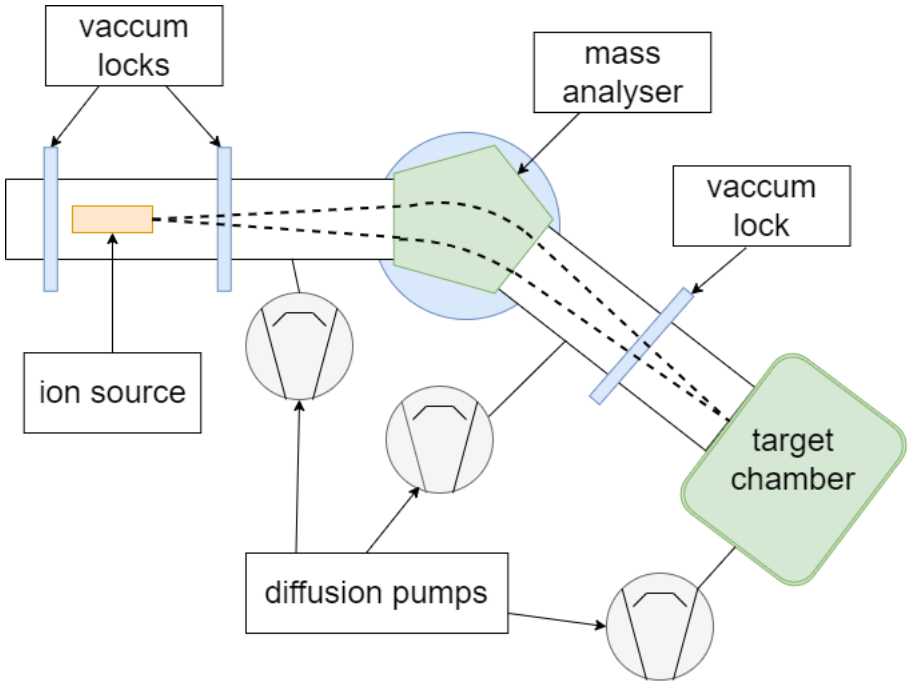

Figure 2.11. Diagram of ion implantator apparatus.

The ions are generated, accelerated to high velocities, and directed towards the semiconductor substrate. Upon impact, ions penetrate the surface, losing energy through collisions with the lattice atoms, which leads to the placement of dopant atoms at specific depths. The depth and concentration of the dopants are determined by the energy and dosage of the ions. Ions impacting a material can interact with it in two primary ways: through inelastic collisions with electrons attached to the material's atoms (known as electronic stopping) or through elastic collisions with the nuclei of the material's atoms (referred to as nuclear stopping). The latter mechanism leads to recoil cascades, where an atom in the material gains sufficient energy to displace another atom, causing a chain reaction that continues until all the energy is dissipated. Most of the energy from electronic stopping is converted into thermal energy. Other effects of ion implantation, as illustrated in Figure 2.12, include the creation of phonons and plasmons, electron excitation in the material, thermally driven diffusion, and significant structural damage that often leads to the amorphisation of the material.

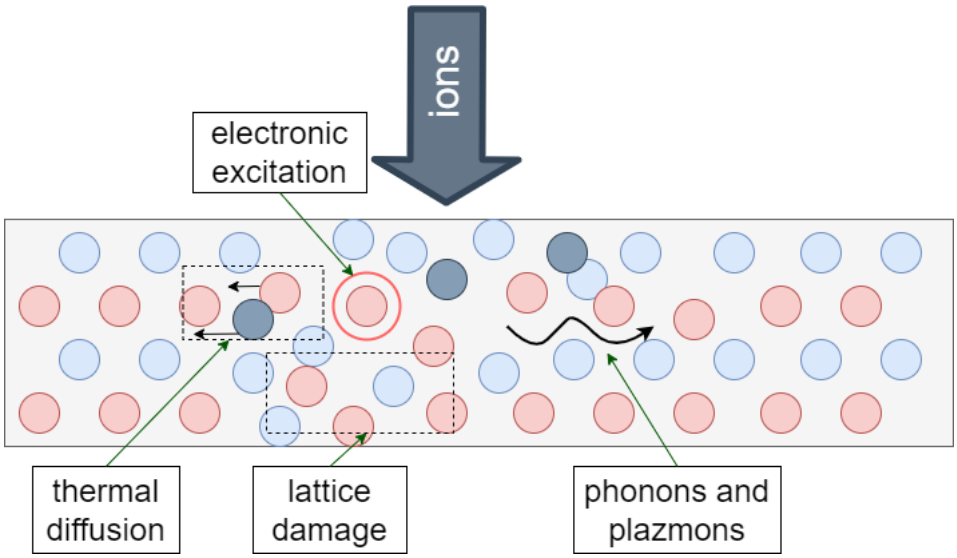

Figure 2.12. Diagram showing processes caused by ion implantation in the target material.

Post-implantation, the semiconductor often requires annealing to repair implantation-induced damage and activate the dopants electrically. The annealing process typically involves heating the substrate, which helps the dopants occupy substitutional sites in the lattice, restoring crystallinity and electrical properties. The temperature and duration of annealing depend on the implanted species and the semiconductor material.

The effects of ion implantation vary with different dopants and substrate materials. For instance, in silicon, boron and phosphorus are common dopants, used to create p-type and n-type regions, respectively. The implantation of these ions typically requires subsequent annealing temperatures around 800-1000°C. Conversely, materials like GaAs exhibit more complex behaviours. The regrowth of ion-damaged GaAs layers involves multiple stages, with the recrystallisation pro-

cess often completed at temperatures exceeding 700°C. In this case, annealing must be carefully controlled to prevent defects that could degrade device performance.

The technique's flexibility is evident in its application to different semiconductor materials and devices. It is indispensable in fabricating integrated circuits, where precise dopant profiles are critical for device characteristics. For example, in fabricating MOSFETs, shallow source/drain regions are achieved through low-energy implantation, while deeper wells require higher energy. Moreover, ion implantation can be used to introduce defects deliberately, creating specific electrical properties. For instance, nitrogen implantation can form amorphous silicon nitride, enhancing dielectric properties. Similarly, the creation of deep-level traps in silicon can be achieved using high-energy implants of ions like helium or hydrogen, useful for charge storage applications [62]. Photovoltaics can also benefit from doping materials with ion implantation. In their review Kaur et al. explore the impact of ion-implantation on the efficiency of photovoltaic cells [71]. They emphasise that ion-implantation can significantly enhance the performance of solar cells by altering material properties. This technique helps reduce charge recombination, modify and fabricate nanostructures, and improve charge transfer. The process involves implanting ions into the material to change its electrical and optical properties, leading to more efficient solar cells with lower fabrication costs. The review also discusses the use of different ions and their effects on various types of solar cells, showcasing improvements in efficiency and conductivity. For example, carbon ion implantation of TiO_2 improved efficiency of a dye-sensitised solar cell. The implantation induced phase transition from rutile to anatase what reduced the recombination of charge carriers [72].

The effects of ion implantation can be simulated with SRIM software (Stopping and Range of Ions in Matter). It is a comprehensive software package widely used for simulating the interactions of ions with various materials. Developed by James F. Ziegler and his colleagues [73], SRIM provides detailed calculations on how ions penetrate, lose energy, and come to rest within different target materials. The software includes several modules, the most prominent being TRIM (Transport of Ions in Matter), which offers precise simulations of ion trajectories. This simulation capability is vital for understanding the effects of ion implantation. By predicting the depth and distribution of ions, SRIM helps to optimise processes such as doping in semiconductors. The software can model both the physical and chemical interactions of ions with matter, accounting for parameters like energy loss, scattering, and damage profiles. To perform calculations, we require the target material's density and composition as input parameters. Each element has distinct properties, such as surface binding energy and dissipation energy. This data, along with details on spatial distribution and thickness of target layer, serves as input for the software. SRIM's outputs include detailed reports on the stopping power, ion range, and damage distribution, which are essential for designing and interpreting experiments. Its ability to simulate a wide range of ions and materials makes it an invaluable tool in research and industry, where understanding and controlling the interactions of ions with matter is critical.

2.6 Photovoltaics in space

Photovoltaics are an essential technology for space missions, providing a reliable and sustainable source of energy for satellites, space probes, and other spacecraft. In the harsh environment of space, where traditional power sources are impractical, solar panels convert sunlight into electricity, powering onboard systems and instruments. The efficiency, durability, and lightweight nature of photovoltaic cells make them ideal for space applications, where minimizing weight and maximizing energy output are critical. Advanced materials and designs, such as multi-junction solar cells, have been developed to enhance efficiency by capturing a broader spectrum of sunlight, even in low-light conditions. Moreover, photovoltaics are crucial for long-duration missions, including interplanetary travel and potential future bases on the Moon or Mars, as they can continuously generate power without refuelling [74]. Commercial satellites typically use silicon or dual or triple junction GaInP/GaAs/Ge solar cells. However, there is significant interest in thin-film solar cells for military applications. NASA also has missions planned where high specific power (kW/kg) and reduced costs are advantageous. Thin-film solar cells offer the benefits of high specific power when applied to flexible, lightweight substrates with appropriately lightweight support structures. Although these cells generally have lower efficiency and require a larger area to produce the same power levels, various trade studies have highlighted several potential applications for them [75]. In the research and development of solar cells for space applications it is important that the light reaching a cell has different spectrum than the one that falls on the surface of the Earth, where most of established technologies are used. The spectrum present at the Earth surface AM1.5 (AM stands for air mass) and the one present in space AM0 are presented in Figure 2.13.

Any material used in the space environment will be exposed to cosmic radiation. The conditions are different depending on the trajectory of a space mission. For missions orbiting Earth, these trajectories are generally categorised into low Earth orbit (LEO), ranging from 300 to 900 km, mid-Earth orbit (MEO), and geosynchronous orbit (GEO) at 35,780 km. NASA missions also encompass interplanetary travel, both towards and away from the Sun, as well as planetary flybys and orbiting other planets, each presenting unique environmental conditions. Additionally, future human missions may target the Moon and Mars, each requiring consideration of their specific surface power requirements and environmental conditions. Figure 2.14 illustrates the number of trapped particles as a function of energy for both Earth and Jupiter. The data for Jupiter were obtained from the Pioneers 10 and 11, as well as Voyagers 1 and 2, during their missions close to the planet.

When charged particles from space enter the Earth's magnetic field, they are deflected along the magnetic field lines. If these particles have low enough energy, they become trapped in the Van Allen belts, which are radiation belts surrounding the Earth at various altitudes depending on the magnetic field. These belts contain protons in the inner belt and electrons in both the inner

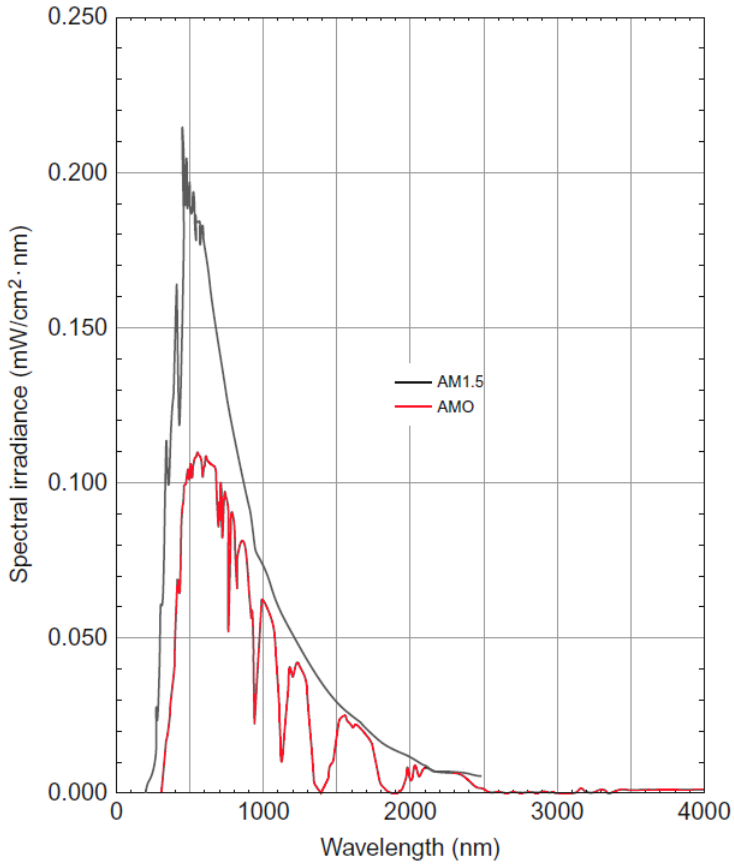

Figure 2.13. The Air Mass Zero spectrum and the Air Mass 1.5 spectrum.

and outer belts, spiralling along the magnetic field lines from pole to pole. Near the poles, these radiation belts can extend almost to the Earth's surface [76].

High-energy particles, primarily electrons and protons, can cause displacement damage in the lattice of solar cells, thereby degrading their electrical and optical properties. The issue of radiation degradation in space is complex and depends on various factors, including the type of particle, energy, fluence, shielding, and the design of the solar cell, such as layer thickness and the number of junctions. Ground-based radiation experiments typically use monoenergetic, unidirectional beams of particles, which makes it challenging to simulate the space environment, especially for multi-junction cells. The Jet Propulsion Laboratory (JPL) has historically set the standard for assessing radiation damage in silicon and gallium arsenide solar cells. For other materials, not yet used in the space industry, such calculations are not possible [77, 78]. To assess how these materials respond to the space environment, several methods can be used: studying the properties of materials over a wide temperature range from -150 to 150 °C, measuring solar cell performance with a solar simulator that provides the AM0 spectrum, and using particle beams with a single energy and dose to observe their impact on the material. However, it's important to note that on Earth, we

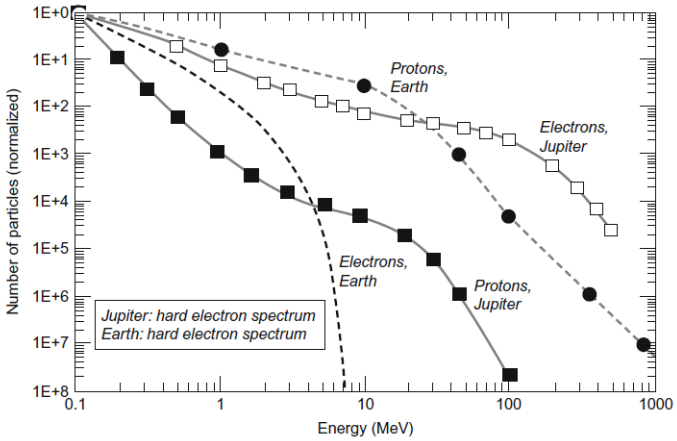

Figure 2.14. Normalised energy spectrum of trapped electron and proton radiation environment at Jupiter, compared to Earth [74]

.

cannot replicate the simultaneous exposure of materials to particles of different energies as occurs in space.

An example of a study that uses proton and electron irradiation to determine resilience of solar cell is work of Chen et al. [77]. They investigated the degradation characteristics of GaInP/GaAs/$In_{0.3}Ga_{0.7}As$ inverted metamorphic (IMM) and GaInP/InGaAs/Ge lattice matched (LM) triple junction solar cells under irradiation of 1 MeV electrons and 10 MeV protons. Both types of solar cells demonstrated strong resistance to radiation, with IMM cells showing a remaining maximum output power factor of 0.86 for electrons and 0.73 for protons, while LM cells showed 0.85 and 0.75, respectively. The IMM solar cells exhibited better current matching at the end of their operational life compared to LM cells. They calculated relative damage coefficients, using an equivalent displacement damage dose model, were found to be 3.11 for IMM cells and 2.78 for LM cells, indicating IMM cells' superior performance under radiation. Degradation mainly occurred in the GaAs middle and InGaAs bottom subcells for IMM structures and in the GaAs middle subcell for LM structures. The IMM cells' ability to maintain better current matching after irradiation highlights their potential advantages for space applications. Additionally, the study calculated the diffusion length damage coefficient for both solar cell types, further quantifying their radiation resilience. Researchers studied also oxide based photovoltaics as in work of Kato et al. [79]. Their study explores the potential use of NiO/ZnO visible-light-transparent solar cells for space applications. Measurements of current density–voltage and external quantum efficiency were conducted under air mass AM0 conditions, revealing that the short-circuit current density increased by 2.6 times compared to AM1.5 conditions. This increase is due to the absorption of ultraviolet light with wavelengths, which is more intense in AM0 conditions. The study also evaluated the durability of these solar cells after exposure to 380 keV proton irradiation. Results showed no significant degradation at proton fluences below $3{\times}10^{14}$ cm^{-2} to $1{\times}10^{15}$ cm^{-2}, sug-

gesting that NiO/ZnO solar cells may have better radiation tolerance compared to Cu(In,Ga)Se2 (CIGS) or GaAs-based solar cells. The research confirms the feasibility of using NiO/ZnO solar cells in space. The cells' increased performance under AM0 conditions and resilience to proton irradiation highlight their potential advantages over other solar cell technologies. However, improvements in crystal quality and further defect evaluations are needed to enhance their photovoltaic performance, indicating a promising area for future development in space applications.

The researchers study not only cells but also component layers, such as transparent conductive oxides which are already used in space applications [80]. Wei et al. [81] subjected ITO thin films to 100 keV proton beam irradiation at varying doses, with the highest dose being $2x10^{16}$ cm^{-2}, equivalent to seven years of exposure in the geomagnetic equator region. The irradiation process decreased both the conductivity and transmittance of ITO, while the sheet resistance doubled. Khasanshin and Novikov [82] investigated the effects of 20 keV proton irradiation on K208 glass coated with ITO. They observed that the degradation of the ITO film resulted in more significant changes in material reflectivity compared to uncoated glass. Oryema et al. [83] examined another transparent conductive oxide, fluorine-doped tin oxide (FTO), using a 7 MeV proton beam at various fluences. As the ion dose increased, the films' transmittance decreased, and the sheet resistance initially decreased at lower doses but suddenly increased at $1x10^{16}$ cm^{-2}. They also noted minor changes in the crystal structure of the oxide, with an improvement in crystallinity and a shift of peaks to lower angle values after irradiation.

In summary, using proton beam irradiation is a tested and good method to study the resistance of materials to space environment.

Chapter 3

Thin films deposition

This chapter shortly describes the methods and setups used to deposit films that were characterised in this work.

3.1 Reactive magnetron sputtering - copper oxides thin films deposition

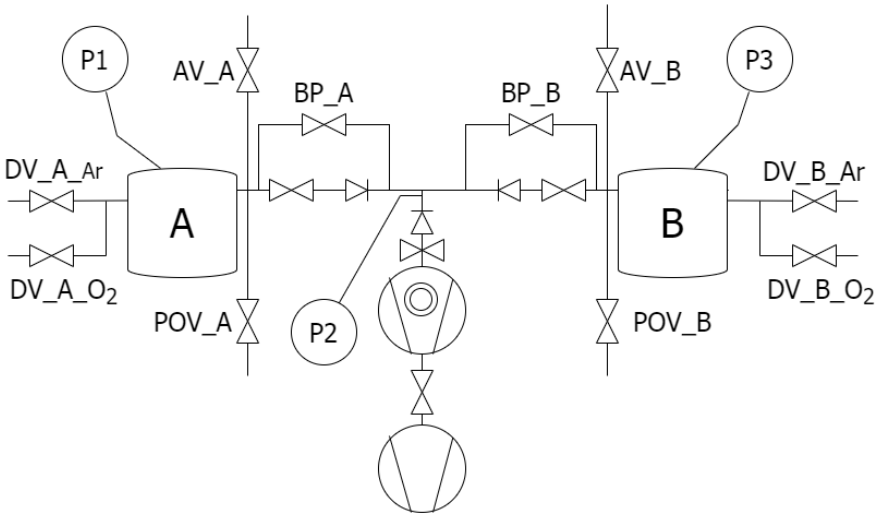

Figure 3.1. Scheme of vacuum installation in TWINPISK stand. P1, P2, P3 - vacuum probes, DV - electromagnetic valves for dosing gases, BP - by-pass manual valves, AV - venting valves, POV - electropneumatic valves.

Copper oxides thin films were deposited with reactive magnetron sputtering. The setup used is a two chamber vacuum technology stand called TWINPISK. The vacuum installation, shown in Figure 3.1 is based on a rotary and turbomolecular pumps which can give pressure at level of $5x10^{-6}$ mbar with one chamber being pumped or $1x10^{-5}$ mbar with two chambers being pumped

simultaneously. In this work chamber B was used which has a system that allows for heating of substrates. The inside of deposition chamber is shown in Figure 3.2b, the target is placed directed up and the substrates are mounted so to face down to the target. Figure 3.2a shows a copper target with visible erosion area. There is an additional rotary pump, not shown in Figure 3.1 that enables pumping of one chamber while a process is ongoing in the other one, for this task POV valves are used. The atmosphere in the chamber is regulated using mass flow controllers for Ar and O_2.

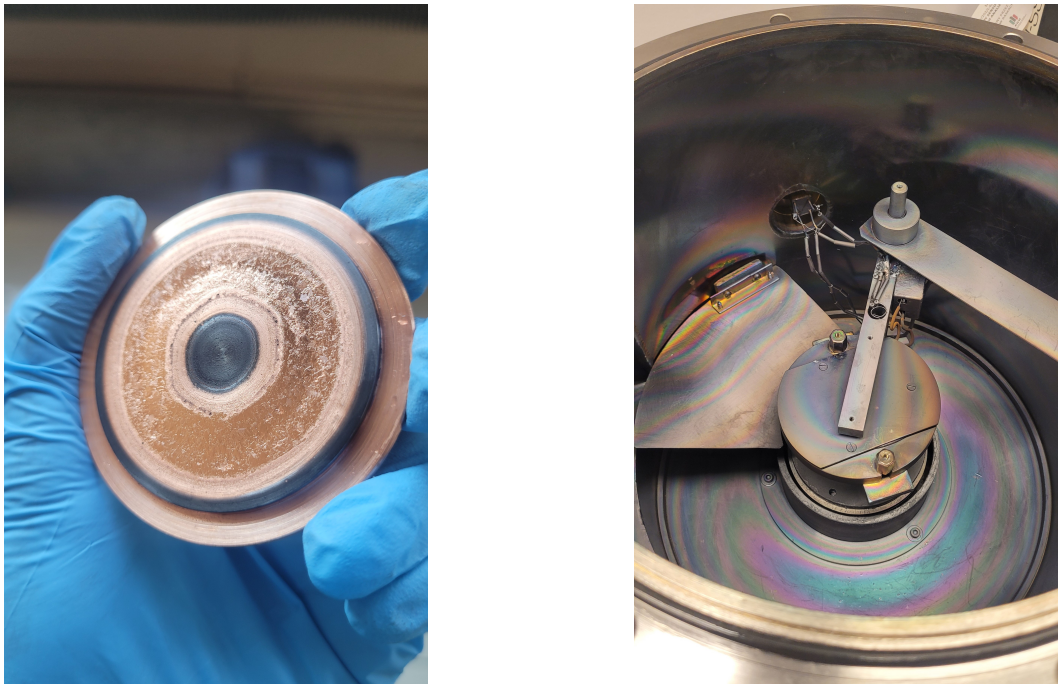

(a) (b)

Figure 3.2. (a) Copper target with visible erosion area, (b) inside of TWINPISK deposition chamber B.

Before deposition process the substrates (glass slabs or silicon) were cleaned with warm water and soap, and then submerged in isopropanol ultrasonic bath for 20 minutes. Just before mounting substrates on the holder, they were cleansed with N_2 to get rid of any possible dust or adsorbed particulates. The parameters of deposition process for each type of copper oxide are listed in Table 3.1. The target used for sputtering was Cu from Kurt J. Lesker of 99.95 % purity. Before deposition for each process a presputtering step was done, first in Ar atmosphere to clean the target for 10 minutes, and then in working gas for 20 minutes to stabilise the plasma and deposition environment.

Samples were made with different thicknesses and Taly-step profilometer of Rank Taylor Hobson was used to measure thickness of test deposition processes. Then by choosing appropriate time of deposition a desired thickness was reached. CuO films were deposited on silicon with thickness of 30 nm, 55 nm and 130 nm, and on glass with thickness of 130 nm and 1550 nm. All Cu_2O

samples on both silicon and glass were 130 nm thick. Cu_4O_3 was deposited only on silicon with thicknesses of 35 nm, 55 nm and 115 nm.

Table 3.1. Copper oxides thin films deposition parameters.

Oxide/Parameter	O_2 flow [sccm]	Ar flow [sccm]	P [W]	Pressure [Pa]	T [°C]
CuO	30	-	50	2.00	150
Cu_2O	18	2	50	1.80	150
Cu_4O_3	27	3	50	1.51	150

CuO thin films were prepared with reactive magnetron sputtering. The target used was 99.95% purity copper, the working gas was 100% O_2. During deposition the pressure was at level of $1.5x10^{-2}$ mbar and the substrates were heated to 150°C. Before deposition process a presputtering was performed in Ar and then in working gas. Discharge power was 50 W. ITO films were acquired from Merck, with a thickness of approximately 200 nm, deposited on a glass substrate. AZO films were deposited using atomic layer deposition (ALD) at a thickness of 100 nm, utilising a Beneq P400A reactor. The glass substrates were placed in a chamber where they were initially stabilised at a temperature of 200 °C and a pressure of 1 mbar for 4 hours. A rotary pump was used to achieve the low vacuum, and pressure was controlled by an MKS Baratorn 626D sensor. Diethylzinc and trimethylaluminium precursors were alternated with distilled water over a 2-hour period, with valve opening times of 0.3 and 0.5 seconds for the metal precursors and distilled water, respectively. The samples treated with proton irradiation are labelled with ": H+".

3.2 Atomic Layer Deposition - transparent electrode made of Al-doped zinc oxide

Zinc oxide doped with aluminium (ZnO:Al or AZO) films were deposited using atomic layer deposition. This method has been proved successful in this material production [84, 85]. The device used for ALD deposition was a Beneq P400A reactor at Centrum Badań i Rozwoju Technologii dla Przemysłu laboratory. The glass substrates were placed in a chamber to be initially stabilised at temperature of 200 °C and pressure of 1 mbar for 4 h. The low vacuum was achieved using a rotary pump, the pressure was controlled using an MKS Baratorn 626D sensor. The precursors used were diethylzinc, trimethylaluminium and distilled water. The opening times of the valves that supply the precursors and the distilled water were 0.3 and 0.5 s, respectively. They were alternated over a period of 2 hours to achieve thickness of 100 nm. Another transparent conductive oxide (so a transparent electrode in a solar cell) was ITO. The films were purchased from Merck and had a thickness of around 200nm, deposited on a glass substrate.

3.3 DC magnetron sputtering - ZnO thin films deposition

Zinc oxide films used for solar cell systems construction were deposited with DC magnetron sputtering. The setup used consisted of two chambers: plasma cleaning and deposition chamber. High vacuum was achieved with rotary pumps and a turbomolecular pump. The thickness of deposited film was controlled with a quartz crystal sensor. The deposition parameters were 35 W, around 100 mA and 360 V, working pressure of $5x10^{-3}$ mbar, the working gas was Ar. The target used was made of sintered ZnO, it is visible in Figure 3.3a. During the deposition process a purple plasma was created (Figure 3.3b).

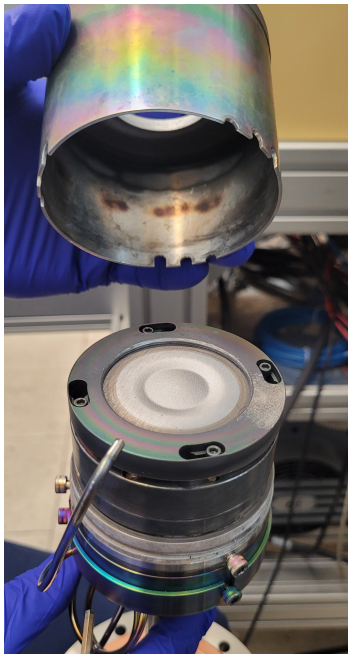

(a)

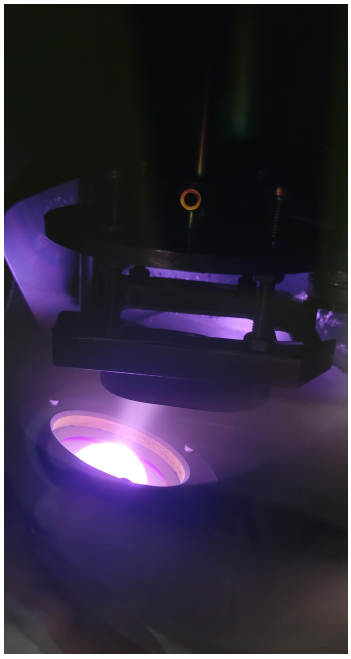

(b)

Figure 3.3. (a) Magnetron with mounted ZnO target and outer cover taken off, (b) plasma created during ZnO deposition.

3.4 Thermal evaporation of metallic Al electrode

Aluminium electrodes in solar cell systems were deposited with thermal evaporation of 99.99% pure aluminium from a heated tungsten spiral. The low pressure (less than 4.95 x 10^{-5} mbar) was achieved with rotary and diffusion pumps. The setup is very simple, where a piece of metal is placed on a tungsten spiral. The substrates, samples, were always placed on a carousel that ensured even coating of the samples and possibility to deposit metal on many samples in one process.

Chapter 4

Investigation of copper oxide thin films modified by Cr ion implantation

This chapter presents experiments and studies that considered chromium ion implantation of copper oxides thin films. First the implantation experiment is described and then simulations of implantation made with Stopping and Range of Ions in Matter (SRIM) program. Then results of simulations and samples characterisation are presented and discussed. CuO is presented separately, as it was studied the most thoroughly. The final section of the chapter covers the results for the other copper oxides, specifically Cu_2O and Cu_4O_3.

4.1 Ion implantation

The implantation experiments were conducted at the The Henryk Niewodniczański Institute of Nuclear Physics Polish Academy of Sciences in Kraków. The ion implantation equipment features a modified Bernas-type source of ions and electromagnets that precisely select the ions with desired energy and mass. Anhydrous chromium trichloride was used as a source of Cr ions. The energy and dose of implanted ions are summarised in Table 4.1. The dose of ions was controlled by the time that a moving sample holder spent in front of the ion beam. CuO and Cu_2O samples of 130 nm thickness deposited on glass were annealed after implantation. Both at temperature of 400°C, CuO in air and Cu_2O in Ar ambience.

4.2 SRIM simulations

The simulations were done for all oxides for Cr ion implantation with energy corresponding to performed experiments. CuO was simulated for 10 keV and 15 keV energy of ions, Cu_2O only for 10 keV ions, and Cu_4O_3 only for 15 keV ions. The simulation does not consider crystal structure of the target material, so it is treated as an amorphous one, and channelling effects do not influence

Table 4.1. Parameters of ion implantation experiments and samples that were implanted.

Energy [keV]	Dose [cm^{-2}]	Implanted samples
10	$1x10^{14}$	CuO 130 nm on glass and silicon, Cu_2O 130 nm on glass
	$5x10^{14}$	CuO 130 nm on glass and silicon, Cu_2O 130 nm on glass
	$1x10^{15}$	CuO 130 nm on glass and silicon, Cu_2O 130 nm on glass
15	$5x10^{16}$	CuO 30nm, 55 nm, 130 nm on silicon, Cu_4O_3 30 nm, 55 nm, 115 nm on silicon

the result. The input data into the simulation are density of target material, its atomic composition and information about the ion beam - element, energy and incident angle. The densities of copper oxides used in simulations are: CuO - 6.31 g/cm^3, Cu_2O - 6.00 g/cm^3, Cu_4O_3 - 5.84 g/cm^3.

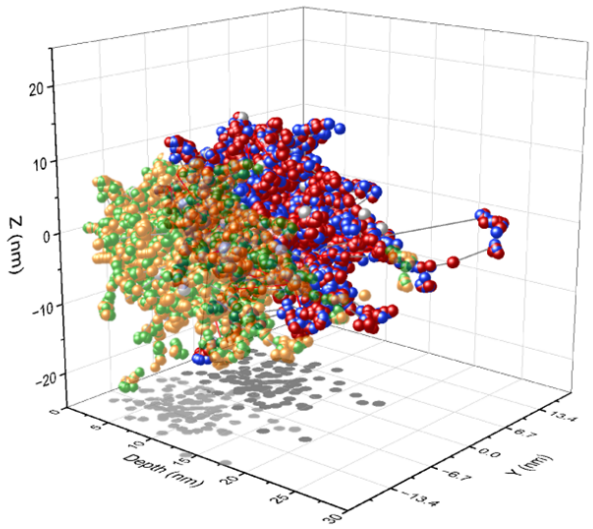

Figure 4.1. Illustration of recoil cascades from two neighbouring ion beams overlapping each other. Coloured balls represent atoms of different elements: red and yellow - Cu, blue and green - O, grey - Cr.

The main results used from simulations were the distribution of ions in depth of the material and the shape and distribution of recoil cascades. It is crucial to remember that in the simulation only a point beam is considered while in the experiment the beam falls onto the whole surface of the sample. SRIM package cannot add the influence of many neighbouring beams of ions. Some of ions and recoiled lattice atoms are directed perpendicularly to the beam, they would interact also with ions and atoms energised by a neighbouring beam. So not all the reactions are considered in the simulation and thus it is expected that the distribution of ions and recoils is underestimated.

Figure 4.1 illustrates atom recoils from one simulation placed next to each other. It is visible that many atoms overlap with others.

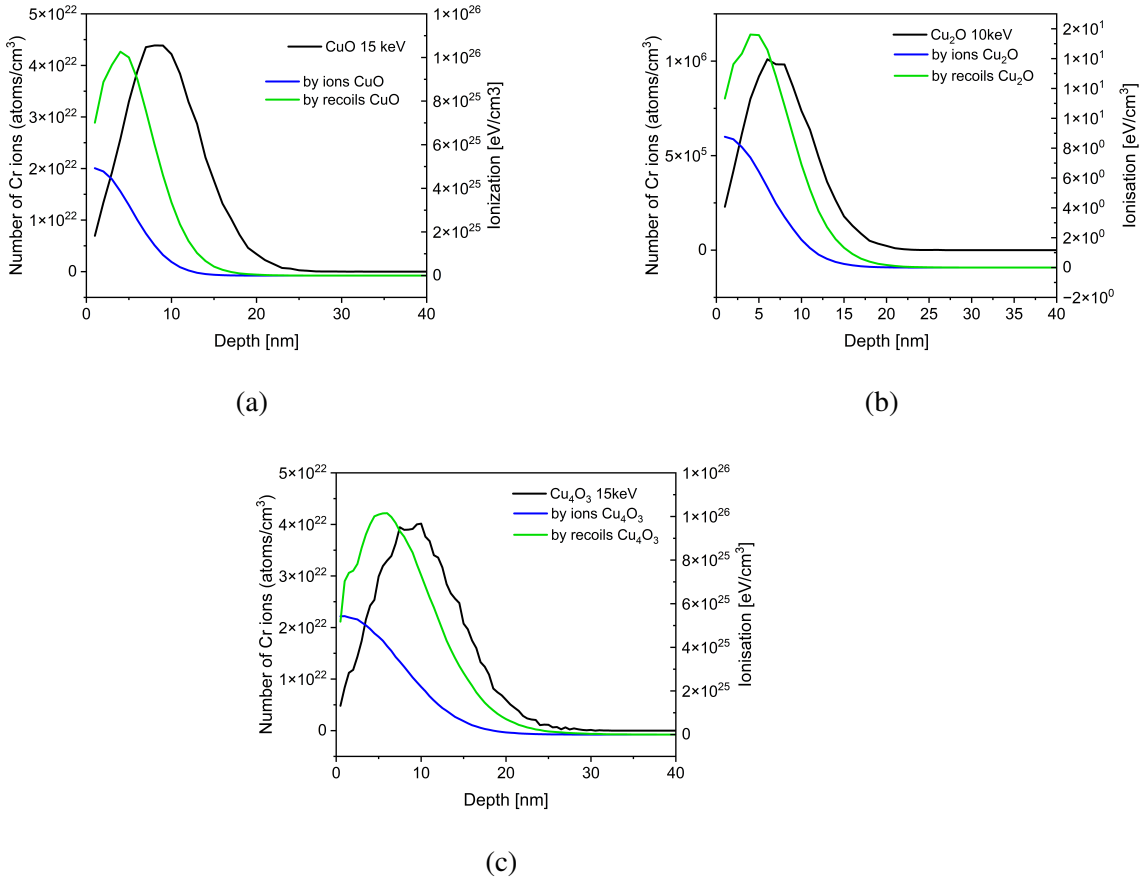

Figure 4.2. Depth distribution of Cr ions and ionisation induced by ions and recoils in (a) CuO implanted with Cr ions of 15 keV energy, (b) Cu_2O implanted with Cr ions of 10 keV energy, (c) Cu_4O_3 implanted with Cr ions of 15 keV energy.

For each oxide the distribution of Cr atoms, and the ionisation induced in the material by ions and recoils are presented in Figure 4.2c. Simulations used to achieve these results were performed for 30 000 implanted ions. In every case a clear peak of ions distribution is visible, for CuO around 9 nm, for Cu_4O_3 around 10 nm, and for Cu_2O at around 8 nm, the last one was simulated for lower energy of ion beam. It is clear that the ions ionise the material near the surface of it, and more in depth the recoiled atoms transfer more energy. The difference between CuO and Cu_4O_3 simulation results are due to different density and ration of atoms in these oxides. Copper and oxygen have different displacement energies and will interact differently with Cr ions.

In Figure 4.3 the visualisation of recoil cascades caused by implantation is presented. Each grey ball represents a Cr ion, and red and blue balls represent copper and oxygen atoms, respectively. An energised ion knocks the target atoms of their positions, and if an atom has enough energy, it knocks another one, creating recoil cascades. Here result of only 10, 100 and 1000 implanted

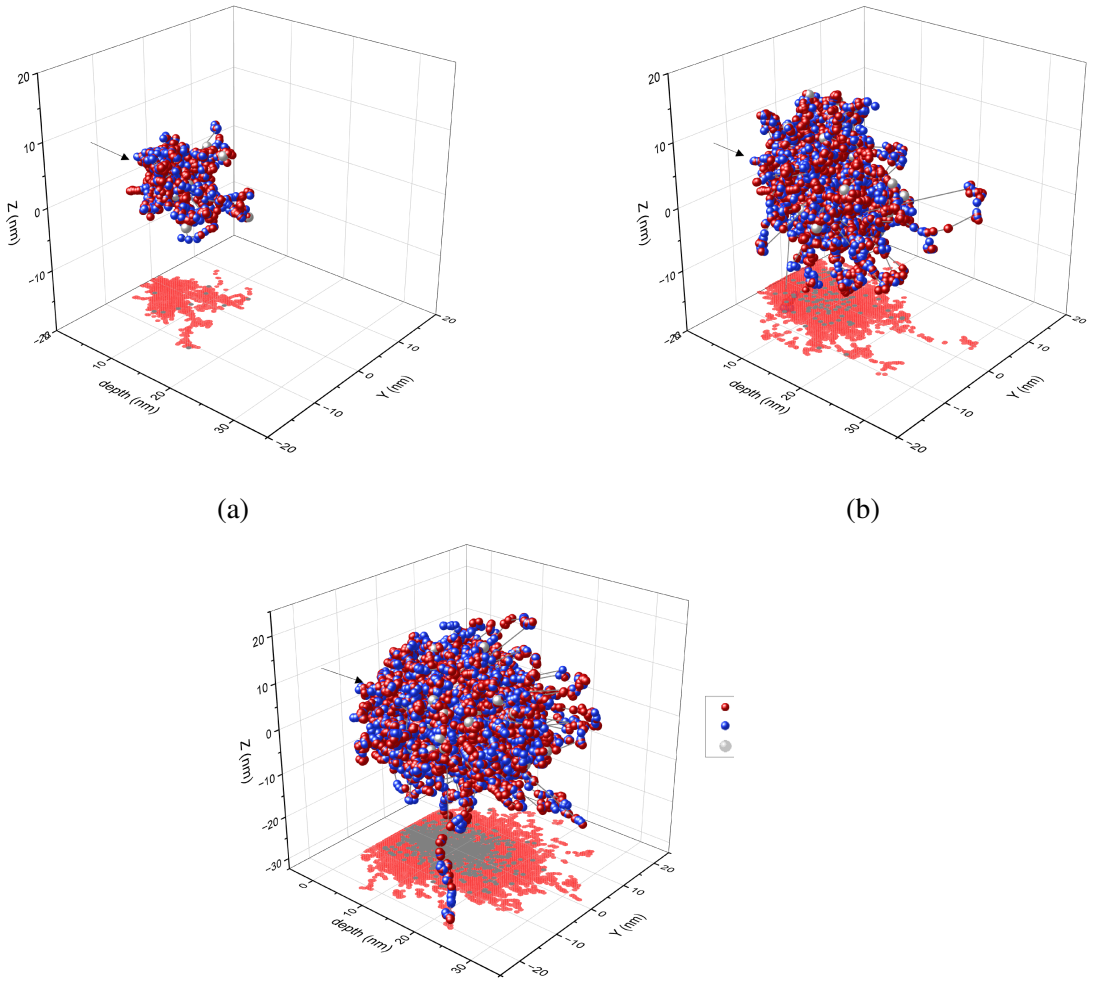

Figure 4.3. Visualisation of recoil cascades for CuO implanted with 15 keV Cr ions for (a) 10, (b) 100, and (c) 1000 simulated ions. Balls represent atoms: red - Cu, blue - O, grey - Cr.

ions are shown. Actually, creation of such figure for more ions was an extremely hard task for a personal computer. This illustration shows also how the atoms and ions spread energy and damage in the lateral direction to the beam in contrast to results in Figure 4.2a. The simulation was carried out for ions with a 0°angle of incidence, where the beam enters the target at a single point which is marked with an arrow in the figure. Though the ions reach no further than 25 nm in depth, the recoils reach beyond 30 nm into the material. Combining it with the information that Figure 4.1 represents, the damage introduction into the film will be much further than 30 nm.

SRIM simulations give opportunity to estimate the depth at which a semiconductor can be doped with implanted element. This can prove useful in all-oxide photovoltaics as for example to introduce back surface field effect as proposed by Zhu et al. [86] through doping of p-type absorber near interface with rear contact. This solution is only theoretical and in their next simulation [87] they stated that presence of defects, which is inevitable, negates this positive effect. Nevertheless,

ion implantation gives unique possibility to introduce an exact amount of dopant into a desired part of the material, and SRIM software is an excellent tool to choose the energy of ion implantation.

4.3 CuO

4.3.1 Structural properties

X-ray diffraction measurements were conducted on CuO samples deposited on silicon substrates to analyse the impact of ion implantation on the phase composition and crystallinity of the thin-film copper oxides, and to verify the deposition of the correct oxide. The measurements were carried out using a PANalytical X'Pert PRO diffractometer equipped with a Cu anode (0.154 nm radiation wavelength). The measurement step was 0.05°with time per step of 8000 s. Prior to analysis, the XRD patterns were processed to remove background noise and the contribution from the Kα2 characteristic radiation of the Cu anode using X'Pert HighScore software. No chromium compounds were detected using the XRD method, which could be due to either the absence of crystalline structures formed by Cr or their presence in quantities too small to be detected by this technique. To estimate the thickness of samples X-ray reflectivity measurements were done, with the same apparatus and with following measurement parameters: the angular range 0.2–3.0°, step 0.003°, and time per step 10 s.

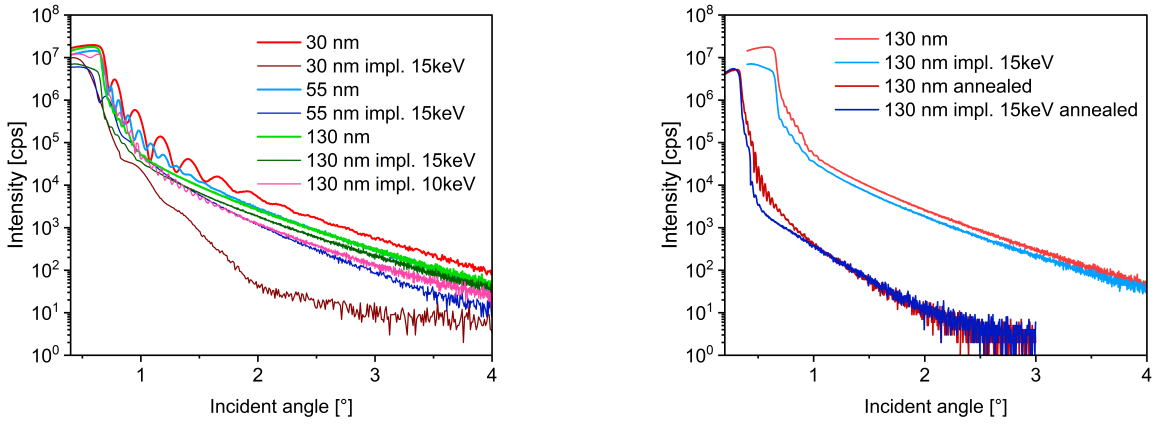

(a) (b)

Figure 4.4. Reflectivity curves of CuO samples (a) with different thickness before and after implantation and (b) before and after annealing. The sample implanted with 10 keV was implanted with dose of 1x10^{15} cm^{-2}.

The reflectivity curves of CuO samples are shown in Figure 4.4. It was not possible for all samples to determine the thickness of the film. The thinnest CuO film of 30 nm shows clear interferences that were calculated to 32 nm thickness, while sample after implantation has almost no

interferences. Moreover, the slope of intensity is much higher indicating increased roughness of film. For all samples, except for 10 keV implanted one, the interferences attenuate after the implantation and the critical angle decreases which indicates decrease in films' density. The effect of annealing that can be observed is that the implanted sample exhibits an abrupt decrease in signal intensity (Figure 4.4b), indicating the presence of distinct layers within the film. This suggests that the region closer to the surface differs significantly in physical properties from the material beneath it [88]. Thickness calculated based on the space between interference fringes are presented in Table 4.2.

Table 4.2. Thickness of CuO films determined from X-ray reflectivity measurements.

Sample	Thickness [nm]
30 nm	32
30 nm impl.	-
55 nm	68
55 nm impl.	-
130 nm	152
130 nm 15 keV impl.	96
130 nm 10 keV impl.	126
130 nm annealed	117
130 nm impl. annealed	102

In Figure 4.5a diffractograms of samples of 30 nm, 55 nm, and 130 nm thickness both before and after implantation with 15 keV ions are presented. Clear CuO peaks are evident in all samples, as indicated using ICDD card #01-080-0076. After implantation, the 30 nm layer appears completely amorphous, with no visible peaks remaining. The 55 nm sample exhibits peaks corresponding to Cu (ICDD card #00-001-1242) and Si (ICDD card #00-001-0787), but no distinct CuO peaks are observed. In contrast, the thickest sample (130 nm) still displays CuO peaks post-implantation. The implanted ions lose energy primarily through excitation of the target's electrons or collisions with nuclei, with nuclear stopping being the dominant mechanism in the keV energy range [89]. These collisions displace target atoms from their positions in the crystal lattice, leading to crystal structure damage or amorphisation when sufficient ions are implanted. Additionally, some atoms may be sputtered from the target, which could explain the absence of a signal from the implanted 30 nm sample. Based on this data, it can be inferred that ion implantation significantly affects the crystal structure up to a depth of 55 nm, while thicker layers remain largely undamaged, retaining their crystalline structure beyond the ion implantation range.

Figure 4.5b presents the diffractograms of samples implanted with 10 keV energy ions at varying doses. The most prominent peaks observed are (111) and (-111) combined with (200) and

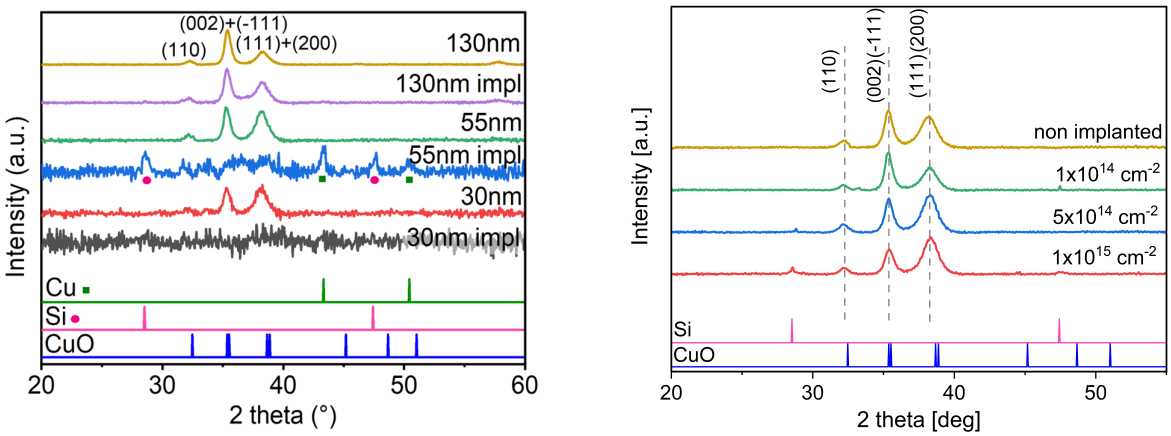

(a) (b)

Figure 4.5. Diffractograms of CuO samples (a) of different thickness implanted with 15 keV Cr ions, (b) all 130 nm implanted with 10 keV Cr ions of different doses.

(002), along with the visible (110) peak. The relative intensities of these major peaks change after implantation, suggesting the possibility of thin film texturisation. Specifically, in samples implanted with 10 keV ions at higher doses, the intensity of the (002) + (-111) peak decreases, while the intensity of the (111) + (200) peak increases. A notable change in this intensity ratio is observed when comparing the non-implanted sample to the sample implanted with a 10 keV ion dose of $1x10^{15}$ cm^{-2}. However, when comparing the non-implanted 130 nm sample with the one implanted with 15 keV ions at a dose of $5x10^{16}$ cm^{-2}, the change in intensity ratio is much less pronounced. This indicates that implantation at higher energies, even with a higher ion dose, has a reduced effect on the texturisation of the thin film.

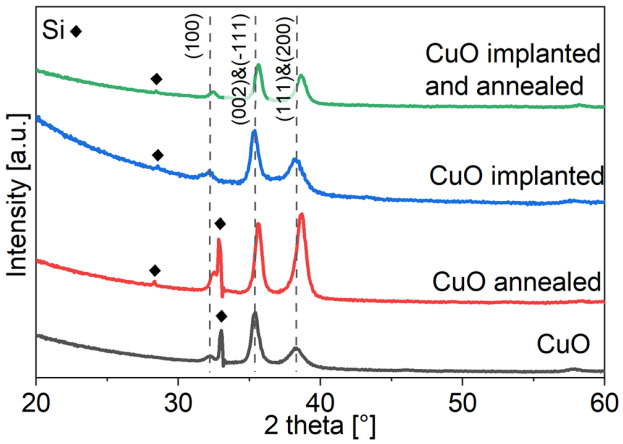

Figure 4.6. Diffractograms of CuO 130 nm samples after implantation and annealing.

Lattice parameters for all 130 nm samples were calculated using the positions of the (110), (-111) and (-311) peaks. The (-311) peak, present at 2 theta angle around 61°, is not shown in the figures to maintain clarity in the data presentation and to avoid interference from the strong Si

Table 4.3. Calculated lattice parameters of CuO samples after Cr ion implantation and annealing.

Sample	*a* [Å]	*b* [Å]	*c* [Å]	β [°]
non-implanted	4.67	3.47	5.15	98.61
dose 1x10^{14} cm^{-2} energy 10 keV	4.66	3.49	5.13	98.65
dose 5x10^{14} cm^{-2} energy 10 keV	4.66	3.49	5.10	98.62
dose 1x10^{15} cm^{-2} energy 10 keV	4.66	3.48	5.10	98.61
dose 5x10^{16} cm^{-2} energy 15 keV	4.66	3.47	5.21	98.62
non-implanted annealed	4.66	3.49	5.13	98.71
dose 5x10^{16} cm^{-2} energy 15 keV annealed	4.69	3.43	5.10	98.91

peak near 70°, which could overshadow the peaks of interest. Additionally, lattice parameters were determined for a sample implanted with 15 keV ions at a dose of 5x10^{16} cm^{-2} and subsequently annealed in air at 400°C for 6 hours. The diffractogram of this annealed sample is displayed in Figure 4.6.

The calculation of CuO monoclinic crystal structure lattice parameters *a*, *b*, *c* and β follow Equations 4.1 - 4.5. Equation 4.1 is for interplanar distance calculation for monoclinic structure and using the *h*, *k*, *l* values of (100) (-111) and (-311) peaks other equations were calculated.

$$\frac{1}{d_{hkl}^2} = \frac{h^2}{a^2 sin^2\beta} + \frac{k^2}{b^2} + \frac{l^2}{c^2 sin^2\beta} - \frac{2hlcos\beta}{acsin^2\beta} \tag{4.1}$$

$$cos\beta = \frac{\sqrt{2}}{2}\left(\frac{1}{d_{-111}^2} - \frac{1}{d_{111}^2}\right) - \frac{1}{\sqrt{\frac{1}{d_{-311}^2} - \frac{1}{d_{-111}^2} + \frac{1}{d_{111}^2}}} - \frac{1}{\sqrt{\frac{1}{2d_{-111}^2} - \frac{1}{d_{110}^2} + \frac{1}{2d_{111}^2}}} \tag{4.2}$$

$$a = \frac{2\sqrt{2}}{sin\beta}\frac{1}{\sqrt{\frac{1}{d_{-311}^2} - \frac{1}{d_{-111}^2} + \frac{1}{d_{111}^2}}} \tag{4.3}$$

$$c = \frac{1}{sin\beta}\frac{1}{\sqrt{\frac{1}{2d_{-111}^2} - \frac{1}{d_{110}^2} + \frac{1}{2d_{111}^2}}} \tag{4.4}$$

$$b = \frac{asin\beta d_{110}}{\sqrt{a^2 sin^2\beta - d_{110}^2}} \tag{4.5}$$

The calculated lattice parameters are listed in Table 4.3. The calculated lattice constant *c* and crystallographic angle β do not seem to change substantially with the dose of implantation. The *c* constant value decreases with an implantation of lower energy and increases for the most intensive implantation. An opposite trend can be seen in the case of the *b* constant, which increases its value for doses used with 10 keV ions, and decreases for highest dose used with 15 keV ions. When comparing two samples with the highest ion doses and different energies, it is clearly noticeable that the *c* parameter has a higher value for 15 keV implantation. This parameter value for samples implanted with 10 keV of energy of Cr ions falls with increasing dose of implantation, so energy

seems to be the deciding implantation parameter here. The parameter a does not have noticeable change neither with implantation nor annealing. Annealing of non-implanted sample reduced a and c parameters, and increased b and β. In case of implanted sample annealing caused decrease of c parameter and the β angle. A clear effect as seen in Figure 4.6 is that annealing changes the ratio of (002) + (-111) to (111) + (200) peaks intensity, which can be observed for both implanted and non-implanted samples.

XRD measurements showed that ion implantation has the most impact on crystal structure up to 60 nm of the film. Thicker samples still show clear peaks coming from CuO monoclinic structure. The changes of lattice parameters caused by implantation and annealing were assessed, and these changes are insignificant, and no clear dependence is observed. One can be said, that annealing results with more intense peak and changes in peak intensity ratios. Moreover, peaks shift to higher angles which can be caused by changes is stress present in the material, where implantation introduces stress into structure and annealing relaxes it.

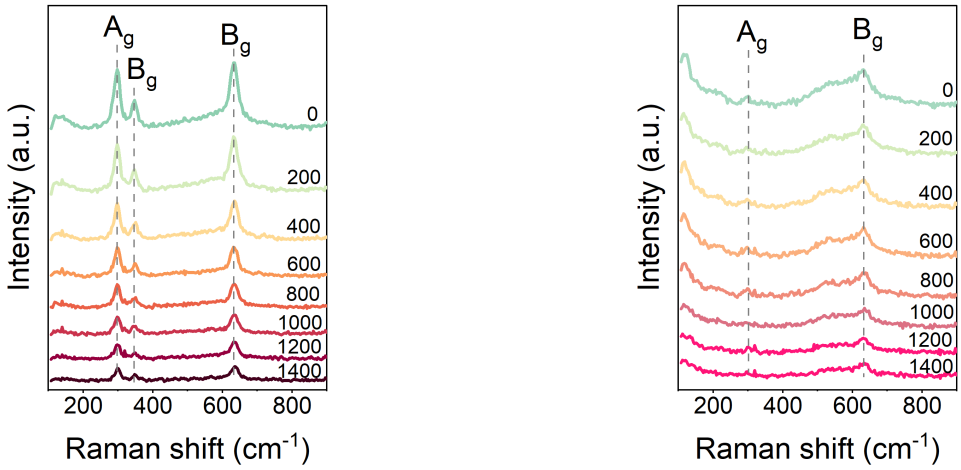

(a) (b)

Figure 4.7. Raman spectra of 1550 nm thick CuO (a) as deposited, (b) after implantation.

Raman spectroscopy is a valuable tool for studying the structure of materials through their vibrational properties. Raman spectra for 1550 nm CuO samples were obtained using a WITec Alpha 300M+ spectrometer with 488 nm diode laser, 100x lens, with resolution of 3 cm^{-1} (lattice 600). Each measurement lasted for 100 s, with 20 seconds per 5 accumulations. The laser was focused at varying depths within the sample. The resulting spectra are shown in Figure 4.7a for the non-implanted sample and in Figure 4.7b for the sample implanted with 15 keV Cr ions at a dose of $5x10^{16}$ cm^{-2}. For the non-implanted sample, the Raman spectrum clearly reveals CuO bands, with three Raman-active modes observed: A_g 319 cm^{-1}, B_g 382 cm^{-1} B_g 629 cm^{-1}. The sample after implantation shows only two bands with a significantly lower signal-to-noise ratio, consistent with the fact that ion implantation can induce a decrease in Raman band intensity [90]. Addi-

tionally, a new band appears at 116 cm^{-1} in the implanted sample signal. CuO does not exhibit Raman-active vibrational modes at this frequency, but this band corresponds to another copper oxide, Cu_2O, which typically shows bands in Raman spectra even though they are theoretically infrared-allowed modes [91, 92]. A broad band around 540 cm^{-1}, corresponding to Cu_2O only Raman-active vibration mode, T_{2g}, is also present. This suggests that Cu_2O may be present in this sample, or that ion implantation has introduced significant non-stoichiometry. Another consideration is that ion implantation affects the material up to a depth of 60 nm, leading to a reduction in signal intensity due to light absorption by the material and substrate. The differences in visible bands likely result from probing closer to the film's surface, therefore this method does not give significant insight into depth of material.

4.3.2 Density of states calculation with Density Functional Theory

In advanced solid materials research, which hold significant technological importance, it is crucial to understand material properties at the atomic level. Currently, Density Functional Theory (DFT) is the most effective method for studying the electronic structure of matter. DFT is widely used in various fields, including solid-state physics, physical chemistry, modern electronics, metallurgy, geoscience, biochemistry, and any other discipline that requires insight into material properties at the atomic scale. It is applicable to atoms, molecules, solids, liquids, and plasmas [93, 94]. DFT has become the preferred tool for most researchers, partly due to the availability of commercial DFT software.

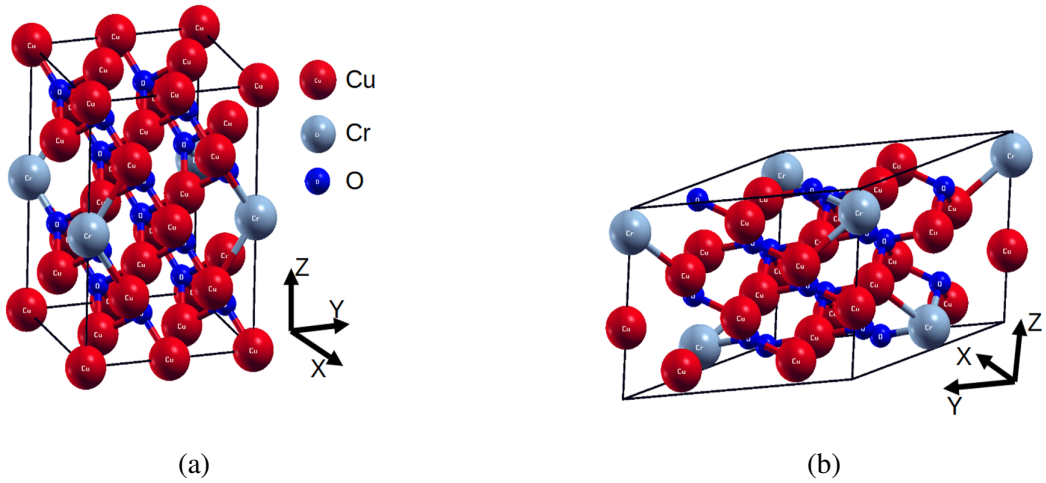

(a) (b)

Figure 4.8. Structures used in DFT calculations (a) $Cu_{15}CrO_{16}$ and (b) Cu_7CrO_8 [95].

The calculations of which results are presented in this section, were performed at Faculty of Physics and Applied Computer Science AGH University of Krakow. The calculations were executed with WIEN2K software package, which is popular and easily available [96]. The calculations were carried out using General Gradient Approximation [97]. The calculated electron structure is at

ground state (0 K temperature), from it is possible to determine density of states, energy band gap value and electromagnetic radiation absorption. Additionally, for the Cu and Cr d-states, orbital-dependent potentials using LDA + U(SIC) with an effective potential of 0.52 Ry were applied [98].

The starting point of calculations was CuO structure C2/c (ITC 15) with lattice parameters as calculated for annealed CuO films: a = 4.66 Å, b = 3.49 Å, c = 5.13 Å, $\alpha = \gamma = 90°$, β = 98.71°. This structure was expanded by a factor of 2 × 2 × 2 to accommodate the appropriate initial antiferromagnetic spin arrangement on the Cu sites [99]. The second structure considered involved substituting one chromium atom in place of a copper atom, resulting in the composition $Cu_{15}CrO_{16}$. After accounting for symmetry, this structure was reduced to the P-1 (ITC 2) space group with lattice parameters a = 5.11 Å, b = 6.82 Å, c = 9.31 Å, $\alpha = \gamma = 90°$, and β = 99.48°(as shown in Figure 4.8a). A third system was created by randomly selecting two Cu atoms and replacing them with Cr atoms, yielding a Pc (7 ITC) structure with lattice parameters a = 9.85 Å, b = 9.31 Å, c = 6.82 Å, $\alpha = \beta = 90°$, and γ = 149.24°(depicted in Figure 4.8b). The electronic properties were calculated theoretically for two different Cr concentrations to demonstrate the changes that occur in the material when doped. The second system has a Cr concentration comparable to the atomic Cr concentration in a sample implanted with a dose of 5×10^{16} cm^{-2} and an energy of 15 keV.

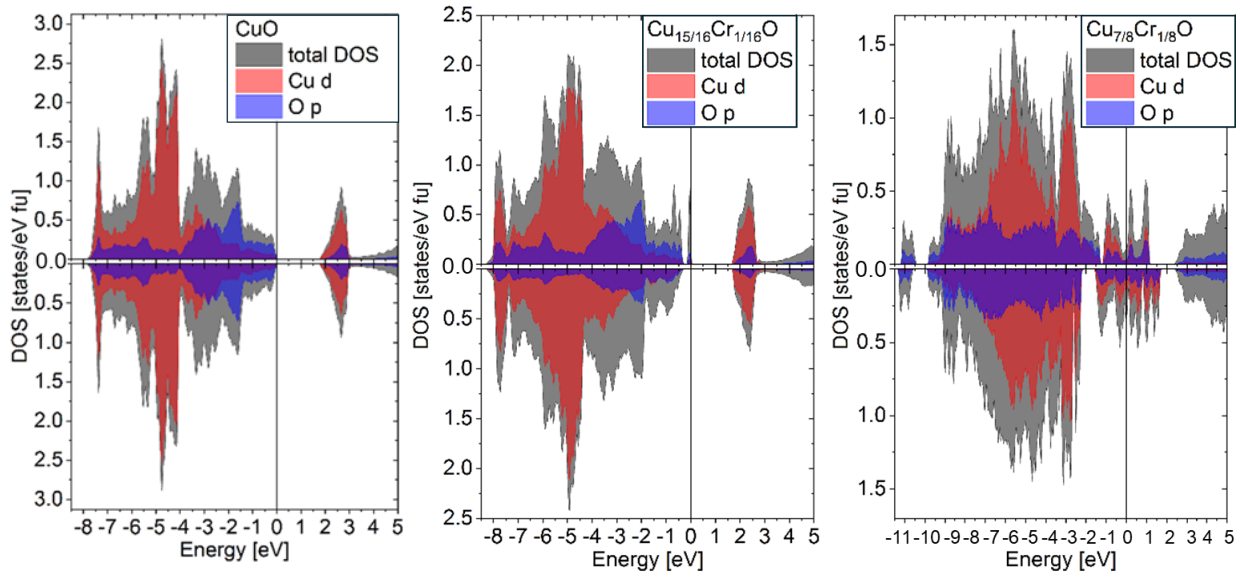

(a) (b) (c)

Figure 4.9. Density of states calculated for (a) pure CuO and doped (b) $Cu_{15}CrO_{16}$, (c) Cu_7CrO_8 [95].

The DFT calculations yield the Density of States which are presented for all three considered structures in Figure 4.9. The pure CuO has energy gap of 1.75 eV (Figure 4.9a) which is consistent with literature [100, 101]. It is important to notice that the calculations consider ground state, and the band gap value increases with temperature [102]. Therefore, the band gap observed at room

temperature will be smaller. The CuO doped with smaller amount of Cr, $Cu_{15}CrO_{16}$, has a very narrow half metallic conduction band at the Fermi energy level for electrons with spin up (Figure 4.9b). The energy band gap is 1.6 eV for spin up electrons and 1.9 eV for spin down electrons. Higher level of doping, with one Cr atom per seven Cu atoms, results with metallic conduction band (Figure 4.9c). The valence band is primarily formed by d-type Cu and p-type O electrons in all considered structures.

To calculate the absorption of light a scheme for the calculation of linear optical properties by the all-electron full-potential linearised augmented planewave (LAPW) method was used [103]. The resulting absorption energy spectrum are presented in Figure 4.10. In CuO, absorption starts for photons with energies greater than 1.7 eV (Figure 4.10a). When the Cr dopant concentration is at one atom per 15 Cu atoms, absorption increases significantly starting from 1.6 eV (Figure 4.10b). In the case of Cu_7CrO_8, absorption begins at even lower energies (Figure 4.10c).

It should be noted that the DFT calculations assume a perfect crystalline material at 0 K. In contrast, the actual sample is a polycrystalline thin film with inherent defects. As a result, the predicted behaviour from the DFT simulations — such as the metallic character of doped CuO and a distinct change in light absorption — may not be observed in practice. Nevertheless, the calculations indicate that doping CuO with Cr should enhance its electrical conductivity.

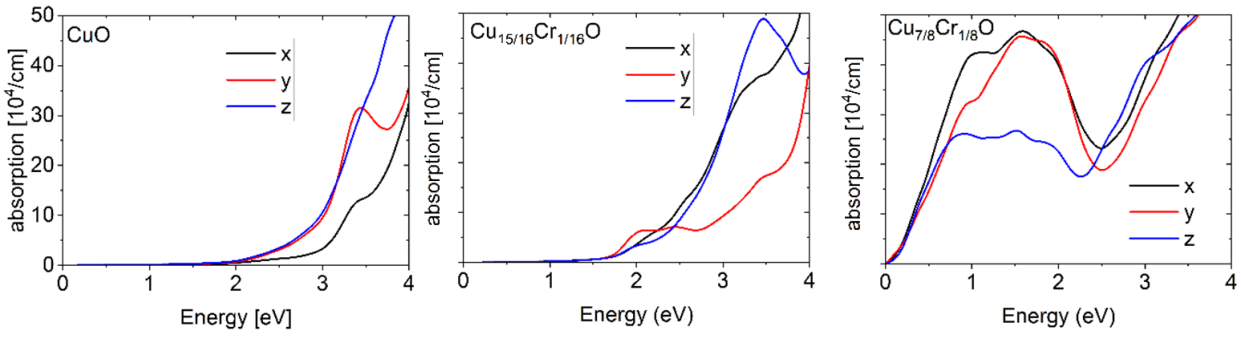

(a) (b) (c)

Figure 4.10. Absorption of light calculated for (a) pure CuO and doped (b) $Cu_{15}CrO_{16}$, (c) Cu_7CrO_8 [95].

4.3.3 Optical properties

Optical properties of CuO were characterised with spectrophotometric measurements of absorbance and with spectroscopic ellipsometry method. Spectrophotometry measurements were conducted in transmission mode using an AvaLight-DH-S-BAL source and AvaSpec-ULS-RS-TEC detector, while all ellipsometry measurements were carried out with a J.A. Woollam M-2000 ellipsometer.

Table 4.4. Energy band gap determined using Tauc plot method for CuO samples.

Sample	E_g [eV]
non-implanted	1.10
dose 1x10^{14} cm^{-2} energy 10 keV	1.17
dose 5x10^{14} cm^{-2} energy 10 keV	1.18
dose 1x10^{15} cm^{-2} energy 10 keV	1.16
non-implanted annealed	1.13
dose 1x10^{14} cm^{-2} energy 10 keV annealed	1.20
dose 5x10^{14} cm^{-2} energy 10 keV annealed	1.20
dose 1x10^{15} cm^{-2} energy 10 keV annealed	1.19

Figure 4.11a displays the absorbance of non-implanted CuO thin films and those implanted with 10 keV ions at various doses.

The band gap of the material can be estimated from absorbance measurements using the Tauc plot method. For CuO, which has an indirect allowed transition, the plot is generated according to Equation 4.6, where α is absorption coefficient, *h* is Planck's constant, ν is frequency of photons, *B* is a constant value, E_g is the band gap. The band gap value is calculated as E_g = - *intercept/slope* of a line fitted to the plot. Tauc plots for CuO samples implanted with 10 keV ions are shown in Figure 4.11b, and for CuO after implantation and annealing in Figure 4.11d. The optical band gaps determined from these plots are summarised in Table 4.4.

$$(\alpha h\nu)^{\frac{1}{2}} = B\,(h\nu - E_g) \tag{4.6}$$

Ion implantation reduced the light absorption of CuO thin films, showing an approximately exponential decrease with increasing implantation dose, as shown in the inset of Figure 4.11a. These effects are detrimental to the films' effectiveness as absorber layers in solar cells. However, annealing the implanted material improves the situation. Although the band gap remains significantly higher than that of the as-deposited CuO, the absorbance, and thus the light absorption, increases across the energy spectrum. The implanted and annealed samples achieve the same level of absorption as the non-implanted sample (Figure 4.11c). The difference in light absorption between CuO and the doped samples is less pronounced than predicted by DFT simulations. This discrepancy arises because DFT calculations assume a perfect crystal structure at 0 K, whereas the actual samples are thin, polycrystalline films measured at room temperature.

Spectroscopic ellipsometry (SE) was employed to evaluate the changes in optical parameters following implantation, particularly focusing on the refractive index *n* and the extinction coefficient *k*, the latter of which is directly related to the absorption coefficient as:

$$\alpha = \frac{4k\pi}{\lambda} \tag{4.7}$$

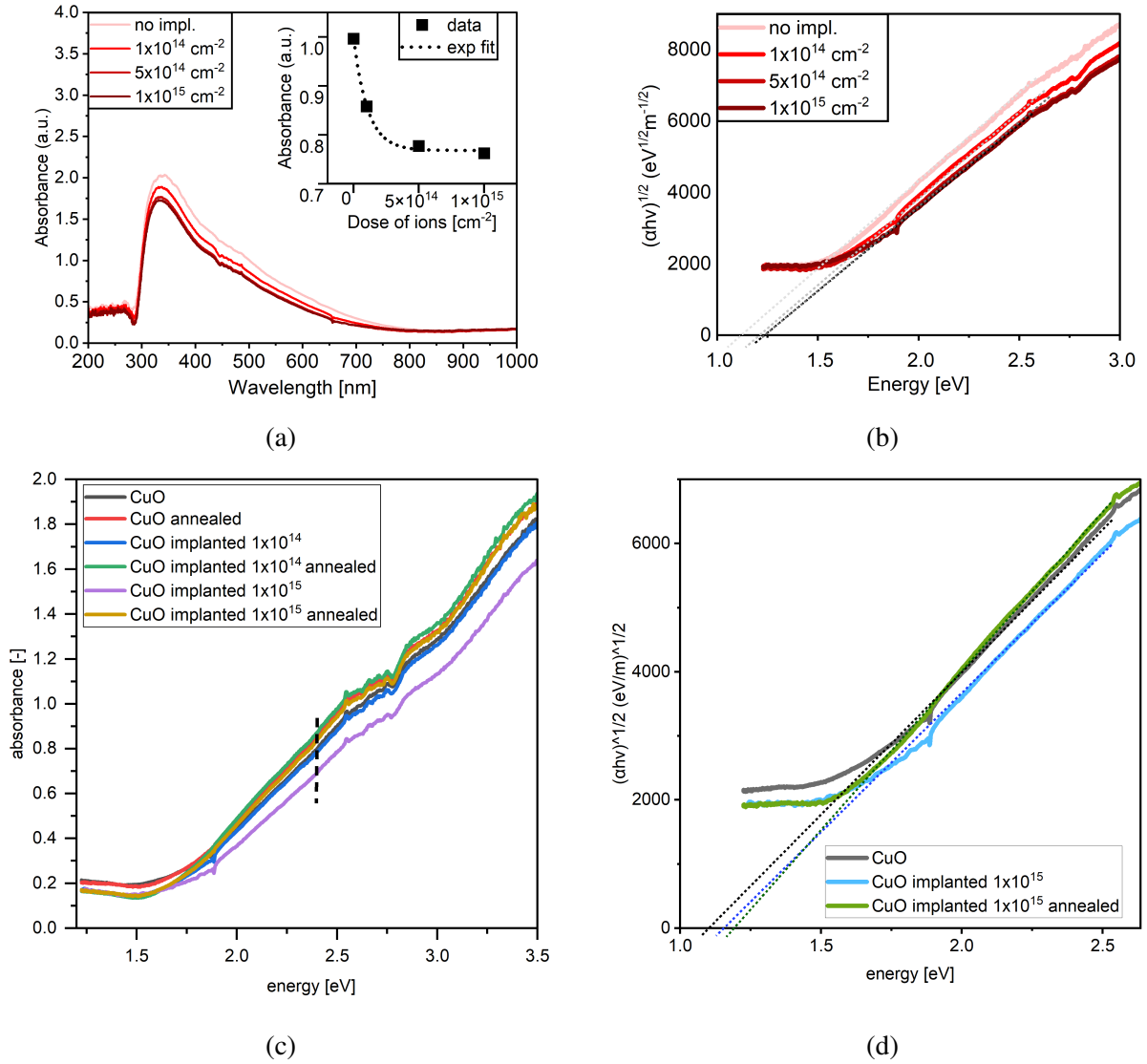

Figure 4.11. Optical properties of CuO thin films implanted with Cr ions of different dose and energy: (a) absorbance of CuO films after Cr ion implantation; (b) Tauc plot for CuO films implanted with 10 keV Cr ions. (c) Absorbance of CuO after implantation and/or annealing, (d) Tauc plot of implanted and annealed CuO. The dashed line in (c) marks wavelength used to prepare plots in Figure 4.18

where λ is wavelength of light. In spectroscopic ellipsometry method a polarised light beam is directed onto a thin film sample. After reflecting from the surface, the light reaches a depolariser and then a detector. The changes in light polarisation upon reflection contain information about the material's optical properties, thickness, and roughness. The two parameters that describe these changes are Psi Ψ and Delta Δ, which are the outcomes of the measurement. They are defined by the ratio of the amplitude reflection coefficients for p- and s-polarisations of light [104]:

$$\rho \equiv tan\Psi e^{i\Delta} \equiv \frac{r_p}{r_s} = \left(\frac{E_{rp}}{E_{ip}} / \frac{E_{rs}}{E_{is}}\right) \tag{4.8}$$

where E_{ip} and E_{is} are amplitudes of two components of incident beams, E_{rp} and E_{rs} of reflected beam. The Psi parameter represents the amplitude ratio, while Delta indicates the phase difference between p- and s-polarised light. Using these parameters, the refractive index and extinction coefficient can be directly calculated through Fresnel equations. The analysis of all ellipsometric data was performed using CompleteEASE software, specifically designed for use with the J.A. Woollam M-2000 ellipsometer.

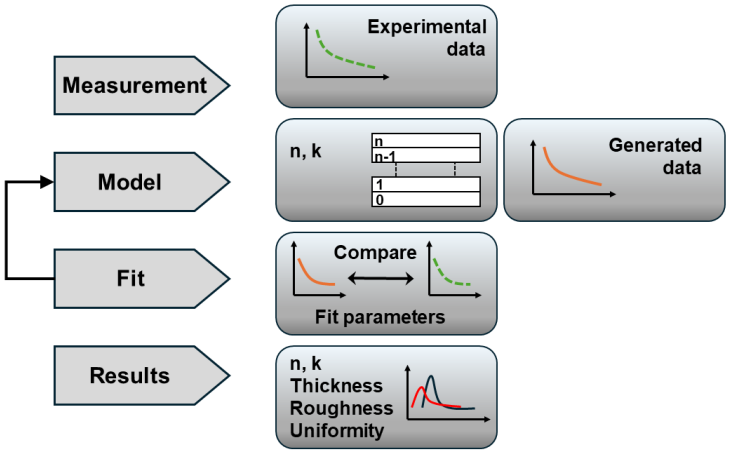

Figure 4.12. Flowchart of data analysis in spectroscopic ellipsometry [105].

In ellipsometry, accurate data analysis requires a model of the material under study. Through fitting and iterative processes, detailed information about the sample can be extracted, as illustrated in Figure 4.12. The model must account for the substrate and include appropriate mathematical functions to describe the deposited films. A roughness layer is often included in the model, typically calculated as a combination of 50% void and 50% of the underlying layer. Since the optical properties of materials stem from their electronic properties — specifically, the energy transitions between different levels — it is reasonable to base the model on this information. Meyer et al. identified the transitions present in copper oxides through electronic property calculations [39]. Models based on this data were developed to specifically analyse the impact of implantation on copper oxides.

Model for CuO is based on energy transitions that occur at energies: 1.66 eV, 2.07 eV, 2.68 eV, 3.46 eV, 6.00 eV. For each of them a Tauc-Lorentz oscillator function is used (Equation 4.3.3). The measured data was first fitted using B-spline mathematical function and then parametrised using the oscillators which directly represent the imaginary part of dielectric function ε_2. The real part is automatically calculated via Kramer-Kroenig relations [105].

$$\varepsilon_{TL} = \varepsilon_1 - i\varepsilon_2$$
$$\varepsilon_2 = \left[\frac{AmpE_0Br(E-E_G)^2}{(E^2-E_0^2)^2+Br^2E^2}\cdot\frac{1}{E}\right], E > E_g \tag{4.9}$$
$$\varepsilon_2 = 0, E \leq E_g$$

The model for CuO consists of a Si substrate, three layers of CuO, and a roughness layer. Each CuO layer consists of 5 Tauc–Lorentz oscillators. As the model is multi-layered, to calculate the total thickness of the film, we need to add the thicknesses of three oxide layers and half of the roughness layer. The fitted thicknesses and corresponding mean squared errors for selected samples are shown in Figure 4.13. The samples include non-implanted CuO, a sample implanted with 15 keV energy and 5x10^{16} cm^{-2} dose, and a sample implanted with 10 keV energy and 1x10^{14} cm^{-2} dose.

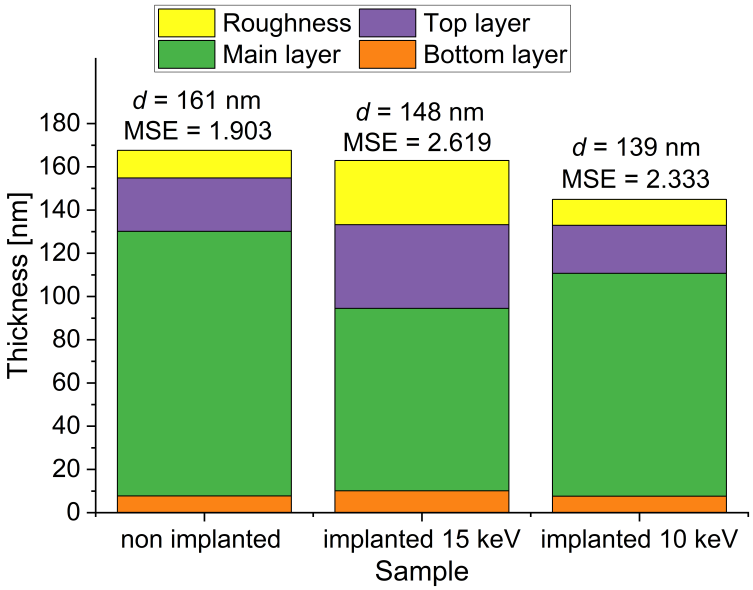

Figure 4.13. Model results after fitting for chosen CuO samples. Bottom layer represents interface between deposited layer and the substrate, top layer with roughness are layers that were influenced by implantation.

The roughness layer is thicker in implanted samples compared to non-implanted ones in every case. The total thickness of the films differs from the intended thickness during the deposition process, which could be attributed to variations in deposition conditions or limitations of the SE method, which is an indirect measurement technique. In the model, the bottom layer's role is to represent the interface between the substrate and the deposited oxide, so its optical properties are not considered in the analysis. Figure 4.14 shows that the absorption coefficient of the main CuO layer decreases after implantation, resulting in an increase in the energy band gap. The slope of the absorption coefficient for the top layer is significantly reduced after implantation, suggesting an

Table 4.5. Energy of transitions in CuO and fitted positions of oscillators.

Energy transition [eV]	non-implanted	1x10^{14} cm^{-2} 10 keV	5x10^{16} cm^{-2} 15 keV
	Oscillator energy (eV)		
1.66	0.608	0.756	0.348
2.07	1.633	1.472	1.504
2.68	2.293	1.697	2.789
3.46	3.542	3.061	3.452
6	6.386	7.736	5.718

increase in Urbach energy and greater absorption due to defects. The absorption coefficient of CuO decreases following implantation, with the properties of the top layer showing more pronounced changes than those of the main layer. The fitted positions of the oscillators are presented in Table 4.5. Interestingly, the oscillator positions for the sample implanted with lower energy ions deviate more from the literature values compared to the sample implanted with higher energy ions.

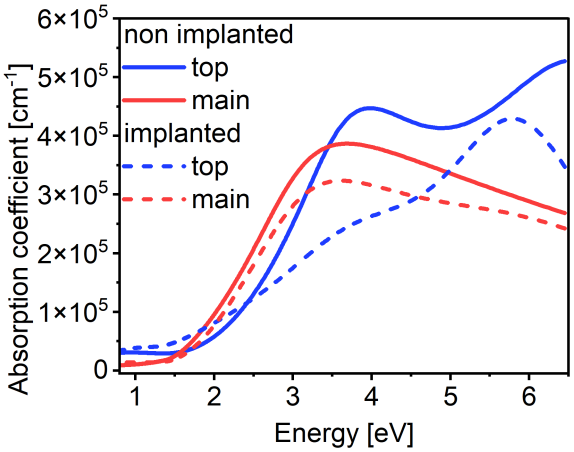

Figure 4.14. Absorption coefficient calculated from fitted model. Results for non-implanted CuO and implanted with 15 keV energy ions.

The refractive index value decreases from 2.5 to 1.5 with increasing energy (Figure 4.15a), which is consistent with the literature [106]. After implantation, the values of both n (refractive index) and k (extinction coefficient) remain nearly unchanged for the main layer. However, for the top layer, their values decrease significantly, n from a maximum of 2.5 to 2.2, and k drops from nearly 1.2 to below 0.8, with the peak value of k shifting to higher energies. The reduction in absorption for both oxides is primarily due to a decrease in the amplitude or position shifts of oscillators at energy positions around 3.5 eV. This analysis highlights that the top layer is more significantly affected by the implantation process.

The next crucial step is the analysis of samples after annealing. The previous analysis focused on samples deposited on silicon, but samples deposited on glass will be discussed. The change

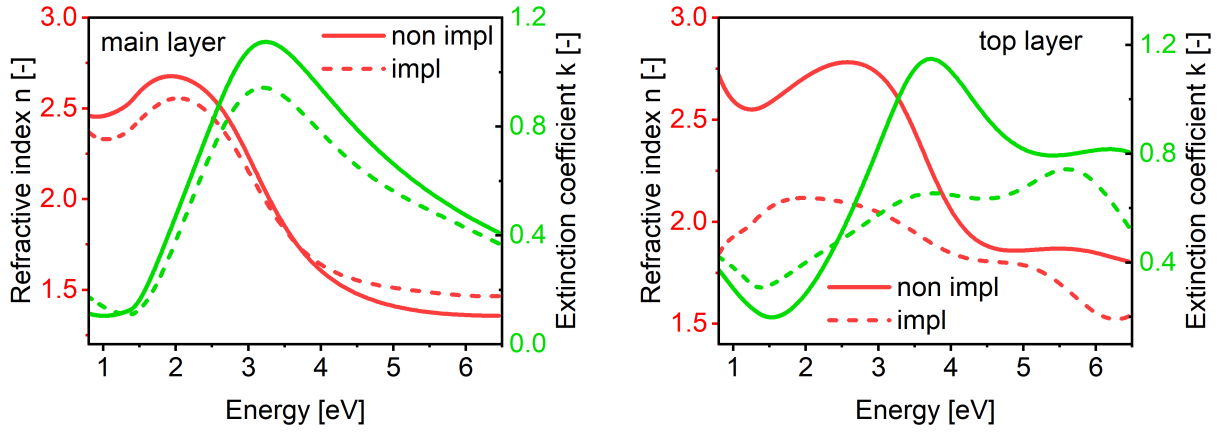

(a) (b)

Figure 4.15. Refractive index and extinction coefficient of CuO thin films (a) main layer and (b) top layer of the model for sample implanted with 15 keV energy ions.

in substrate has significantly affected the ellipsometry model. Instead of the five Tauc-Lorentz oscillators used previously, only four oscillators are now present, as including a fifth oscillator noticeably reduced the fit quality. Additionally, it was necessary to restrict the fitting range to wavelengths longer than 330 nm.

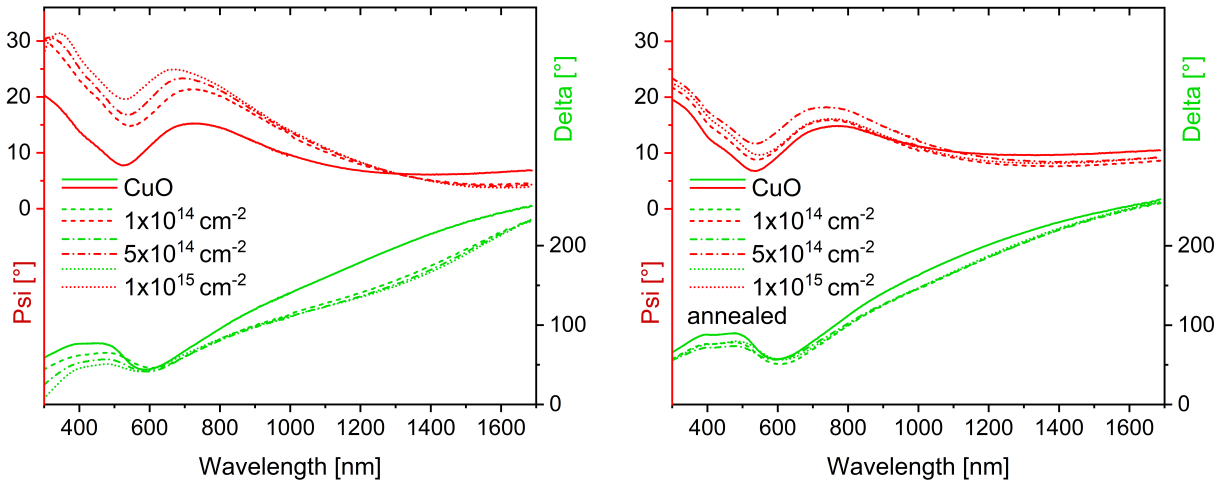

(a) (b)

Figure 4.16. Psi and Delta data obtained at 70°incidence angle for samples with different dose of implantation of 10 keV energy ions (a) before and (b) after annealing.

Psi and Delta values measured only for 70 °incident angle, which was chosen as close to Brewster angle for CuO, are presented in Figure 4.16. The most noticeable difference related to ion dose is observed in the Psi parameter. Higher doses result in Psi values that deviate further from those of the non-implanted sample, though these differences become much smaller after anneal-

ing. For the Delta parameter, the most notable changes occur in the 800 nm to 1600 nm range, where values increase post-annealing and become almost identical across all samples. Since the absorption coefficient can be directly derived from the Delta parameter, these changes indicate that ion implantation decreases the absorption of CuO thin films, while annealing restores it, which is consistent with spectrophotometric measurements.

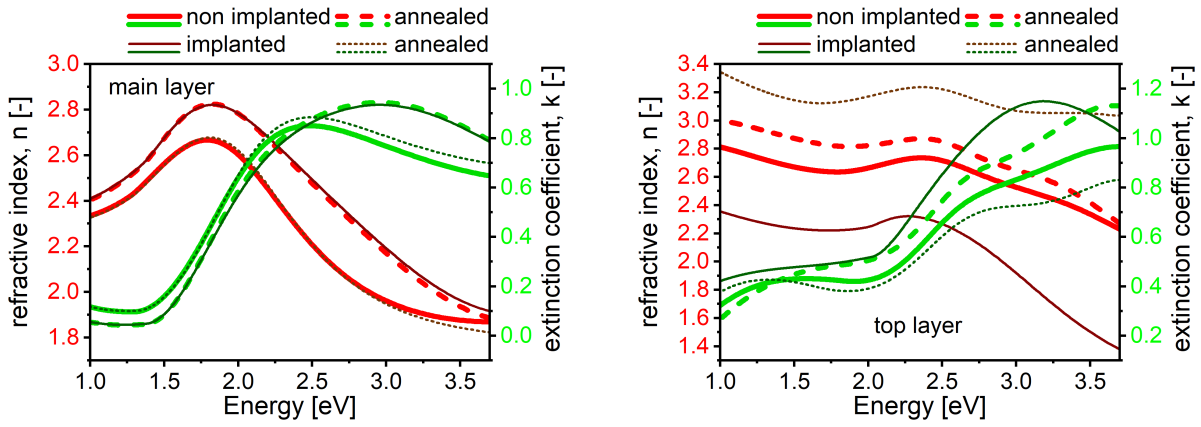

(a) (b)

Figure 4.17. Optical properties, refractive index n and extinction coefficient k, for (a) main layer and (b) top layer of non-implanted and implanted with dose 1x10^{14} cm^{-2} before and after annealing.

The results of fitting for samples deposited on glass are summarised in Table 4.6. The model used is multi-layered, with each CuO layer described by four Tauc-Lorentz oscillators. The substrate was represented by a Cauchy function. The mean square error for all fits is satisfactory. It is evident that annealing reduced the thickness of the roughness layer in each implanted sample. In some cases, the bottom layer thickness is minimal, yet it does not contribute significantly to the information about the film's properties. The thickness of the top layer remains consistent across all samples. The thickness of the main layer is slightly reduced in the implanted samples after annealing compared to before the thermal treatment. These results indicate that the annealing process modifies the properties of the implanted samples, making them more similar to those of non-implanted CuO. Annealing primarily affects the thickness of the main layer in CuO, consistent with its effect on other samples. This process is expected to induce crystallisation and grain growth within the film, altering optical density of thin films. Figure 4.17 displays the optical properties of two CuO films: one non-implanted and the other implanted with a dose of 1x10^{14} cm^{-2} at 10 keV energy. Presented properties are derived from the fitted models. Notably, the most significant differences are observed in the top layer, consistent with findings from models of samples deposited on silicon (Figure 4.13). Interestingly, the properties of the main layers show that the implanted sample, after annealing, closely resembles the non-implanted sample before annealing. It is possi-

Table 4.6. Spectroscopic ellipsometry data fitting results for samples after implantation with 10 keV energy Cr ions and/or annealing.

Sample	MSE [-]	Roughness [nm]	Top layer [nm]	main layer [nm]	Bottom layer [nm]	Total thickness [nm]
CuO	1.467	12.9	36.47	81.25	1.71	125.88
CuO annealed	1.874	12.08	35.5	70.1	2.87	114.51
1x10^{14} cm^{-2}	2.645	19.2	36.35	93.29	0.01	139.25
5x10^{14} cm^{-2}	1.916	22.11	38.51	92.82	2.88	145.265
1x10^{15} cm^{-2}	2.243	19.78	38.63	89.36	0.95	138.83
1x10^{14} cm^{-2} annealed	2.128	11.69	35.42	80.87	3.46	125.595
5x10^{14} cm^{-2} annealed	1.759	15	35.8	75.62	0.1	119.02
1x10^{15} cm^{-2} annealed	1.557	14.48	35.4	81.55	2.61	126.8

ble that extended annealing could further align the properties of the implanted sample with those of the annealed non-implanted film. For the top layer, annealing increases the refractive index for both samples. However, the extinction coefficient behaves differently; it decreases after annealing in the implanted sample, which contradicts the absorption measurements obtained through spectrophotometry. This discrepancy could be due to several factors: the model may require refinement, the current results are based only on data measured at a 70° incident angle, and additional angles might yield more accurate results. Additionally, spectroscopic ellipsometry measures a small spot of approximately 2 mm in diameter, whereas spectrophotometry covers a larger area with a spot size greater than 4 mm, so essentially a different part of the sample is measured.

4.3.4 Surface homogeneity and chemical states

The ellipsometer used in this work is equipped with focusing probes that reduce the light spot size of around 100 µm. Map measurements were performed with J.A. Woollam M-2000 ellipsometer using focusing probes at angle of 70° for 11x11 data points with a step and margin of 0.5 mm. From these measurements a pseudo refractive index parameter was calculated which is defined in Equation 4.10.

$$\langle\widetilde{n}\rangle^2 = (\langle n\rangle + i\,\langle k\rangle)^2 = sin\varphi^2\left[1 + tan\varphi^2\left(\frac{1-\rho}{1+\rho}\right)^2\right] \tag{4.10}$$

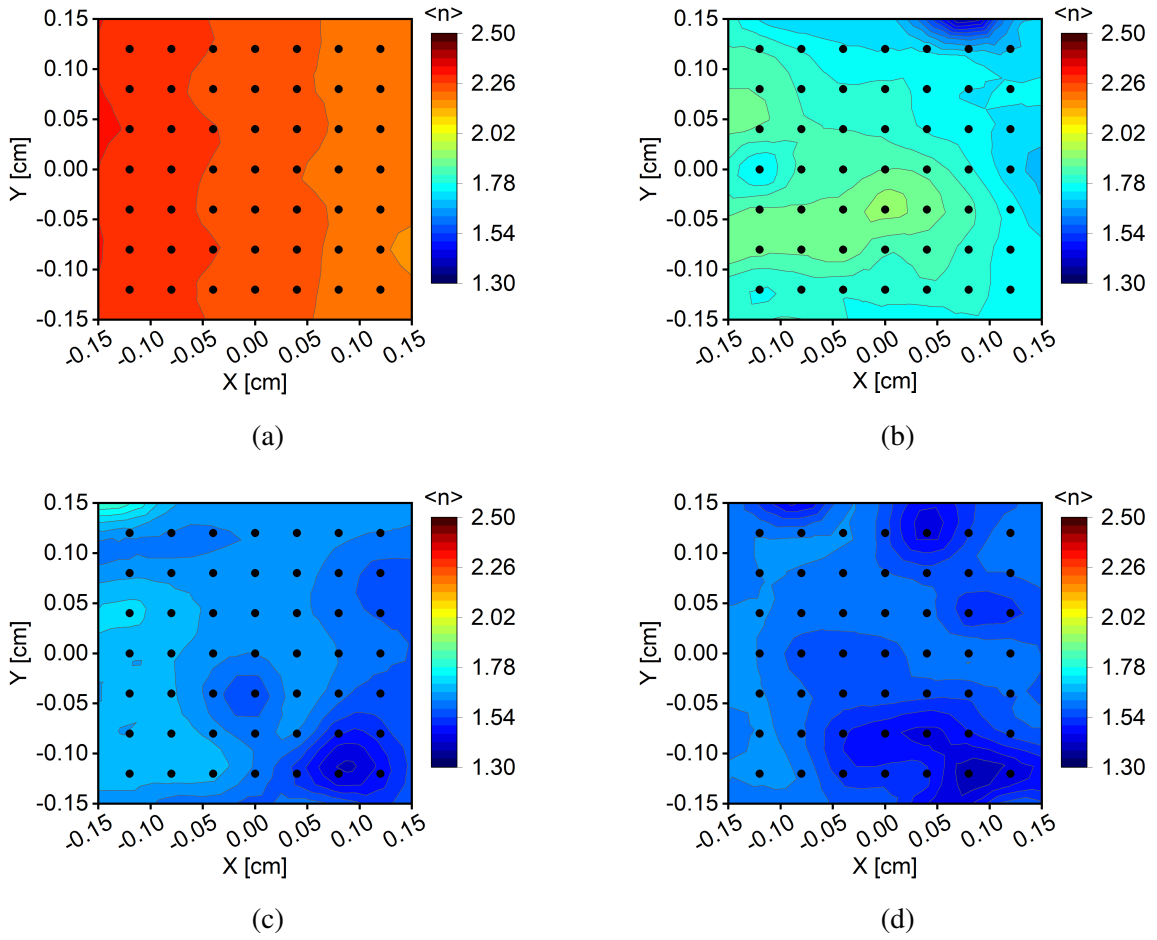

Figure 4.18. Pseudo refractive index maps of CuO samples before annealing (a) non-implanted CuO, implanted with 10 keV ions of dose (b) 1x10^{14} cm^{-2}, (c) 5x10^{14} cm^{-2}, (d) 1x10^{15} cm^{-2} [107].

where $\widetilde{n}$ is the complex refractive index, $\langle n \rangle$ is the pseudo refractive index, $\langle k \rangle$ is the pseudo extinction coefficient, φ is the angle of incidence, and ρ is defined as in Equation 4.8.

The $\langle n \rangle$ parameter allows for quick assessment of film uniformity through measurement and automatic calculation. For CuO, the non-implanted sample shows a clear slope of the parameter on the map (Figure 4.18a), due to the deposition process conducted without the rotation of the stage, which results in a layer with a gradient thickness. Implanted samples no longer have this characteristic but have some visible non-uniformities (Figures 4.18b-4.18d). Additionally, the value of the pseudo refractive index decreases with increasing implantation dose.

After the annealing, the slope is not visible anymore in case of non-implanted sample (Figure 4.19a) . Samples implanted with doses of 1x10^{14} cm^{-2} and 5x10^{14} cm^{-2} still show nonuniformieties after the annealing. The sample implanted with the highest dose has a plateau of high value of $\langle n \rangle$ and overall seems more homogeneous than before annealing.

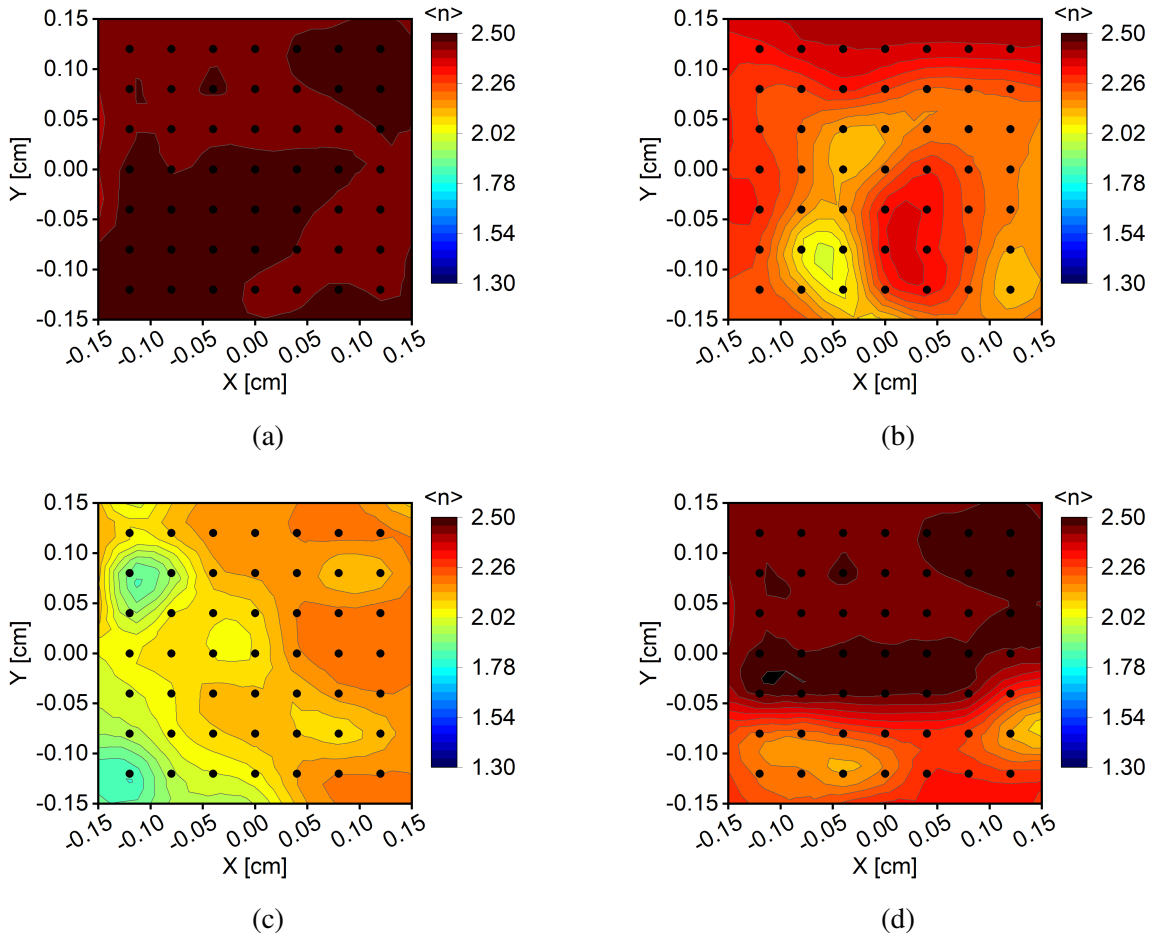

Figure 4.19. Pseudo refractive index maps of CuO samples after annealing (a) non-implanted CuO, implanted with 10 keV ions of dose (b) $1x^{14}$ cm^{-2}, (c) $5x10^{14}$ cm^{-2}, (d) $1x10^{15}$ cm^{-2}.

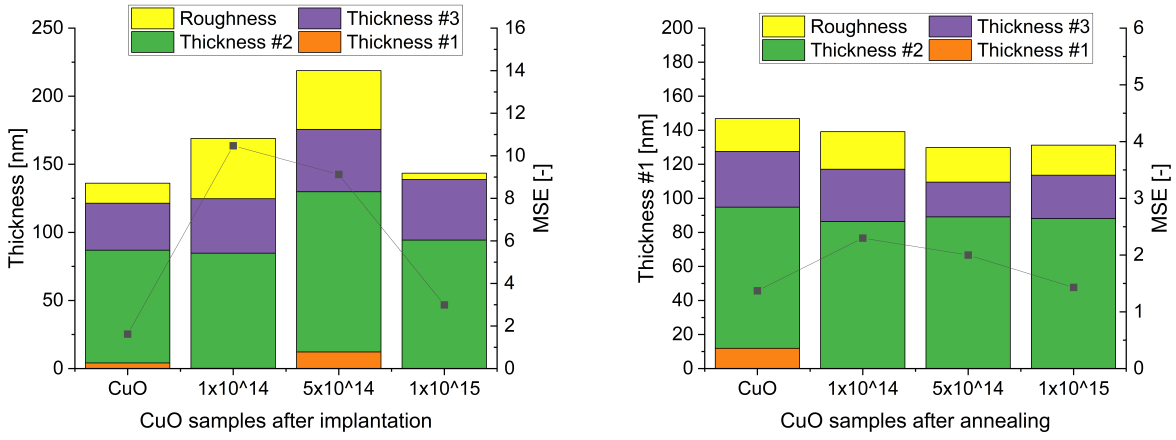

Figure 4.20. Maps fittings average results of CuO samples (a) before and (b) after annealing.

A different way of mapping is to see the result of fitting. Here, the CuO samples on glass were fitted with multilayered model, and the parameter presented on the maps is the total thickness. The average results of thickness of each layer and the mean square error (MSE) are presented in Figure 4.20. Fittings of samples after annealing show lower MSE and non-existent bottom layer. Three dimensional maps with a projection of total thickness calculated from the multilayer model are presented in Figure 4.21 and 4.22. The models used here consisted of glass substrate, three layers of CuO made with four Tauc-Lorentz oscillators and a roughness layer at the top. The fits were made as a continuous calculation for a whole map. The total thickness of all samples is lower after the annealing process. Regarding assessment of surface homogeneity, the pseudo-refractive index is a more dependable parameter as there is no uncertainty introduced with fitting process.

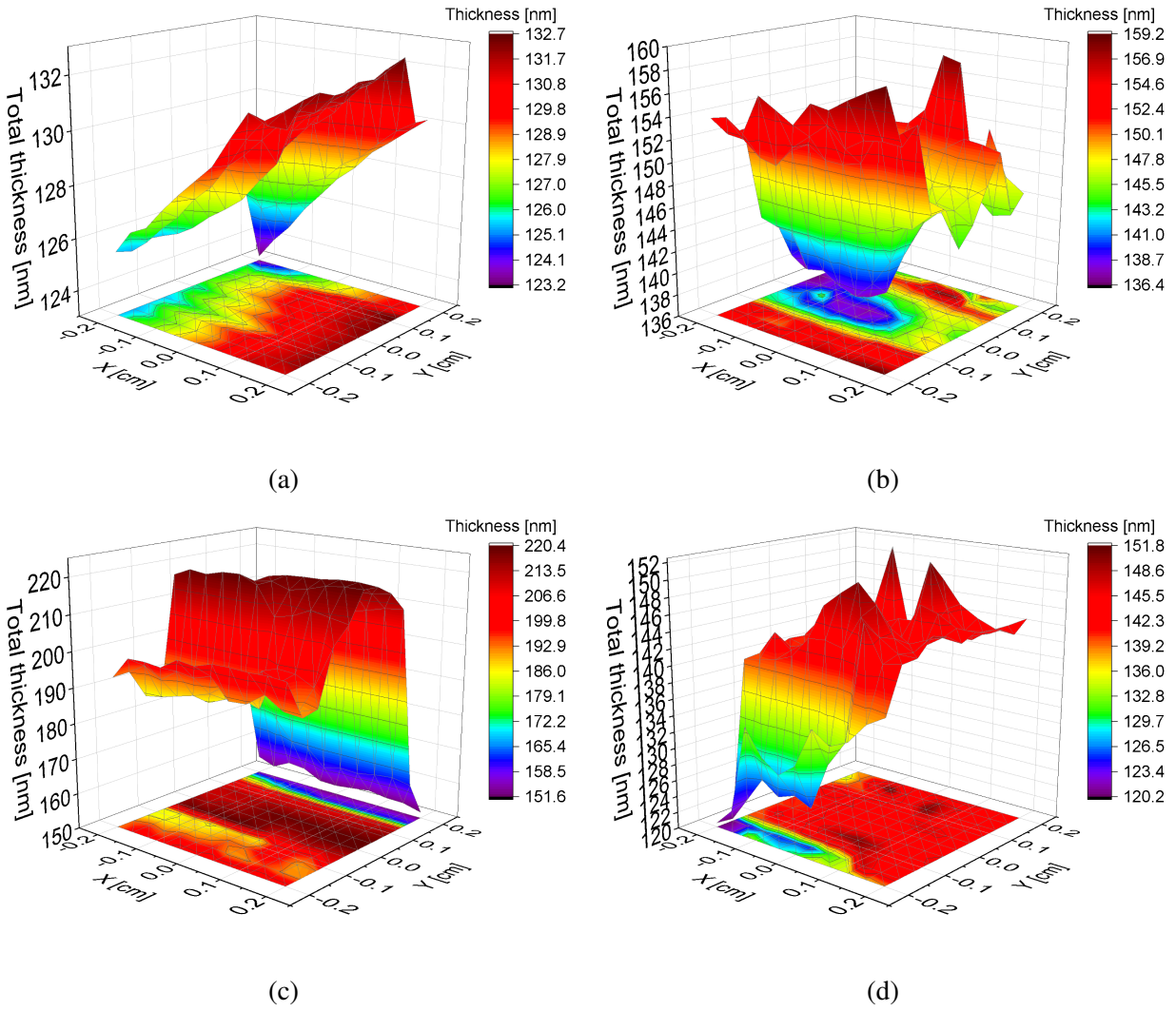

Figure 4.21. Total thickness three dimensional maps of CuO samples before annealing (a) non-implanted CuO, implanted with 10 keV ions of dose (b) 1x10^{14} cm^{-2}, (c) 5x10^{14} cm^{-2}, (d) 1x10^{15} cm^{-2}.

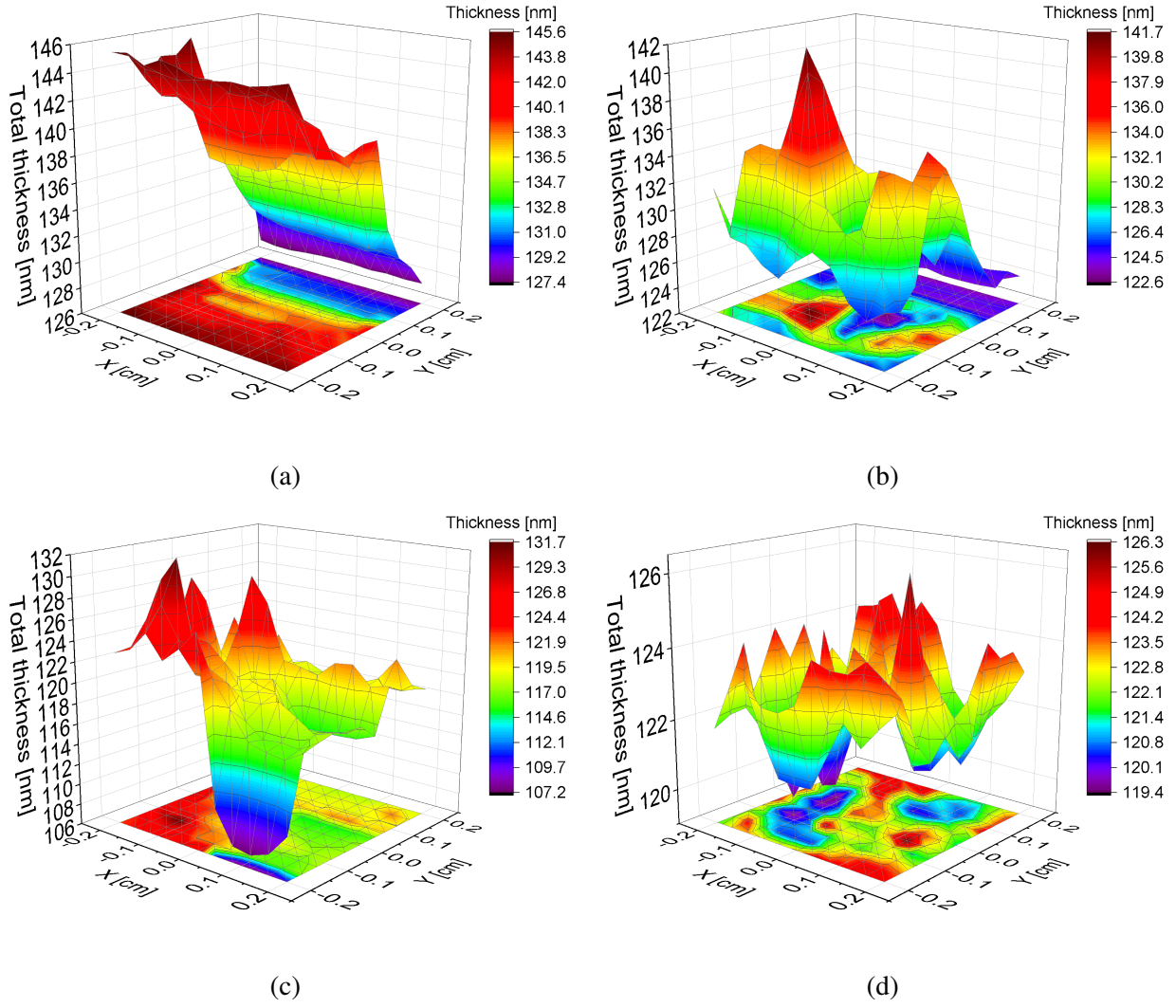

Figure 4.22. Total thickness three dimensional maps of CuO samples before annealing (a) non-implanted CuO, implanted with 10 keV ions of dose (b) 1x10^{14} cm^{-2}, (c) 5x10^{14} cm^{-2}, (d) 1x10^{15} cm^{-2}.

Atomic force microscopy (AFM) is a versatile technique capable of imaging nearly any surface. It is employed to measure and pinpoint various forces, such as adhesion strength, magnetic forces, and mechanical properties. The process involves using a sharp tip, approximately 10–20 nm in diameter, attached to a cantilever. The tip reacts to interactions with the surface, and its movements are detected by directing a laser beam onto the tip, which is then monitored by a photodiode [108]. Here, AFM was used to characterise roughness of CuO thin films before and after implantation. The apparatus used was atomic force microscope Dimension ICON from Bruker in tapping mode.

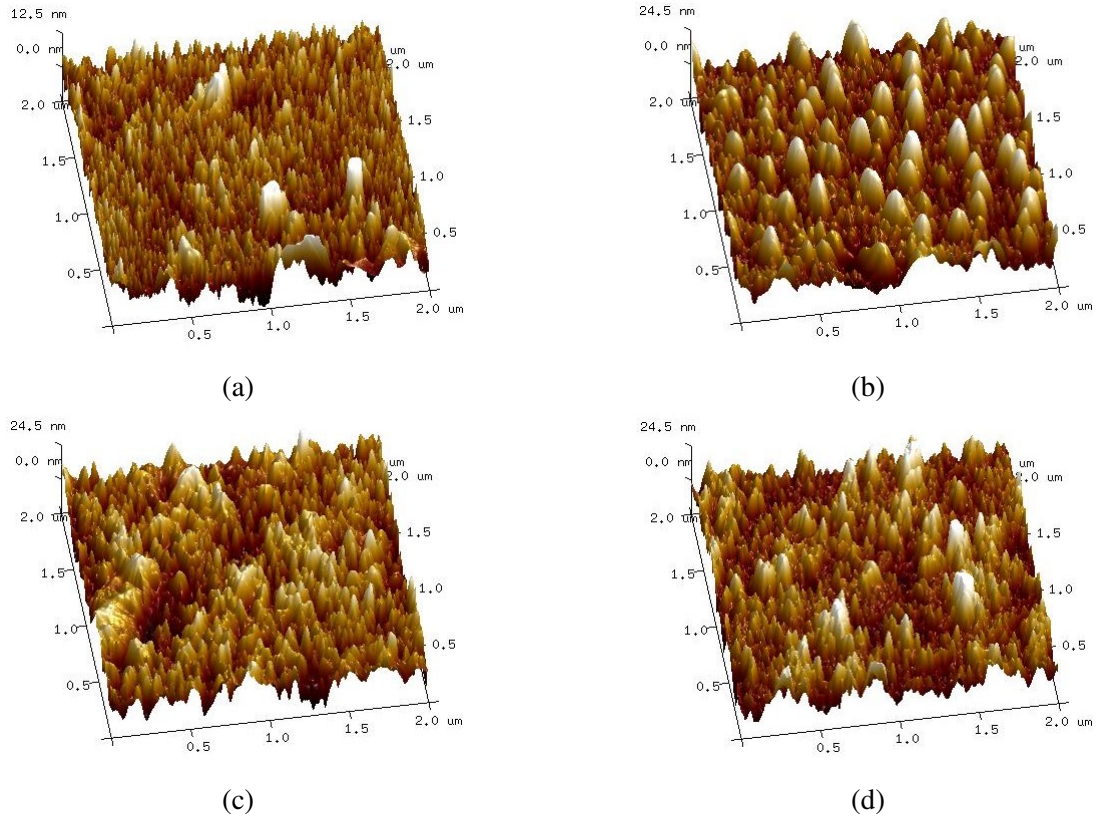

(a) (b)

(c) (d)

Figure 4.23. Atomic force microscopy 3D surface micrographs of CuO samples (a) non-implanted, implanted with 10 keV Cr ions of doses (b) 1x10^{14} cm^{-2}, (c) 5x10^{15} cm^{-2} and (d) 1x10^{15} cm^{-2} [109].

The roughness of the samples was evaluated using two parameters: R_a (arithmetical mean deviation of the assessed profile) and R_{max} (maximum valley depth below the mean line). Non-implanted samples exhibited the lowest roughness, with R_a at 2.36 nm and R_{max} at 39.7 nm. In contrast, the roughness values for implanted samples were notably higher: R_a = 5.17 nm, R_{max} = 49.4 nm for dose 1; R_a = 5.79 nm, R_{max} = 54.9 nm for dose 2; and R_a = 5.16 nm, R_{max} = 57.1 nm for dose 3. The surface of the S2-Si-130-dose1-10 sample stands out compared to the others, showing distinct regular curved formations (Figure 4.23). AFM results show that implantation increases the roughness of CuO thin films.

X-ray Photoelectron Spectroscopy measurements were performed at National Instutute of Materials Physiscs in Magurele, Romania. In XPS method, the sample is irradiated with soft x-rays, of energies lower than around 6 keV. The photons with sufficient energy excite core level electrons from the material. This process is summed by a simple Equation 4.11:

$$h\nu = BE + KE + \Phi \tag{4.11}$$

where $h\nu$ is photon energy, *BE* is binding energy, *KE* is kinetic energy of photoelectron, Φ is work function of spectrometer. The binding energy can be regarded as the difference of initial and final energy of electron in the process of emission from its orbital [110]. The kinetic energy of the emitted photoelectrons is measured by the detector, but the *BE* is a parameter that does not depend on the radiation used in the experiment. Therefore, to present XPS data the *KE* is recalculated to *BE* using Equation 4.11, and in the figures, x-axis is always from higher to lower *BE* values. Photoelectron peaks are labelled according to the element and the orbital from which the electrons were emitted. For instance, "O 1s" refers to electrons ejected from the 1s orbital of an oxygen atom. After emission of electron a "hole" is created in the material and this state is relaxed by filling the hole with an electron from a valence orbital. Then two phenomenon can happen: emission of excessive energy as photon - this is called X-ray fluorescence, or the Auger process can happen. In XPS the X-ray fluorescence is not detected, but Auger electrons are, and they contribute useful qualitative information [111].

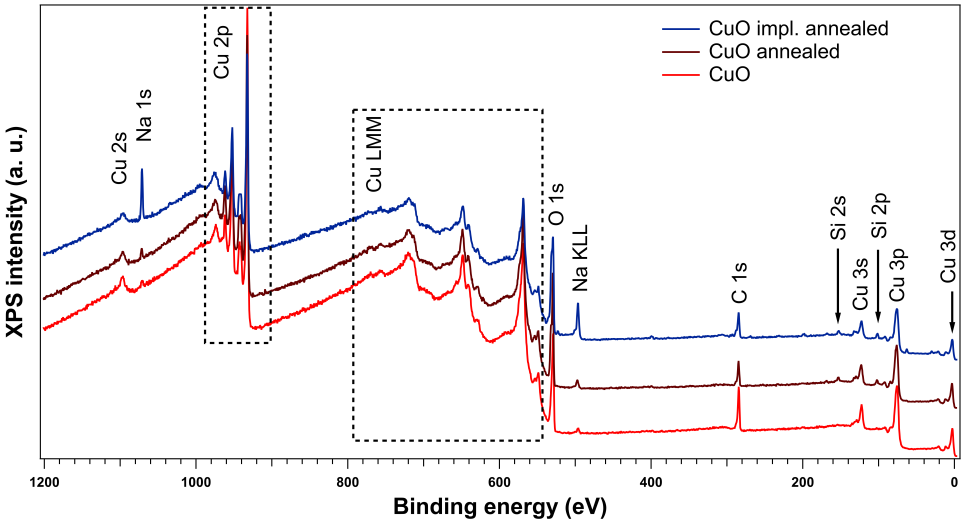

Figure 4.24. XPS wide scans of CuO as deposited, annealed, and implanted with 10 keV energy ions of dose 1x10^{15} cm^{-2} and annealed.

The investigation of chemical properties of the surface was done with XPS technique using an analysis chamber equipped with a 150 mm hemispherical electron energy analyser (Phoibos). The analyser operated in fixed transmission mode (FAT) with pass energy of 20 eV. The X-ray source

was monochromatic Al Kα of 1486.6 eV energy, at power of 250 W (12.5 kV × 20 mA). The charging effects were compensated with a flood gun (1V × 0.1 mA) and with binding energy correction with regard to the C 1s contamination core level at 286.4 eV *BE*. All data analysis and fitting were done with Igor Pro software. Peaks were fitted using Voigt function (sum of Lorentz and Gauss functions) [112]. All contributions coming from the same element had the same broadening, both Lorentzian and Gaussian, in case of Cu 2p the 1/2 and 3/2 peaks had different Lorenztain broadenings. The background used for Cu 2p spectra was Total Sum, and for O 1s Shirley background was applied.

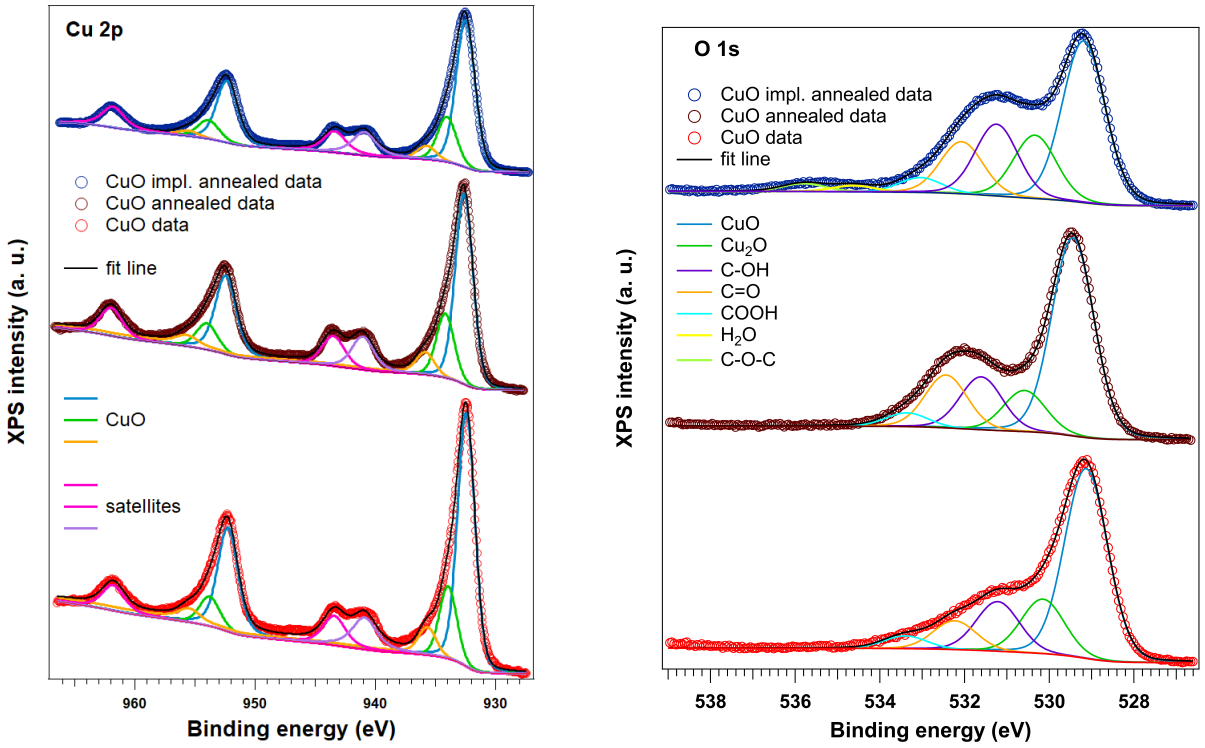

(a) (b)

Figure 4.25. XPS narrow spectra of (a) Cu 2p and (b) O 1s signals for samples, from bottom to top: CuO as deposited, CuO annealed, CuO implanted and annealed.

XPS extracts the signal only from the surface of the sample. Only electrons that escape the surface without undergoing inelastic collisions contribute to the characteristic photoelectron peaks used in XPS analysis. The attenuation length is a parameter akin to the inelastic mean free path of electrons, which is the average distance an electron with a specific kinetic energy can travel before experiencing inelastic scattering. However, the attenuation length also accounts for the effects of elastic scattering. For energies used in XPS the useful information is usually obtained from up to 10 nm deep in the material. For quantitative analysis there are methods that use atomic sensitivity factors, which are empirically derived factors from known compounds measurement that provide normalisation of peak intensity to determine atomic concentration. The XPS measurements give

information what changed on CuO thin films surface after implantation and/or annealing. XPS was also used to perform in depth characterisation of atomic composition.

Figure 4.24 shows wide scans of CuO samples, namely sample as deposited, after annealing, after implantation (energy 10 keV, dose 1x10^{15} cm^{-2}) and annealing. Wide scans are performed to see what elements are present in the sample. Next, specific ranges are measured to study desired elements. In studied samples clearly copper signals are present, both from photoelectron and Auger peaks. There is some Na and Si detected that probably come from the substrate or are a contamination. The Na signal is much stronger for implanted sample.

Table 4.7. The relative contribution of components for O 1s signal for CuO as deposited, after annealing and after implantation and annealing.

	Relative contribution in O 1s [%]						
Sample	CuO	Cu_2O	C-OH	C=O	COOH	C-O-C	H_2O
CuO	61.91	17.77	16.17	4.15	-	-	-
CuO annealed	55.23	11.47	14.73	14.74	3.83	-	-
CuO impl. annealed	42.83	16.71	18.94	13.8	3.94	1.64	2.14

The Cu 2p spectra all show typical signal of Cu^{2+} with around 19 eV spin orbit splitting and shake up satellites present around 9 eV from the Cu $2p_{3/2}$ peak (Figure 4.25a) [113]. The most intensive peak comes from CuO lattice and the two smaller from the surface and defects. The as deposited sample has the highest contribution of the lattice component. The O 1s spectra are dominated by strong peak around 529 eV which corresponds to CuO, at around 530 eV is typically the signal from Cu_2O [110]. The relative contribution percentage of O 1s components is presented in Table 4.7. The contributions that come from various organic adsorbates are stronger in case of annealed sample, and even stronger for implanted sample with additional peaks present around 536 eV. Both annealing and implantation combined with annealing introduce more defects and adsorbates into CuO surface.

4.3.5 Electrical properties

To investigate the electrical properties of CuO thin films, sheet resistance was measured using the four-point probe method with a Jandel RM3000+ Test Unit. This technique is applicable only to films deposited on dielectric substrates, such as the glass substrates used in this study. For each sample, the measurement was conducted ten times to ensure accuracy. The Jandel meter automatically selected the appropriate current for measurement, which in this case was set to 100 nA. The measurement results are summarised in Table 4.8.

Samples implanted with higher doses exhibited resistance levels too high for accurate measurement. However, after annealing, all samples became sufficiently conductive for measurement.

Table 4.8. Sheet resistance of CuO thin film samples.

Sample	Sheet resistance [Ω/□]
CuO	8.2 x 10^5 ± 5.3 x 10^2
CuO annealed	1.7 x 10^6 ± 3.6 x 10^2
1x10^{14} cm^{-2}	8.0 x 10^6 ± 2.0 x 10^3
5x10^{14} cm^{-2}	NA
1x10^{15} cm^{-2}	NA
1x10^{14} cm^{-2} annealed	1.1 x 10^6 ± 6.5 x 10^2
5x10^{14} cm^{-2} annealed	2.2 x 10^6 ± 71.2 x 10^3
1x10^{15} cm^{-2} annealed	6.3 x 10^6 ± 7.7 x 10^3

Notably, an improvement in electrical conductivity was observed in the sample implanted with 10 keV ions at a dose of 1x10^{14} cm^{-2}. In contrast, other implanted samples showed higher resistance compared to the non-implanted, annealed CuO thin film.

4.3.6 Depth profiling

Implanted CuO films were studied with Secondary Neutral Mass Spectrometry (SNMS) and XPS to determine a depth profile of elemental concentration.

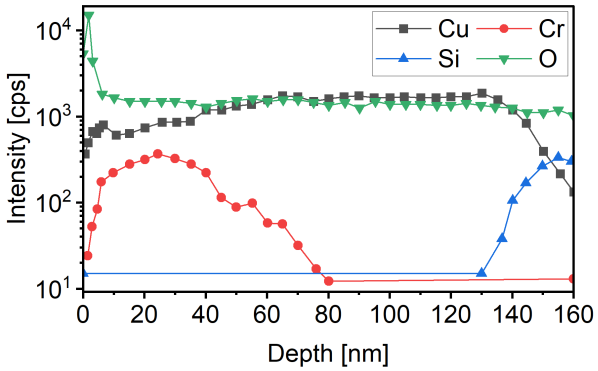

Figure 4.26. SNMS depth distribution of elements in CuO implanted sample[114]

The used SNMS/SIMS-XPS assembly contains a secondary neutral mass spectrometer, a secondary ion mass spectrometer and an X-ray photoelectron spectrometer (XPS) with a common vacuum system. The mass spectrometer is Balzers QMG 422. The device is at ATOMKI Institute for Nuclear Research, Hungarian Academy of Sciences in Debrecen. The sensitivity of this measurement is 1 ppm, and depth resolution 1-2 nm. The sample characterised with this method was 130nm CuO deposited at Si and implanted with 15 keV Cr ions of dose 5x10^{16} cm^{-2}. The resulting profile is presented in Figure 4.26. Near the surface of the sample there is excess O and almost no

Cr. Cr shows a peak of distribution at around 20 nm in depth. This observation is corresponding well to SRIM simulations, but the peak position is around two times deeper than predicted with simulations.

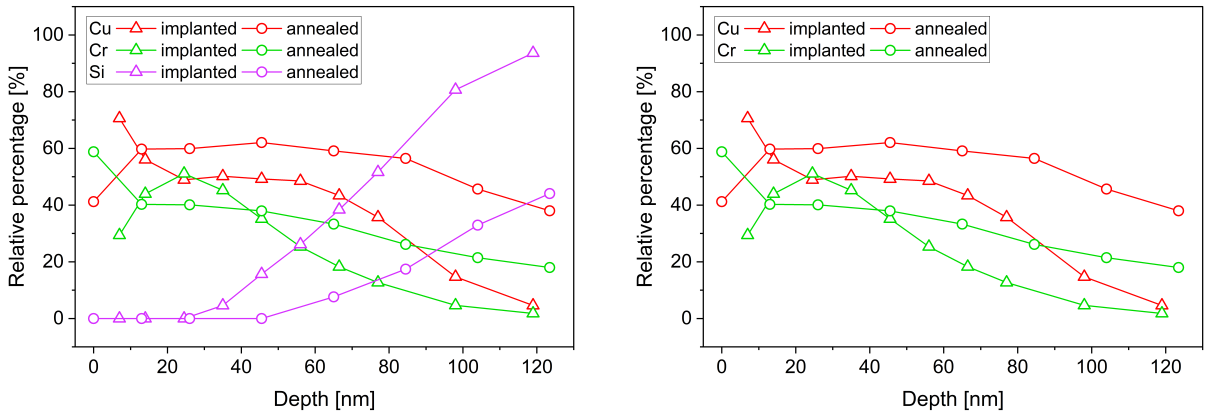

(a) (b)

Figure 4.27. Relative atomic concentration determined from XPS depth measurements of implanted sample and implanted annealed sample of (a) Cu, Cr and Si, (b) only Cu and Cr.

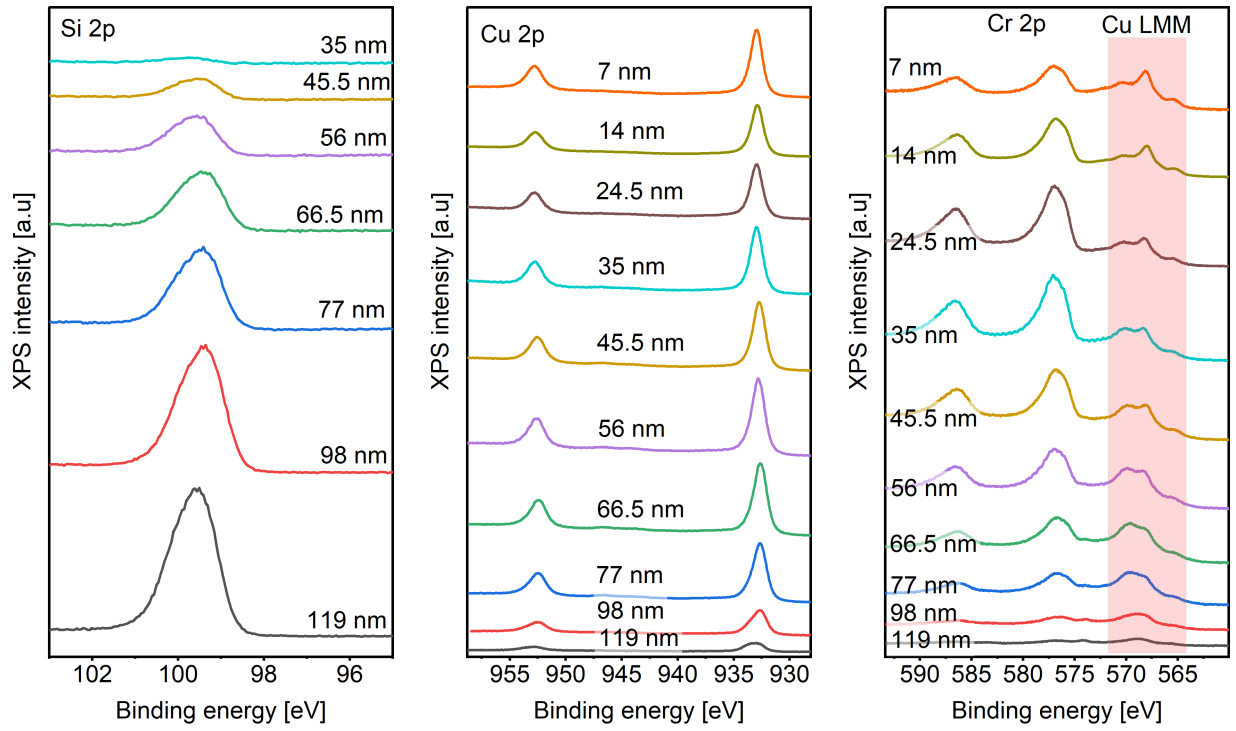

(a) (b) (c)

Figure 4.28. Depth measurements of implanted CuO for signals of (a) Si 2p, (b) Cu 2p, (c) Cr 2p.

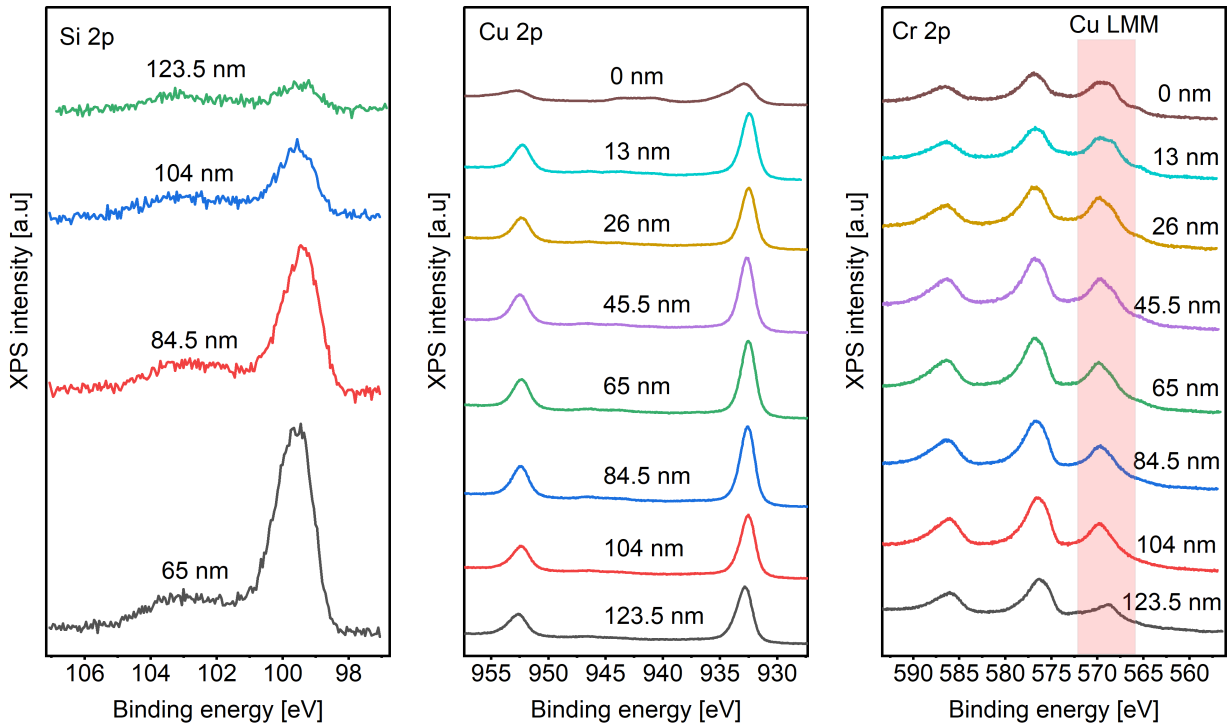

(a) (b) (c)

Figure 4.29. Depth measurements of implanted and annealed CuO for signals of (a) Si 2p, (b) Cu 2p, (c) Cr 2p.

The depth profiling analysis with XPS was performed by Ar+ sputtering the sample in cycles (at 3keV x 10 mA with $1*10^{-5}$ mbar Ar+ pressure) followed by XPS measurements. The depth measurements were performed for CuO deposited on silicon with thickness of 55 nm (this is the thickness aimed during deposition process). Thin film was implanted with 15 keV energy Cr ions and dose of $5x10^{16}$ cm^{-2}. These samples were chosen as they were implanted with high dose and therefore were promising to detect Cr signal in them. Half of this sample was then annealed in air at 400 °C for 6 hours. These two samples, implanted and implanted and annealed, were due to XPS measurements in cycles after Ar sputtering. The resulting spectra are presented in Figures 4.28 and 4.29. The signal from Cr 2p is close to the Cu Auger LMM signal, which is marked on Figures 4.28c and 4.29c. Using this data and atomic sensitivity factors (determined for height of peaks [115]) the relative concentration of elements was calculated. The results are presented in Figure 4.27, where the scale of depth does not correspond to the thickness of the films. The depth of measurement was estimated using sputtering rate of the sample, that was determined during sputtering cycles. This calculation is not accurate, yet there is still a very valuable observation to be made. The distribution of Cr before annealing has a clear peak between 20 and 30 nm in depth. This correspond well to the SRIM simulations results, though there this peak position was around 10 nm. This discrepancy can be explained with the fact that simulation only considers a point beam

not taking into account the neighbouring beams influence (as was discussed regarding Figure 4.1). After implantation the Cr distribution is almost uniform in the whole sample. This is an expected result from annealing which accelerates diffusion of Cr in CuO. The annealing step distributes the dopant into the film, proving that implantation and annealing can be a successful doping technique for CuO thin films. If the film was thicker, it is probable that the ions would not distribute into the whole thickness of the films. Optimisation of implantation energy, temperature and time of annealing could result with successful doping of thicker samples or manufacturing a doped region within a film.

4.4 Cu_2O and Cu_4O_3

4.4.1 Structural properties

Cu_2O samples were implanted only with 10 keV Cr ions with three different doses. In all discussed results for this oxide the doses will be named as follows: dose 1 - 1x10^{14} cm^{-2}, dose 2 - 5x10^{14} cm^{-2}, dose 3 - 1x10^{15} cm^{-2}. XRD measurements for as deposited and implanted samples were performed with PANalytical X'Pert PRO diffractometer equipped with a Cu anode (0.154 nm radiation wavelength). The measurement step was 0.05°with time per step of 8000 s. The resulting diffractogram and phase analysis is presented in Figure 4.30. All samples exhibit three distinct peaks corresponding to Cu_2O (ICDD card #01-074-1230): (110), (111), and (200). In the non-implanted sample, a Cu peak is also observed, suggesting that some additional copper, not just the oxide, might have been deposited. However, the Cu_2O peaks remain distinct and clearly identifiable. The sample implanted with the highest dose shows a small peak around 28°, which is attributed to the substrate (ICDD card #00-003-0544) but could also originate from another copper oxide — Cu_4O_3 (ICDD card #00-049-1830). This latter finding indicates a possible phase change due to implantation, and damage done to the layer, allowing the substrate signal to become more pronounced. Additionally, a small Si peak (ICDD card #00-003-0544) is visible in the film implanted with a medium dose.

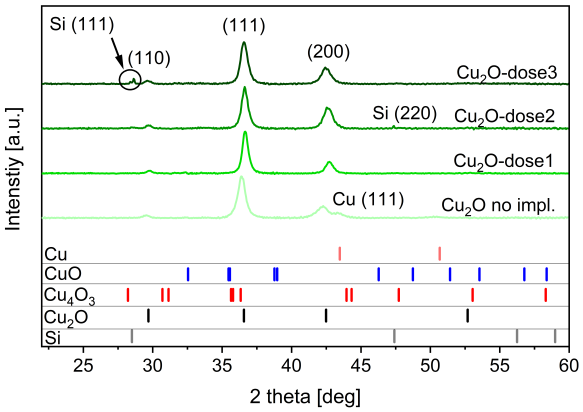

Figure 4.30. Diffractograms of Cu_2O samples non-implanted and implanted with three different doses.

Samples prepared in the same manner, but deposited on glass, substrates were annealed in Ar at 400°C for 6 hours. Ar was chosen as ambient gas for this process, as annealing with presence of oxygen would result with transformation of Cu_2O into CuO. Before the annealing process they were measured with Bruker D8 Advance Diffractometer in theta-theta grazing incidence angle configuration. Only the range that covers the two most important Cu_2O peaks was chosen for measurements. The sample were characterised in the same way after the annealing. Result-

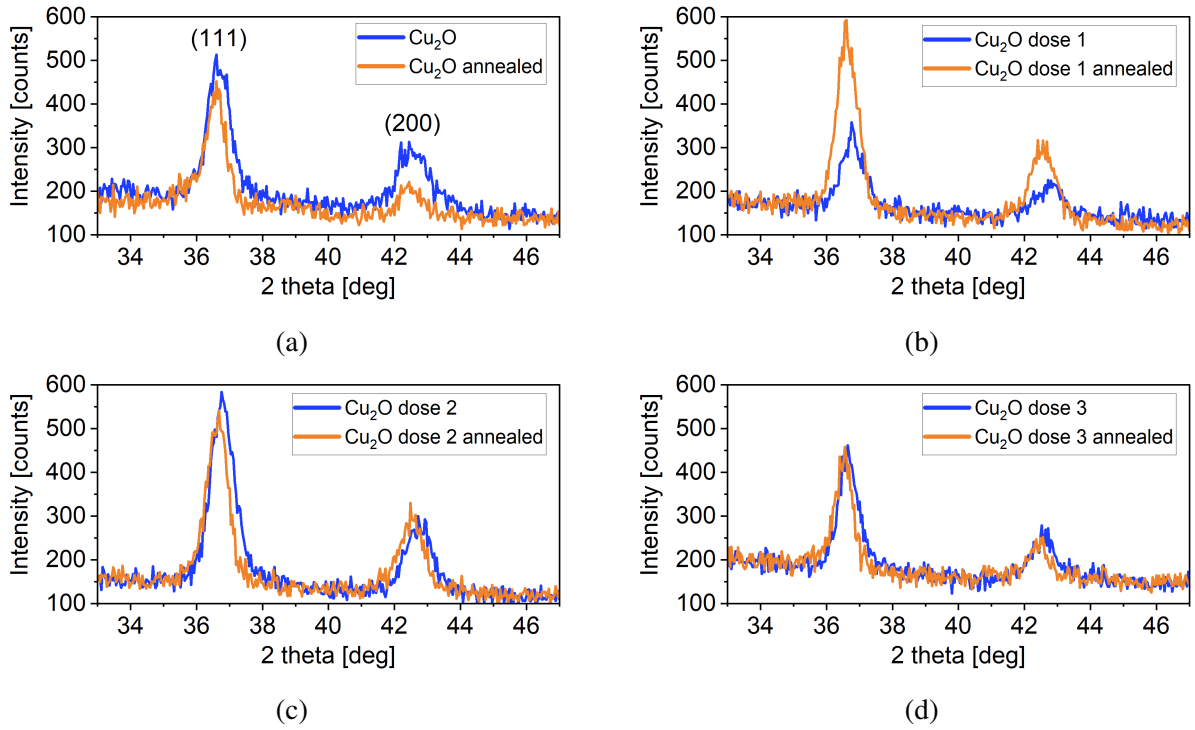

Figure 4.31. Diffractograms of Cu_2O samples before and after annealing in Ar (a) non-implanted sample, implanted with (b) dose 1, (c) dose 2, (d) dose 3.

ing diffractograms are showed in Figure 4.31. The annealing process caused a slight shift of the peaks toward lower angles for all samples. For samples implanted with doses 2 and 3, the change after annealing is negligible. In the case of the non-implanted sample, the intensity of the peaks decreased, but their width also reduced. The most significant difference is observed in the sample implanted with dose 1, where the peak intensity increased after annealing. It is difficult to draw definitive conclusions about the effect of annealing on the structural properties of the Cu_2O layers.

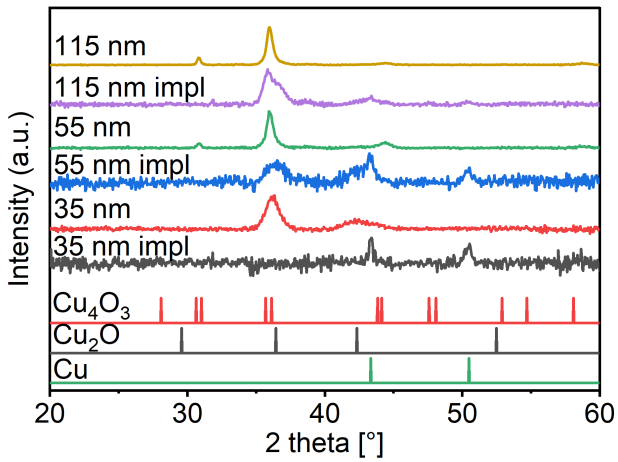

Figure 4.32. Diffractograms of various thickness Cu_4O_3 thin films before and after implantation with Cr ions.

Cu_4O_3 films were deposited only on silicon substrate. XRD measurements were performed again with PANalytical X'Pert PRO diffractometer as for CuO and Cu_2O samples. Results for various thickness films are shown in Figure 4.32. The thinnest Cu_4O_3 sample exhibits a peak from Cu_2O (ICDD card #01-074-1230), indicating incomplete deposition (Fig. 2b). In the thicker samples, 115 nm and 55 nm, the film consists solely of Cu_4O_3, with visible peaks at (200), (202), (404), and (220) (ICDD card #00-0491-830). After ion implantation, Cu peaks (ICDD card #00-001-1242) appear. For the 55 nm sample, the crystal structure is significantly degraded, making the paramelaconite peaks barely detectable. The thin film was damaged by the implantation process. The thinnest sample suffered the most damage, as the ions and recoils affected its entire thickness, with simulations indicating a recoil range of approximately 30 nm. The 55 nm sample is also heavily damaged, with the recoils penetrating deeper into the material, impacting most of the sample.

To estimate the thickness of samples X-ray reflectivity measurements were done using PANalytical X'Pert PRO diffractometer. The resulting curves of chosen samples are presented in Figure 4.33. The measurement parameters were: the angular range 0.2–3.0°, step 0.003°, and time per step 10 s. For Cu_2O there is a drop in intensity visible for implanted sample. this suggest that there are differences within the film, and a layer closer to the surface has different properties than the layer beneath. Critical angle and the slope are similar for both samples. The calculated thickness were 133 nm for non-implanted and 127 nm for implanted sample. In case of Cu_4O_3 each sample exhibits increase of slope and decrease of critical angle which correspond to increase in roughness and decrease of film density. Only for non-implanted samples it was possible to determine the thickness. For 35 nm sample it was 37 nm, for 55 nm sample - 73 nm, and for 115 nm sample - 129 nm.

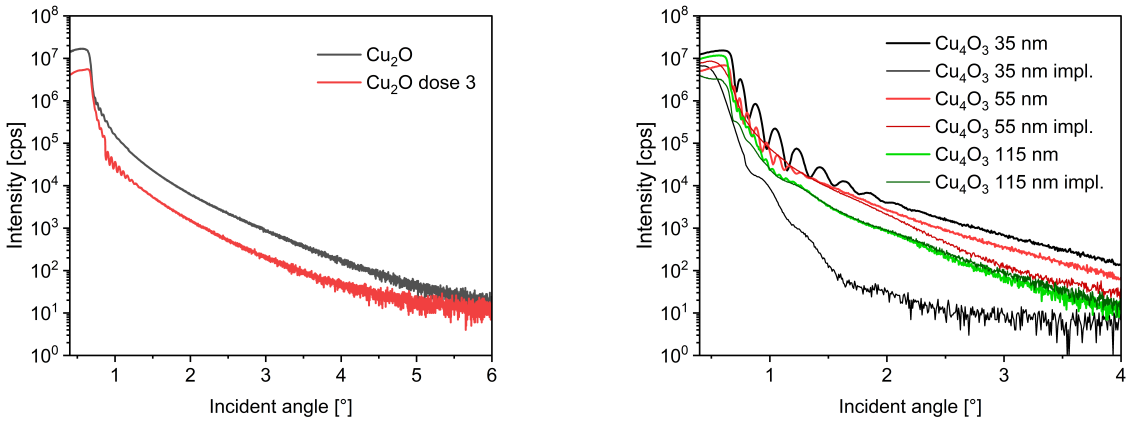

(a) (b)

Figure 4.33. X-ray reflectivity curves for (a) Cu_2O and (b) Cu_4O_3 samples.

4.4.2 Optical properties

The absorption of light of Cu_2O films was measured using spectrophotometry with an AvaLight-DH-S-BAL source and an AvaSpec-ULS-RS-TEC detector in the transmission mode. Before the absorbance measurement, a dark signal and the reference signal were collected, where the reference was a glass slab.

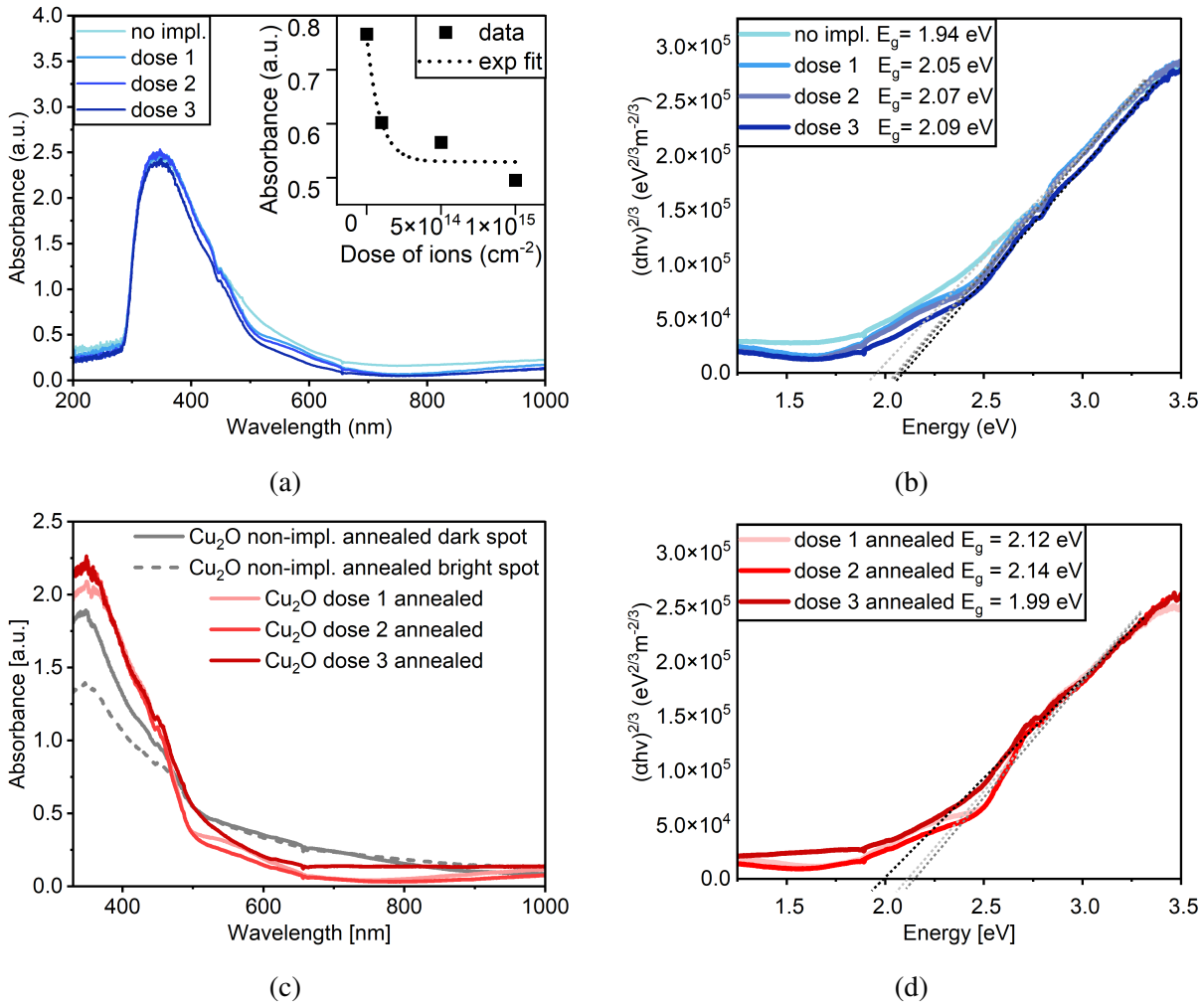

Figure 4.34. Optical properties of Cu_2O thin films implanted with Cr ions of different dose and energy: (a) absorbance of Cu_2O films after Cr ion implantation; (b) Tauc plot for Cu_2O films implanted with 10 keV Cr ions, and after annealing (c) absorbance of implanted films and two spots of non-implanted sample, (d) Tauc plot for implanted and annealed samples.

Implantation decreases the absorption of light by Cu_2O films as shown in Figure 4.34a. The inset in this figure shows that this decrease of absorption is approximately exponential regarding the dose of ions. After annealing absorbance of implanted films has more profound drop at 500 nm wavelength especially in case of dose 1 and dose 2 implanted samples. The non-implanted sample after annealing deteriorated, there was visibly a darker part of the sample and a brighter one, and

both of them had lower absorption of light than implanted samples (Figure 4.34c). Therefore, in case of annealed samples Tauc plot was calculated only for implanted ones. The Tauc plot for Cu_2O was prepared as for direct forbidden transition [39]. The plots for samples before annealing are presented in Figure 4.34b and after annealing in Figure 4.34d. The results show that a higher band gap corresponds to a higher dose of implanted ions. Annealing results with even higher band gap values, though dose 3 sample was an exception as it had lower band gap after implantation. It is visible in absorbance spectrum (Figure 4.34c) that the drop around 500 nm is less intense for dose 3 sample than for dose 1 and dose 2 samples, and this range of absorption influences strongly the determined value of band gap.

Spectroscopic ellipsometry was used to characterise both Cu_2O and Cu_4O_3 samples. Measurements of Cu_4O_3 films were performed with J.A. Woollam M-2000 ellipsometer. The Cu_2O films deposited on glass were measured with VASE (variable angle spectroscopic ellipsometer), also from J.A. Woollam company.

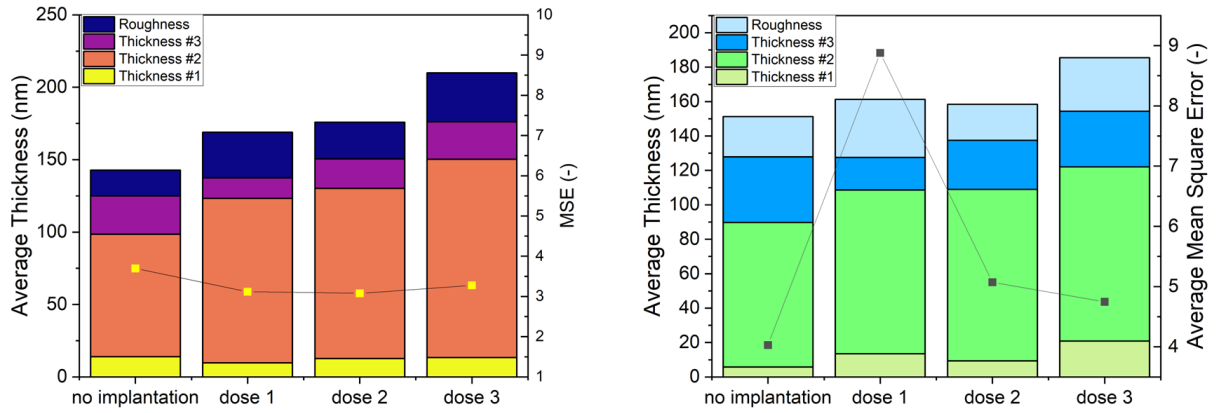

(a) (b)

Figure 4.35. Fit results of SE data for Cu_2O samples deposited at silicon (a) for representative points and (b) for the whole maps [109]. The data points connected with solid line represent the mean square error (MSE) values.

Cu_2O films deposited on silicon were studied with map measurements of 11 point maps with step and margin of 0.5 mm. For these samples a multi-layered model was established. After the first B-spline fitting of the non-implanted sample, a model for Cu_2O was created based on four Tauc–Lorentz oscillators (Equation 4.3.3) as this oxide has four energy transitions [39]. The model consisted of five layers: substrate — Si, the interface layer between substrate and film (layer #1), the main layer of the film (layer #2), the top layer (layer #3), and the roughness layer (which is 50% void and 50% top layer). From the maps representative points for each sample were arbitrarily chosen. The results of fitting for these point as well as average results for the whole maps are presented in Figure 4.35.

The total thickness of the sample is calculated by summing the thicknesses of layer #1, layer #2, layer #3, and half of the roughness layer. The results of the total thickness for maps of all four samples are shown in Figure 4.37. Each sample exhibits certain points that deviate significantly from the majority of the layer, such as near the X 0.2 cm, Y 0.2 cm corner for the non-implanted sample. The non-implanted sample exhibits a uniform map with exception of few points at the edge. The implanted samples show much more nonuniform maps of total thickness. The mean squared error (MSE) values for the map fits were reasonable, with values under 10, which is considered good for a map fitting.

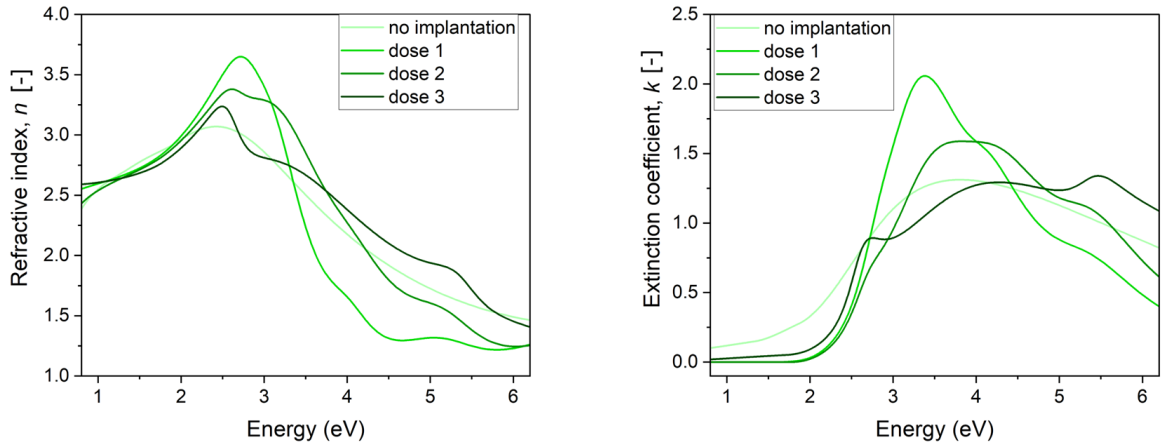

(a) (b)

Figure 4.36. (a) Refractive index and (b) extinction coefficient calculated from model fitting at representative points of Cu2O samples, the data is for main layer #2 [116].

Representative points from all Cu_2O samples were modelled to determine the oxide's optical properties. The refractive index n and extinction coefficient k derived from the fitted model are shown in Figure 4.36. The non-implanted sample exhibits the smoothest energy dependence for these parameters. In contrast, the implanted samples display additional maxima, with the number and position of these peaks varying according to the implantation dose. The optical parameters n and k exhibit varying energy dependence based on the implantation dose. The model used four Tauc–Lorentz oscillators with energies around E_1 = 2.5 eV, E_2 = 3 eV, E_3 = 4 eV, and E_4 = 5.5 eV. Fitting of data showed that these energies shifted after implantation. With higher implantation doses, the amplitude of E_2 and E_3 initially increases, followed by a decrease in E_2 and an increase in E_4. The amplitudes of E_1 and E_4 rise while the others diminish the higher the implantation dose. These oscillators correspond to specific transitions occurring at the indicated energies. As suggested by Ito et al., transitions could be observed at energies of 2.624 eV, 2.755 eV, 3.5 eV, and 4.3 eV, although these are lower than the values that resulted from fitting [117].

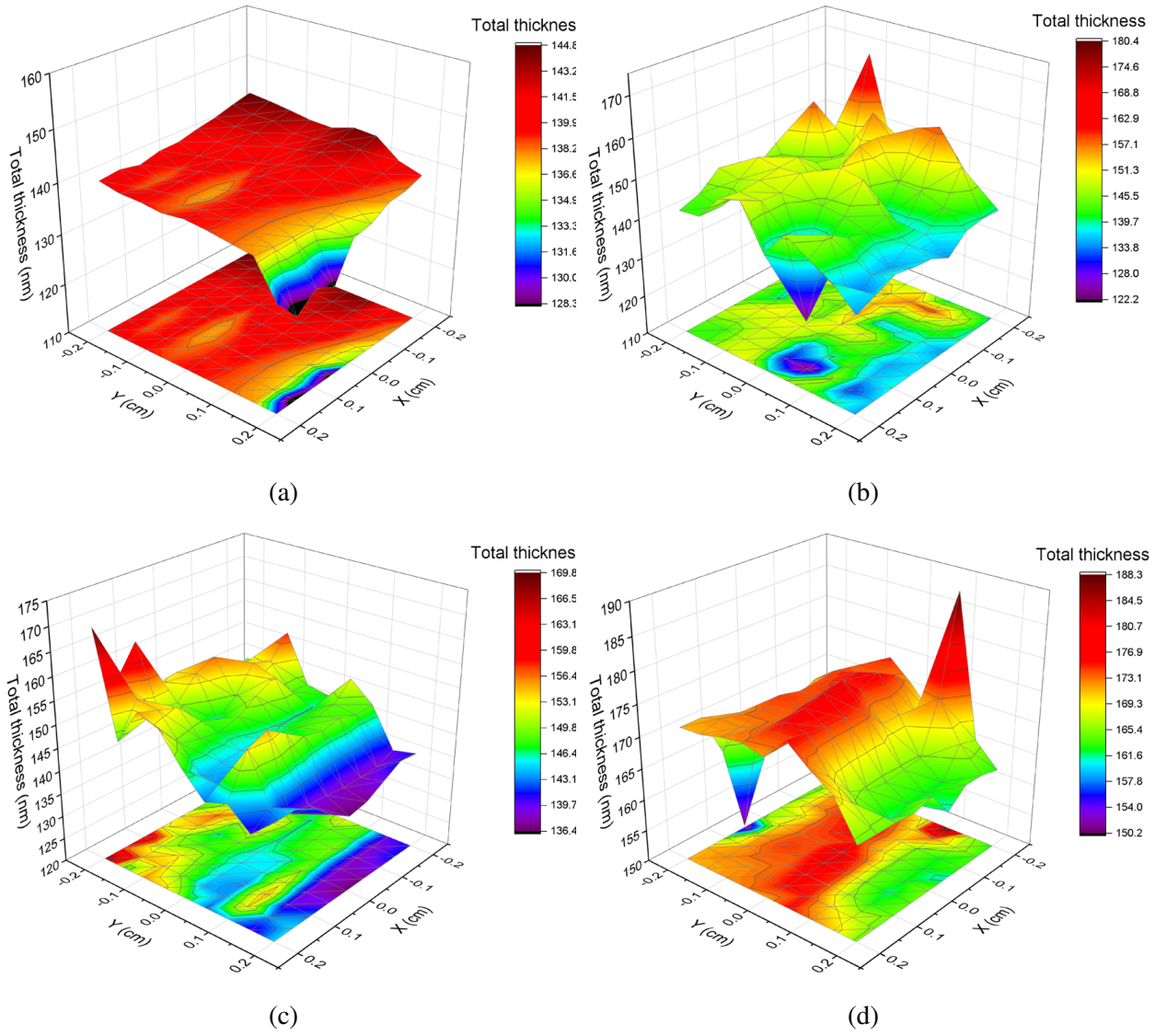

Figure 4.37. 3D maps of total thickness parameter calculated Cu_2O samples (a) non-implanted, (b) dose 1, (c) dose 2, and (d) dose 3 [116]

.

Ellipsometry results indicate that the overall thickness of the modelled samples increases with the ion implantation dose, even though all samples were deposited under identical conditions and for the same time duration of deposition process. Figure 4.35a reveals that the roughness layer and layer #3 become thicker with higher implantation doses, while the lower layers do not show this trend. The introduction of Cr contributes to the increased film thickness, particularly affecting the layers closest to the surface. This model analysis of map measurements is a way to study the homogeneity of films. In the next subsection Cu_2O samples are characterised using pseudo refractive index parameter and with AFM method to study their homogeneity.

Cu_2O samples after annealing were not fitted with multilayered models. It proved to be impossible to achieve good fits quality with previously used model. The reason for it is the used transparent

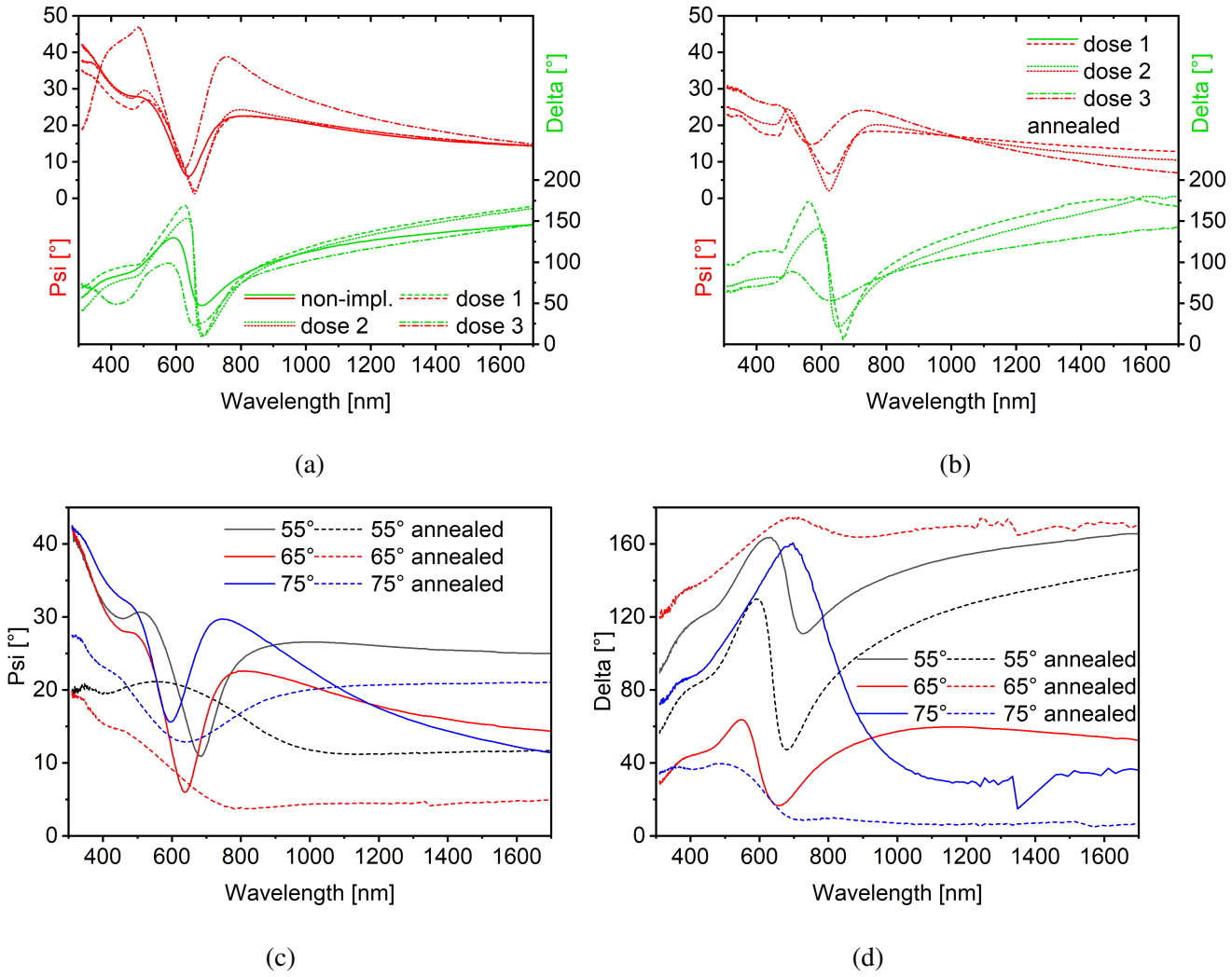

Figure 4.38. SE measurement data, Psi and Delta, for Cu_2O samples (a) before and (b) after annealing measured at 65°angle. (c) Psi and (d) Delta for non-implanted sample measured at various angles.

substrate, even though the backscattering of light was diminished by sticking an opaque tape to the rear side of the sample. Yet still ellipsometry delivers a way to study changes in the material - by examining the measured Psi and Delta values. Figure 4.38a shows the data for 65°incident angle for non-implanted and implanted Cu_2O samples. The higher the dose of implantation the more data differs from as deposited oxide. Data for implanted and annealed samples is presented in Figure 4.38b. The film implanted with the highest dose differs from the other two more, although this difference is smaller after annealing than before. The non-implanted sample data for various angles before and after annealing is showed separately in Figures 4.38c and 4.38d. It can be clearly seen that annealing caused more profound changes in ellipsometric result than the implantation. It was said before that the Cu_2O sample degraded after annealing, and ellipsometry measurement confirms that.

Table 4.9. Transition energies of Cu_4O_3 and fitted Tauc-Lorentz oscillators position energies [118].

Transition	Oscillators positions	
energies [eV]	non-implanted	implanted
1.80	0.52	0.38
2.34	1.96	1.92
3.08	2.87	2.70
3.53	3.37	3.26
3.90	3.80	3.71
5.29	3.84	3.75
5.68	5.69	6.00

For the two Cu_4O_3 sample analysis a ellipsometry model was prepared. It based on 7 Tauc Lorentz oscillators. The energies of transitions [39] in this oxide and fitted positions of oscillators in the main layer are listed in Table 4.9. The roughness and top layer #3 of the films were significantly affected by ion implantation. The combined thickness of these layers (using half of the roughness layer) increases with implantation, as the ions alter the material properties within the sample's depth. SRIM simulations indicate this depth to be approximately 30 nm, which aligns with the SE results showing that the combined thickness of roughness layer and layer #3 is about 30 nm for Cu_4O_3. The roughness layer is notably thicker in implanted sample compared to non-implanted one.

The optical properties of interest are those of the top layer (#3) and the main layer (#2). Figure 4.39 presents the absorption coefficient, refractive index, and extinction coefficient for the studied samples. Implantation reduces the material's absorption, particularly for energies above 3 eV. The optical parameters n and k also show lower values across most of the energy spectrum following implantation. An increase in Urbach energy is more pronounced in the main layer (Figure 4.39b). The top layer is predominantly responsible for light absorption, both before and after implantation. The n and k characteristics suggest that the top layer has more prominent oscillators in the fitted model, with these parameters also exhibiting higher values in the top layer than in the main layer. When compared to literature values, n and k are consistent, with n peaking around 2.5–3 and decreasing at energies above 3 eV, while k increases at higher energies. The extinction coefficient of the top layer decreases more significantly after implantation than that of the main layer, indicating that the implantation process has a more substantial impact on the sample's surface. The reduction in absorption is primarily due to a decrease in the amplitude of oscillators with energy positions around 3.5 eV.

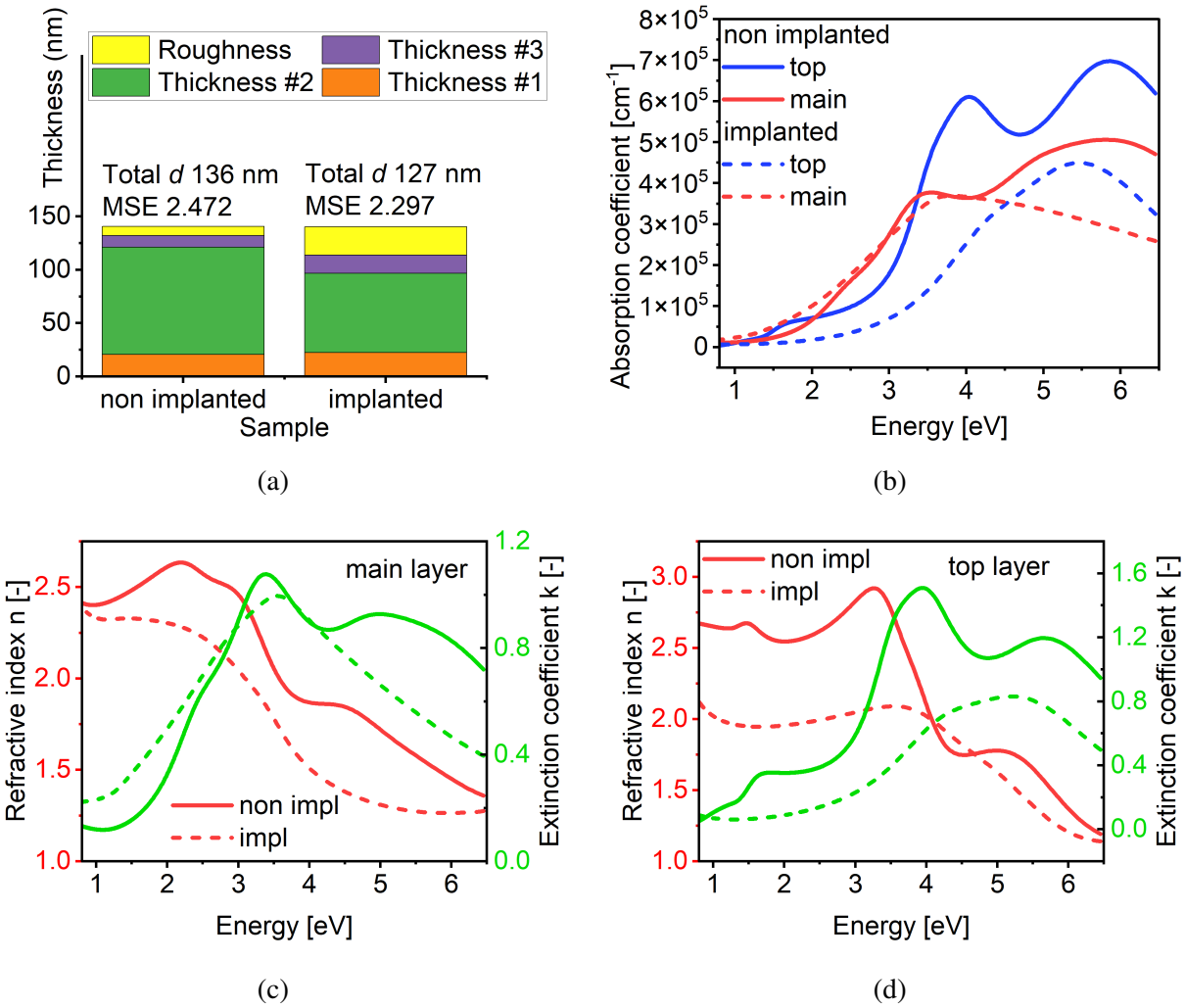

Figure 4.39. (a) Spectroscopic ellipsometry model fitting results for Cu_4O_3, and determined (b) absorption coefficient, refractive index and extinction coefficient for (c) main and (d) top layer of the model [118].

4.4.3 Surface homogeneity

From map measurements of Cu_2O samples also the pseudo refractive index <*n*> (Equation 4.10) was calculated for Cu_2O. For non-implanted Cu_2O the slope that is due to deposition without stage rotation is slightly visible. Samples implanted with dose 1 and dose 2 appear to be more homogeneous than non-implanted sample. Film implanted with highest dose shows clear nonuniformity (Figure 4.40d). The maps of total thickness and pseudo refractive coefficient are different, where the main reason is that pseudo refractive index is not a result of fitting but of a direct calculation. Total thickness parameter considers all measured spectrum, while pseudo refractive index is calculated only for a chosen light wavelength.

Map measurement and pseudo refractive index calculation was performed for Cu_4O_3 deposited on silicon. This oxide was implanted only with 15 keV energy Cr ions of $5x10^{16}$ cm^{-2} dose.

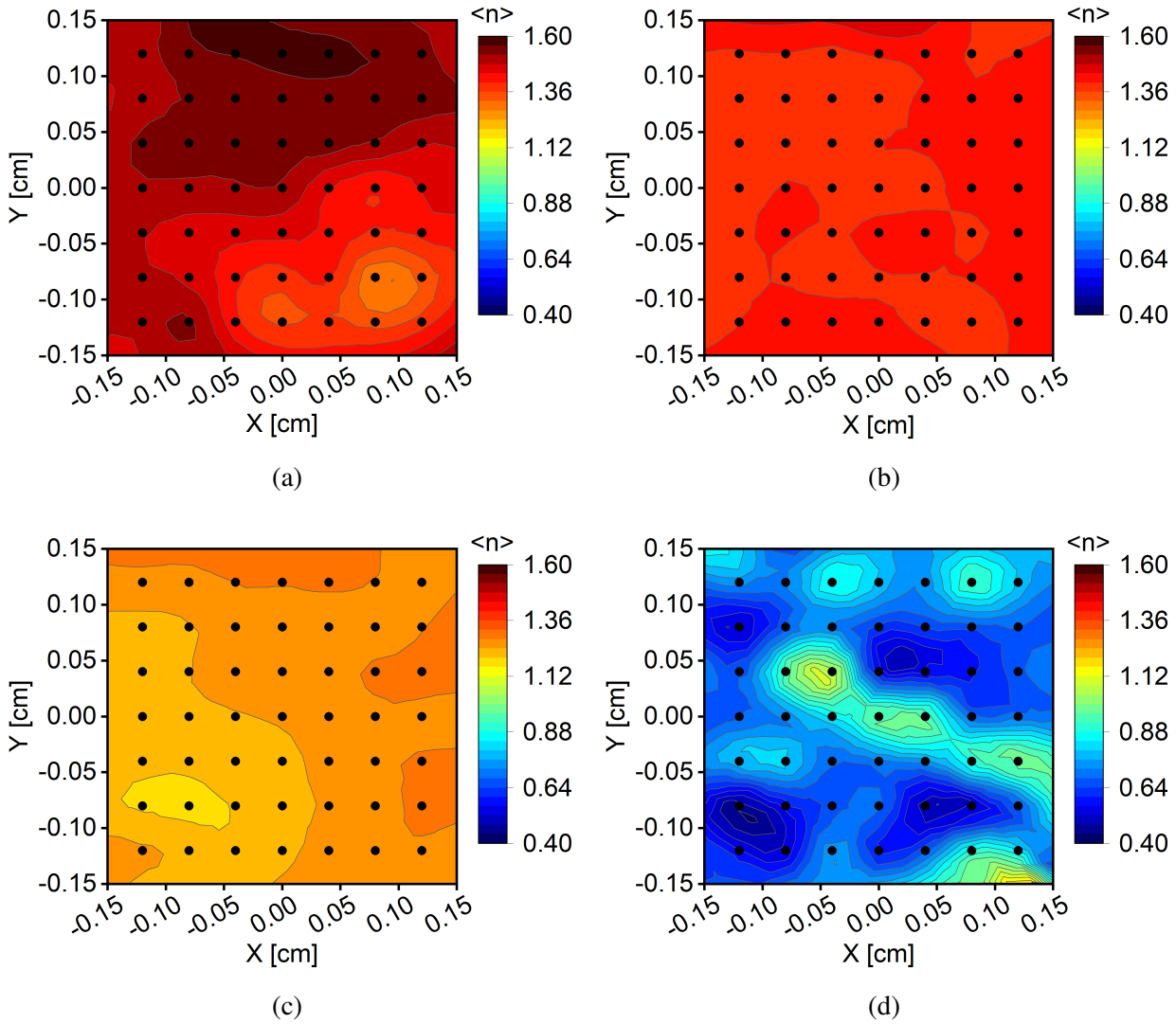

Figure 4.40. Maps of pseudo refractive index parameter for Cu_2O samples (a) non-implanted and implanted with (b) dose 1, (c) dose 2, (d) dose 3 [107].

It is possible to compare only two samples before and after implantation. Their homogeneity is comparable, but pseudo refractive index parameter <*n*> decreases to a very large extent after implantation. This behaviour is in contrary to CuO and Cu_2O for which <*n*> value increased after implantation. Maps of total thickness calculated using model presented in previous subsection, are presented in Figure 4.42. Non-implanted sample shows higher range and values of the total thickness compared to implanted one. This is in accordance with results achieved from optical analysis modelling (Figure 4.39a).

AFM was used to characterise roughness of Cu_2O thin films before and after implantation. The device used was atomic force microscope Dimension ICON from Bruker in tapping mode. Resulting micrographs are presented in Figure 4.43

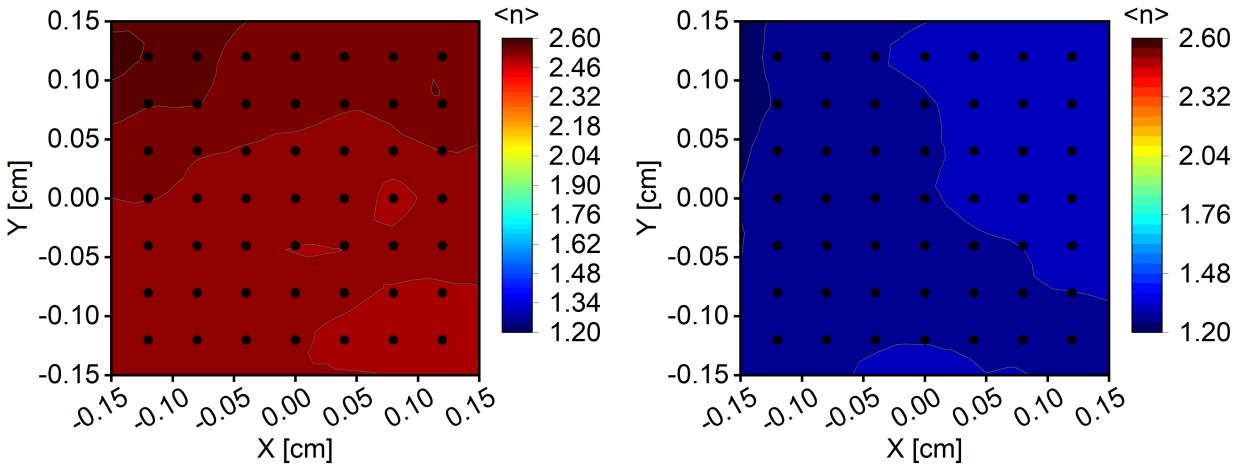

Figure 4.41. SE measurement data, Psi and Delta, for Cu_2O samples (a) before and (b) after annealing measured at 65°angle. (a) Psi and (b) Delta for non-implanted sample measured at various angles.

The roughness of the samples was evaluated using two parameters: R_a (arithmetical mean deviation of the assessed profile) and R_{max} (maximum valley depth below the mean line). The R_a parameter of non-implanted sample was 3.5 nm, and was higher for implanted samples: dose 1 - 5.2 nm, dose 2 - 5,3 nm, dose 3 - 5.1 nm. R_{max} values were: non-implanted - 62.7 nm, dose 1 - 51.2 nm, dose 2 - 79.9 nm, dose 3 - 58.5 nm. The average roughness is higher for implanted samples than non-implanted sample, while maximum valley depth has no dependence on the dose of implantation.

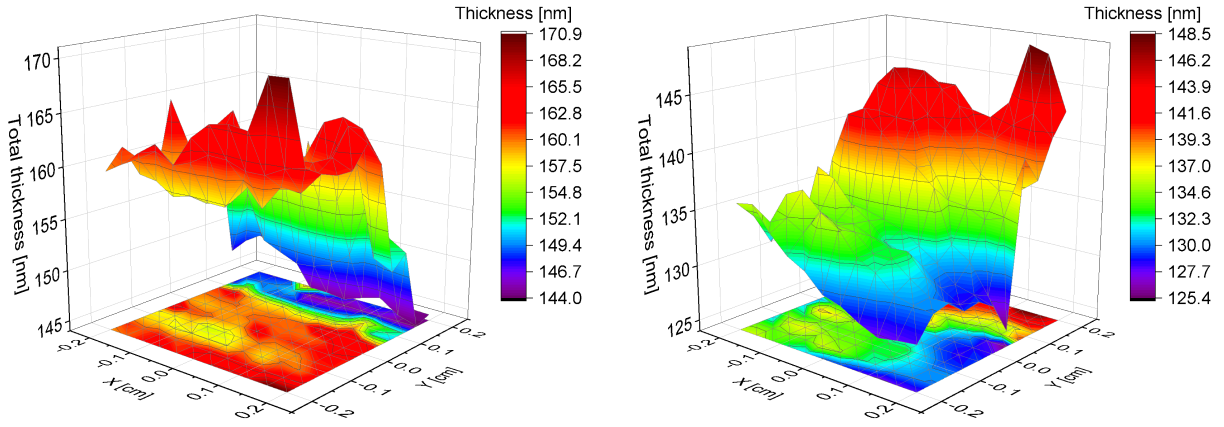

(a) (b)

Figure 4.42. Total thickness three dimensional maps of Cu_4O_3 (a) non-implanted and (b) implanted samples.

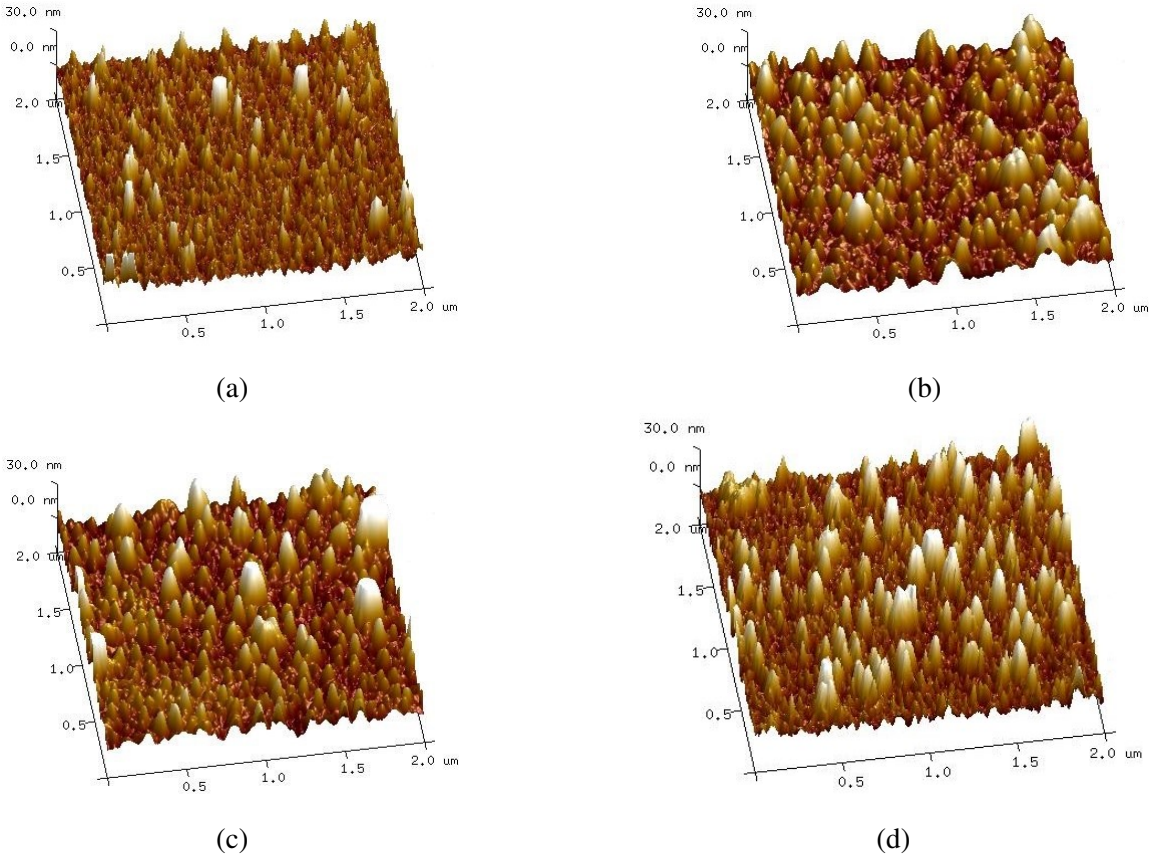

(a) (b)

(c) (d)

Figure 4.43. Atomic force microscopy 3D surface micrographs of Cu_2O samples (a) non-implanted, implanted with 10 keV Cr ions of doses (b) $1x10^{14}$ cm^{-2}, (c) $5x10^{14}$ cm^{-2} and (d) $1x10^{15}$ cm^{-2}[109].

4.4.4 Surface chemical state of Cu_2O

Annealed Cu_2O samples were characterised with X-ray Photoelectron Spectroscopy. The surfaces were measured after a mild cleaning with Ar^+ sputtering to remove the contamination at the surface (3 minutes in 3.3 x 10^{-7} mbar Ar^+ pressure). The narrow spectra for all of the core levels were measured on a Kratos Ultra DLD spectrometer using a monochromatised Al Kα source that has 1486.6 eV energy. The source was operated at 144 W (12 mA and 12 kV), and the analyser in fixed transmission (FAT) mode with pass energy of 20 eV. The charging effects were compensated using a charge neutraliser during the measurements and a correction of the binding energies to carbon contamination at 284.6 eV as a first step of data analysis. The measurements were performed at National Institute of Materials Physics in Magurele, Romania. All data analysis was done in Igor Pro software. For O 1s level Shirley background was used and for Cu 2p Total Sum background. The peaks were fitted with Voigt function as in case of CuO study.

For XPS analysis non-implanted and samples implanted with dose 2 and dose 3 were chosen. Wide scans for all three films are presented in Figure 4.44. No Cr was detected with XPS, as probably the implantation doses were too small. Similarly to CuO samples Na was detected in the surface of the materials. Figure 4.45 shows Cu LMM Auger spectra which are a good indicator of what type of copper is present in the material. Implanted samples exhibit characteristic shape for Cu^{1+} while non-implanted has a shape typical for Cu^{2+} [119]. In this graph the energy where Cr 2p core level would give signal is marked with an arrow.

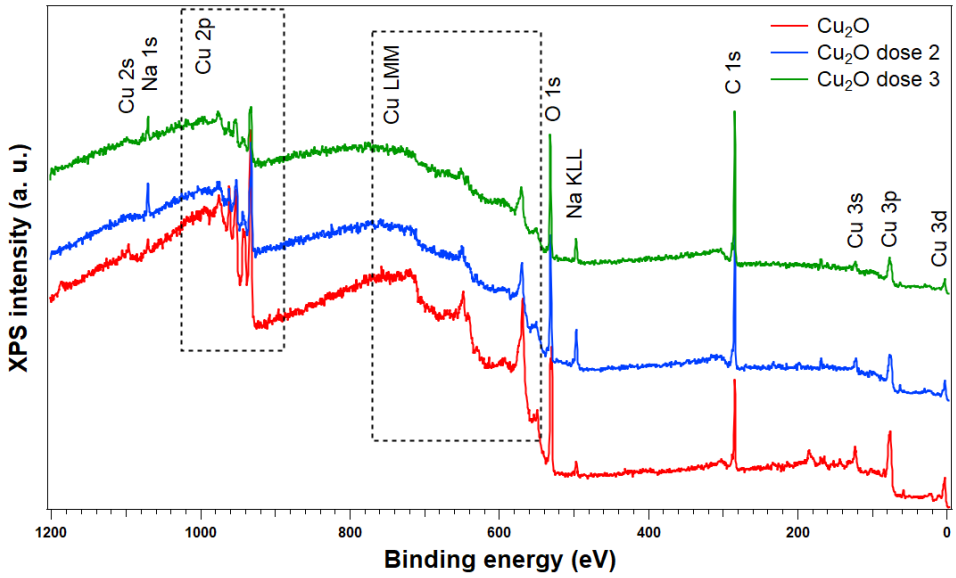

Figure 4.44. Wide XPS scans for Cu_2O samples, the most important signals from detected elements are marked on the figure.

The narrow spectra of Cu 2p level, presented in Figure 4.46a, give qualitatively similar result. Implanted samples show the main Cu $2p_{3/2}$ peak at around 932 eV *BE*, which is characteristic for

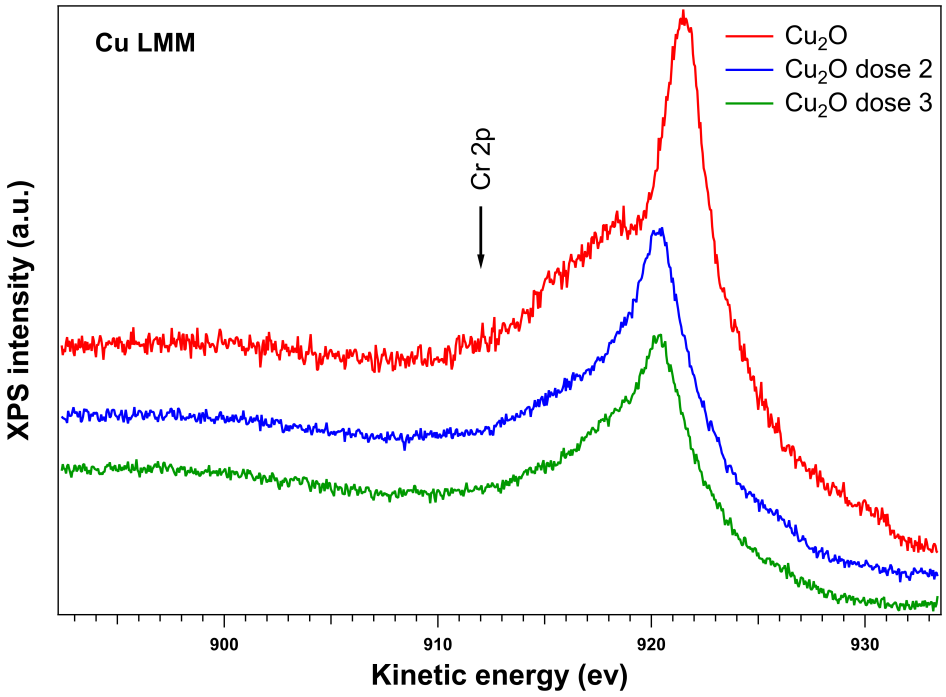

Figure 4.45. Cu LMM Auger spectra for Cu_2O samples.

Table 4.10. The relative contribution of components for O 1s signal for Cu_2O annealed samples.

	Relative contribution in O 1s [%]				
Sample	CuO	Cu_2O	defective CuO	defective Cu_2O	adsorbates
Cu_2O annealed	41.3	12.78	20.21	18.08	7.63
Cu_2O dose 2 annealed	-	21.9	-	69.54	8.56
Cu_2O dose 3 annealed	-	13.43	-	76.85	9.72

copper in Cu_2O with weak shake-up satellites present. Non-implanted sample has much stronger shake-up satellites and the Cu 2p peaks are very wide. The cu 2p $_{3/2}$ comprises of two main contributions at 934.2 eV and 932.6 eV which correspond to Cu^{2+} and Cu^{1+}, respectively. The O 1s level spectra provide more information regarding adsorbates and defects in the films (Figure 4.46b). The relative contribution percentage of all components are presented in Table 4.10.

Non-implanted sample shows the most intensive peak at 529.58 eV which corresponds to oxygen bound to copper in CuO oxide. There is also signal from defects on CuO at 531.15 eV. This sample shows signal from Cu_2O as well, lattice Cu_2O at 530.49 eV and defective at 531.75 eV. At the highest energies two contributions from organic adsorbates are present. Implanted samples show no CuO peak, but the dominating signal comes from defective Cu_2O with contribution form lattice Cu_2O as well. For sample implanted with dose 2 the ratio of lattice Cu_2O to defective Cu_2O is 0.31, and for sample implanted with dose 3 the ratio is 0.17. For both implanted samples sig-

nal form adsorbates is present at around 533 eV and at high *BE* of 536 eV, this last one can be contributed to gas phase CO_2 [120].

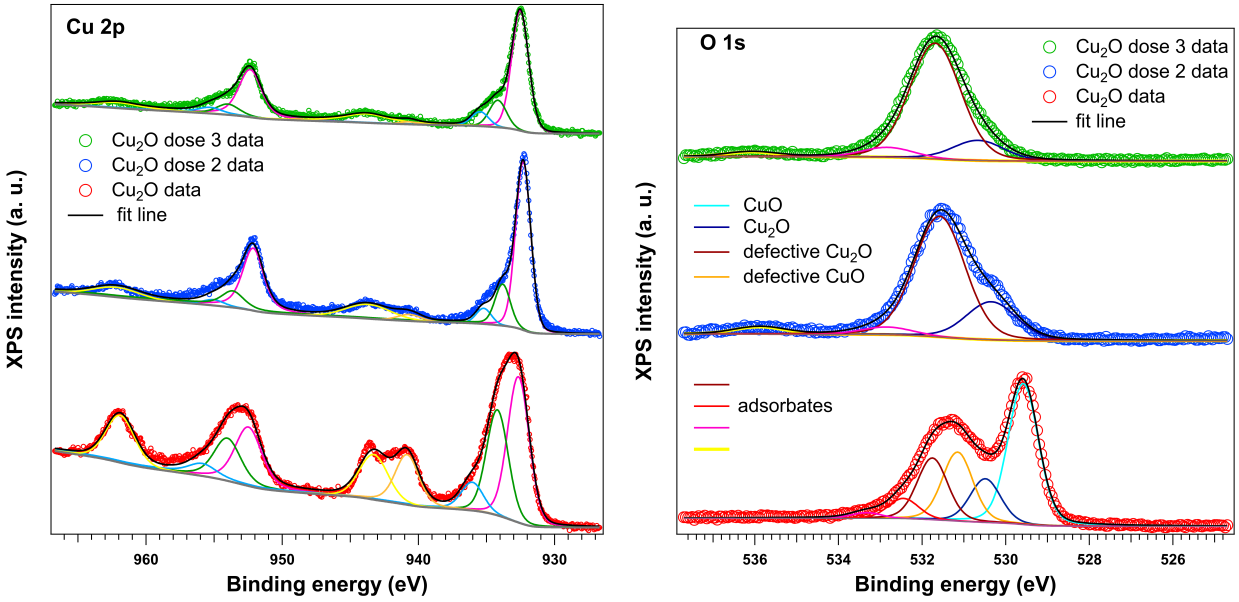

(a) (b)

Figure 4.46. (a) Cu 2p and (b) O 1s spectra for Cu_2O samples.

4.5 Conclusions

The influence of Cr ion implantation on the properties of copper oxides, particularly CuO, was extensively studied. XRD measurements confirmed that implantation damages the crystal structure. For the thinnest sample, around 30 nm, no crystalline peaks of CuO were detected, while thicker samples around 50 nm exhibited significant crystal damage, though the main peaks were still visible. A 130 nm sample showed clear CuO peaks, indicating that the most pronounced effects of implantation on the crystal structure occur up to about 60 nm. Similar observations were made for Cu_4O_3 films. Annealing at 400°C for 6 hours did not result in significant changes in the crystal structure of either CuO or Cu_2O.

Absorption measurements revealed that implantation decreases the light absorption of both CuO and Cu_2O. Implantation at 10 keV across different doses showed that higher doses resulted in a greater reduction in absorption. Annealing restored the absorption properties of implanted CuO and positively affected the conductivity of CuO thin films. The highest conductivity was observed in a sample implanted with 10 keV ions at a dose of $1x10^{-14}$, following annealing.

Annealing Cu_2O in an Ar atmosphere deteriorated the non-implanted sample, as confirmed by spectroscopic ellipsometry, spectrophotometry, and XPS studies. XPS provided further insight,

showing that the non-implanted sample had more CuO contributions than the implanted and annealed samples, suggesting that implantation stabilises Cu_2O at the surface. This could be advantageous for solar cell applications, where the issue of a CuO interface between Cu_2O and the n-type layer has been observed by researchers [121, 122, 123].

Spectroscopic ellipsometry proved valuable in characterising implanted materials. Dielectric function models based on energy transitions in copper oxides were developed. Multilayered models indicated that the thickness of films affected by implantation is up to 30-40 nm, corresponding well with SRIM simulations. Additionally, implantation increased the roughness of layers, a finding corroborated by AFM measurements of CuO and Cu_2O. The ellipsometer also provided map measurements that showed implantation causes non-uniformity, while annealing improves the uniformity of CuO films. Particularly useful were the quick pseudo-refractive index maps, which are fast to produce without requiring complex modelling.

XPS was utilised to create a depth concentration profile of Cr in CuO thin films. The measurements were successful, clearly showing a peak in Cr concentration as predicted by SRIM simulations. After annealing, Cr distribution became uniform throughout the film.

Spectrophotometry and spectroscopic ellipsometry were used to analyse the optical properties of CuO thin films. Absorbance measurements revealed that implantation decreased light absorption, but annealing restored it. Ion implantation with subsequent annealing can be used to engineer the band gap of CuO thin films. Spectroscopic ellipsometry combined with modelling is a viable tool to analyse the changes in materials, clearly the roughness of samples increased after implantation and decreased then with annealing. The top layers of models are most influenced by implantation as is expected after such material processing. The properties of implanted films after annealing are closer to the properties of non-implanted sample, which is a desired effect, as this indicates crystal structure restoration and homogenisation of the layers. Ellipsometry with mapping measurements proved to be a useful method for thin films homogeneity assessment.

Overall, Cr ion implantation had a positive influence on CuO layers with propertly chosen energy and dose, improving their electrical properties while maintaining good light absorption after annealing. The DFT calculations indicated that such doping should have positive effect on the electrical properties of CuO. Cr implantation could also be used to stabilise Cu_2O oxide and prevent its reduction to CuO.

Chapter 5

Influence of proton irradiation - simulation of space conditions

Proton irradiation was employed to simulate the effects of the space environment, which was discussed in Section 1.6. The materials selected for this experiment were copper oxide (CuO) and two transparent conducting oxides, ITO and AZO. The initial section of this chapter details the sample preparation and irradiation process. The following section presents the results of the CuO thin films, analysing their properties before and after irradiation. Then, ITO and AZO characterisation is presented and discussed. The chapter concludes by summarising the key findings from the conducted studies.

5.1 Proton irradiation experiment

The irradiation experiment was conducted at the Institute of Nuclear Physics Polish Academy of Sciences in Kraków. Proton beams with an energy of 226.5 MeV and a fluence of 10^{11} cm^{-2} was used. The homogeneity of samples area irradiation was 9.99%. The experiment lasted for one hour and was performed in air at room temperature.

5.2 CuO

5.2.1 Structural properties

The structural characteristics for CuO samples were obtained with X'PertPro PANalitycal diffractometer with Cu anode working at 40 kV and 40 mA. The measurement employed the grazing incident angle technique with the angle of 1°. The step size was 0.4°and time per step 5 s. Diffractograms of the CuO samples are presented in Figure 5.1. The range was set to show the most characteristic CuO peaks and detect any possible peaks from other copper oxides, which was not the case. For both samples the main peaks for CuO are visible: (110), two double peaks (-111) & (002) and (111) & (200) as identified with ICDD card #01-080-1268. The positions of peaks do not change after proton irradiation. Only the intensity ratio slightly changes, the double peak (111) & (200) becomes more dominant.

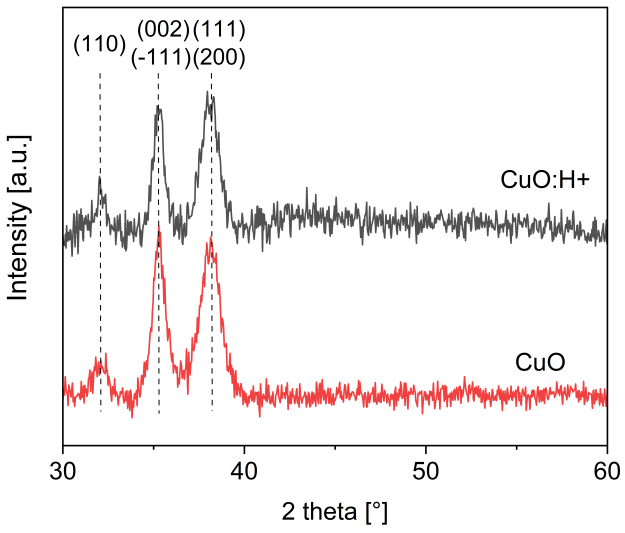

Figure 5.1. Diffractograms of as deposited CuO and sample irradiated with protons CuO:H+, the most important peaks for CuO are identified.

Raman spectroscopy was employed to study structure of CuO as well with HORIBA LabRAM HR Evolution Scientific Raman Spectrometer. The measurements used 633 nm laser and were set at 10 accumulations each of 10 s duration. The results are showed in Figure 5.2. In spectra of

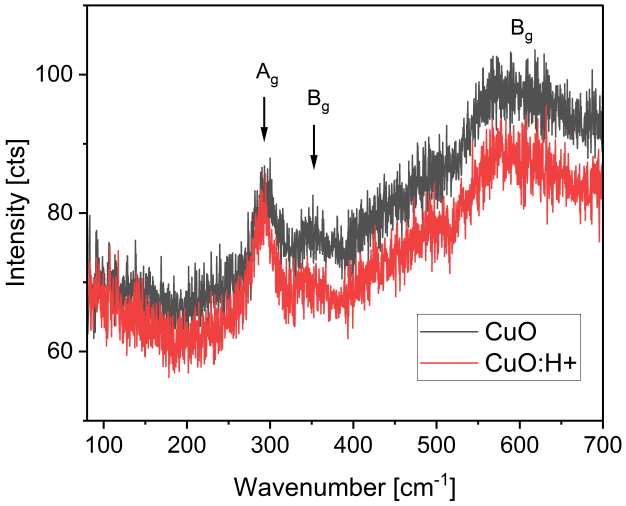

Figure 5.2. Raman spectra for as deposited CuO and irradiated sample CuO:H+, for each film three vibrational modes are assigned.

both samples there are three modes visible: A_g at approximately 300 cm^{-1} and two B_g modes at approximately 350 and 600 cm^{-1}. The signal contains high level of noise for both samples and no structural changes can be observed from these results.

5.2.2 Optical properties

The light absorption of CuO thin film before and after proton irradiation was characterised with spectrophotometry measurements. The resulting absorbance spectra is presented in Figure 5.3. There is a slight decrease of absorption for higher wavelengths (> 500nm).

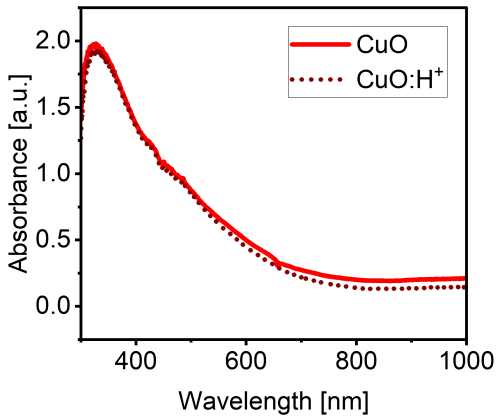

Figure 5.3. Absorbance of CuO thin films before and after proton irradiation.

Spectroscopic ellipsometry is highly sensitive to changes in thin film materials. Figure 5.4 presents the Psi and Delta values measured for three incident angles 65°, 70°, 75°. For both parameters the curves are basically identical, small differences are present only for 75°angle.

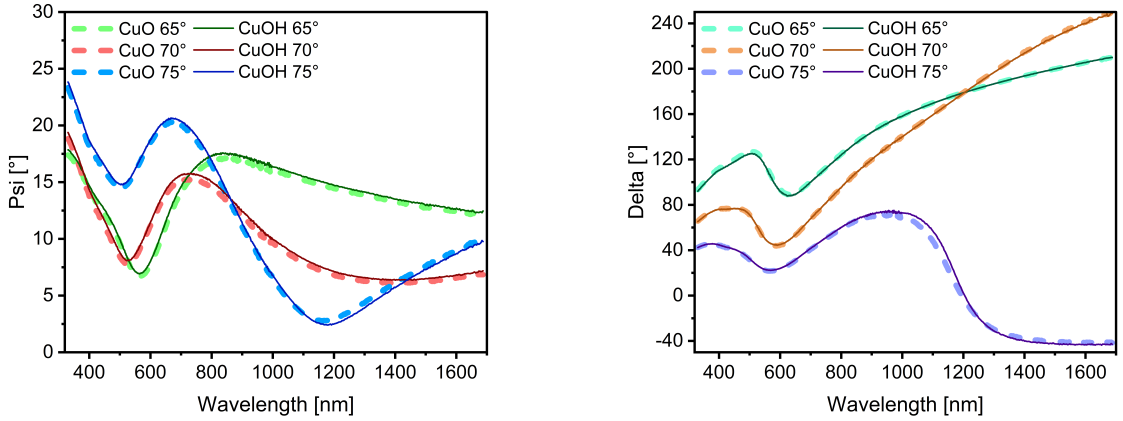

(a) (b)

Figure 5.4. Spectroscopic ellipsometry data (a) Psi and (b) Delta for CuO samples before and after proton irradiation.

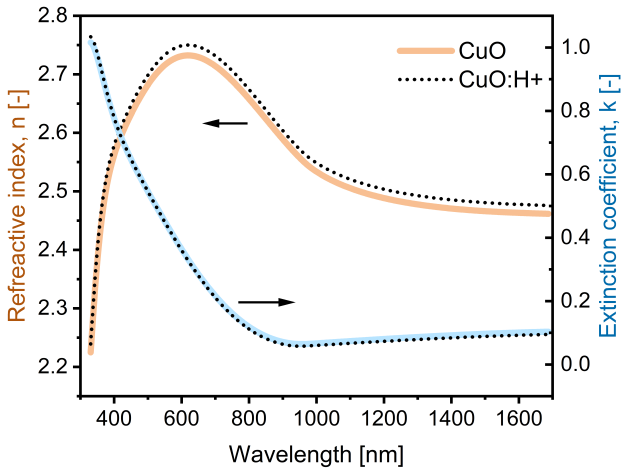

Figure 5.5. Refractive index n and extinction coefficient k of as deposited CuO and irradiated sample CuO:H+.

Dielectric function model was used to fit this data and extract the refractive index and extinction coefficient values. The model consisted of only one CuO layer made with four Tauc-Lorentz oscillators and a roughness layer. The positions of the oscillators were based on transition energies from [39] that were: 1.66 eV, 2.07 eV, 2.68 eV, 3.46 eV and 6.0 eV. The oscillators had positions at, for as deposited CuO: 0.99 eV, 2.56 eV, 3.71 eV and 7.20 eV, for irradiated sample: 0.97 eV, 2.59 eV, 3.71 eV and 7.96 eV.

Fitting with five instead of four oscillators resulted with worse fit quality that was monitored with Mean Squared Error value (MSE). For performed fittings the MSE was 3.590 for CuO and 4.275 for CuO:H+. The data and fit line for both samples are presented in Figure 5.6. It can be seen that the curves appear identical. Calculated thickness and roughness of CuO layers were follows:

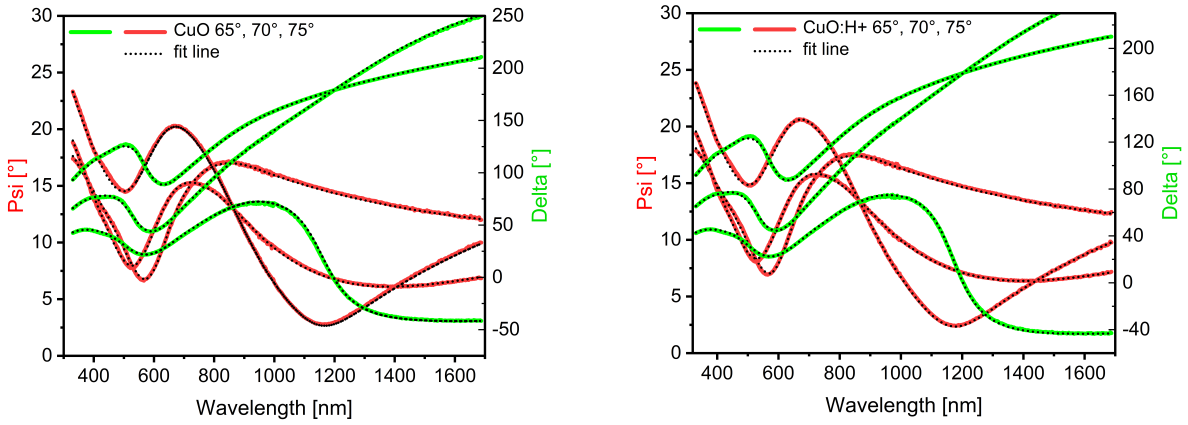

(a) (b)

Figure 5.6. Spectroscopic ellipsometry data (coloured lines) and fit lines (dotted lines) for (a) as deposited CuO and (b) irradiated sample CuO:H+.

115.8 nm and 10.4 nm for CuO and 115.5 and 11.9 nm for CuO:H+. The calculated thickness is the same for both samples but the irradiated one has higher roughness and larger MSE of the fit. From this can be concluded that proton irradiation slightly increased the non-uniformity of CuO thin film with scarce influence on optical properties.

5.2.3 Electrical properties

Electrical properties of CuO thin films were characterised with measurements of sheet resistance. This parameter films was obtained with RM3000+ device from Jandel. For each sample measurements were repeated ten times in three different points. The results were as follows, for as-deposited CuO 8.18 x 10^5 ± 196 Ω/□ and for irradiated sample CuO:H+ 1.00 x 10^6 ± 389 Ω/□. The resistance of material increased by around 20% which is expected as the irradiation introduces more roughness and probably more defects into the film.

5.2.4 Surface chemical state

X-ray photoelectron spectroscopy (XPS) was employed to examine the chemical properties of the CuO films surface. The experimental setup featured an analysis chamber equipped with a 150 mm hemispherical electron energy analyser (Phoibos), operating in fixed transmission mode (FAT) with a pass energy of 20 eV. A monochromatic Al Kα X-ray source, with an energy of 1486.6 eV, was used at 250 W (12.5 kV × 20 mA). Charging effects were mitigated by a flood gun (1V × 0.1 mA) and by applying a binding energy correction to the C 1s contamination peak at 286.4 eV. The XPS data was processed using Igor Pro software.

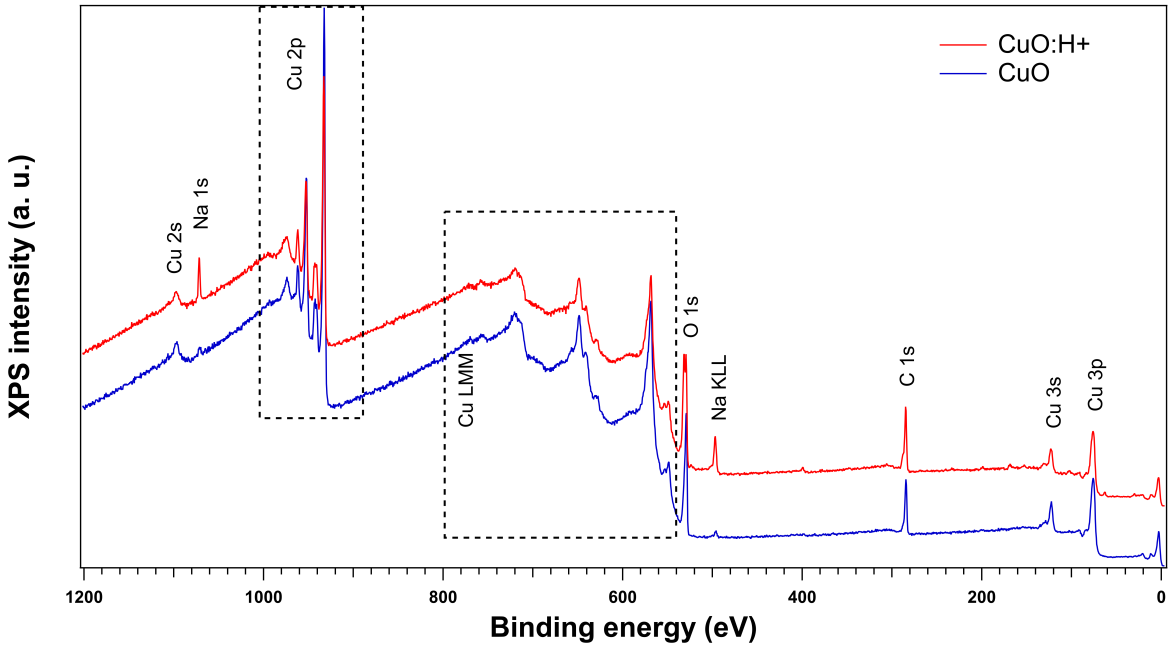

Figure 5.7. XPS wide scan of CuO and CuO:H+ samples.

The wide scans are presented in Figure 5.7. There are signals from copper Cu (3p, 3s, Auger LMM lines, 2p, 2s), oxygen O 1s, carbon from surface contamination C 1s and from sodium Na Auger KLL line and 1 s. Irradiated sample exhibits stronger signal from sodium. Narrow scans were measured for C 1s to calibrate the data, O 1s, and Cu 2p, the last two are shown in Figure 5.8. Both samples exhibited a Cu 2p signal indicative of CuO, characterised by two prominent peaks and shake-up satellites [124]. The main difference after irradiation was a slight reduction in signal intensity and broadening of the two main peaks.

Table 5.1. The relative contribution of components for O 1s signal for CuO as before and after proton irradiation.

	Relative contribution in O 1s [%]		
Sample	CuO	Cu_2O	adsorbates
CuO	61.9	17.8	20.4
CuO: H+	48.8	14.3	36.9

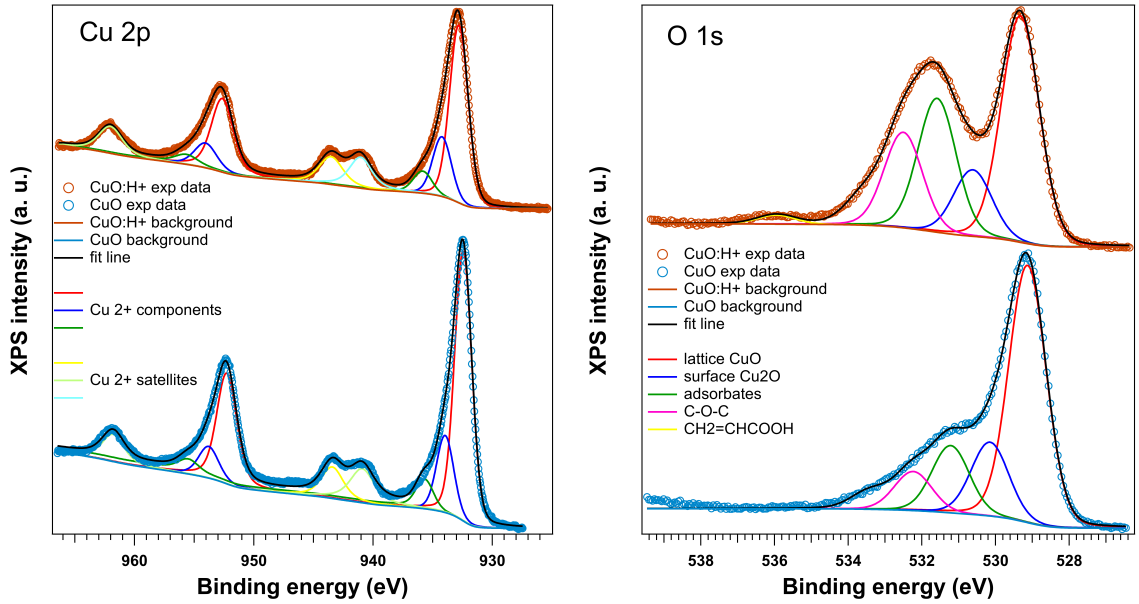

(a) (b)

Figure 5.8. Narrow scan for Cu 2p (a) and O 1s (b) signal with fitted line and components. Bottom line is for non-irradiated sample, line in the top part for irradiated sample.

Notable changes were observed in the O 1s spectra, where the intensity of components related to surface Cu^{1+} and adsorbates increased significantly after irradiation, while the primary O 1s signal from Cu^{2+} weakened. Additionally, a new signal around 536 eV emerged, attributed to organic adsorbates [110]. The relative contributions of signals from CuO (Cu^{2+}), Cu_2O (Cu^{1+}) and adsorbates components are presented in Table 5.1. The fitting-based calculations provide quantitative evidence that irradiation led to an increase in adsorbates and defects on the surface of the CuO thin film.

5.3 Transparent conductive oxides ITO and AZO

5.3.1 Structural properties

The structural properties of ITO and AZO were studied with a Panalytical Empyrean diffractometer using a copper anode (λ = 0.154 nm). The parameters for grazing incidence X-ray diffraction measurement were following 2 theta range from 20 to 80°, step 0.04°, time per step 5 s, omega angle 1°. Resulting diffractograms are presented in Figure 5.9. There is no change in crystal structure of oxides caused by irradiation. The diffractograms are identical before and after the process. The assignment of peaks was done based on ICDD card #00-005-0664 for AZO and ICDD card #00-001-0929 for ITO. ITO appears in structure of the In_2O_3 cubic Ia3 space group no. 206, and AZO in structure of the ZnO hexagonal system group P63mc no. 186.

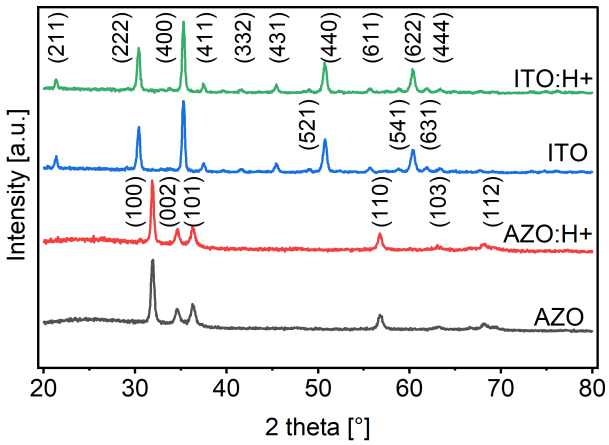

Figure 5.9. X-ray diffractograms of ITO and AZO thin film before and after proton irradiation.

5.3.2 Optical properties

The transmittance of transparent conductive oxides is an important characteristic of these materials. Transmittance of films as measured with an Avantes Sensline Ava-Spec ULS-RS-TEC spectrophotometer and an Avantes AvaLight DH-S-BAL-Hal lamp. For all samples tested, transmittance remained above 80% across all measured wavelengths. After irradiation, the transmittance of AZO decreased in the 400 to 630 nm wavelength range (Figure 5.10b). Meanwhile, the transmittance of ITO showed a slight reduction across the entire measured range (Figure 5.10a).

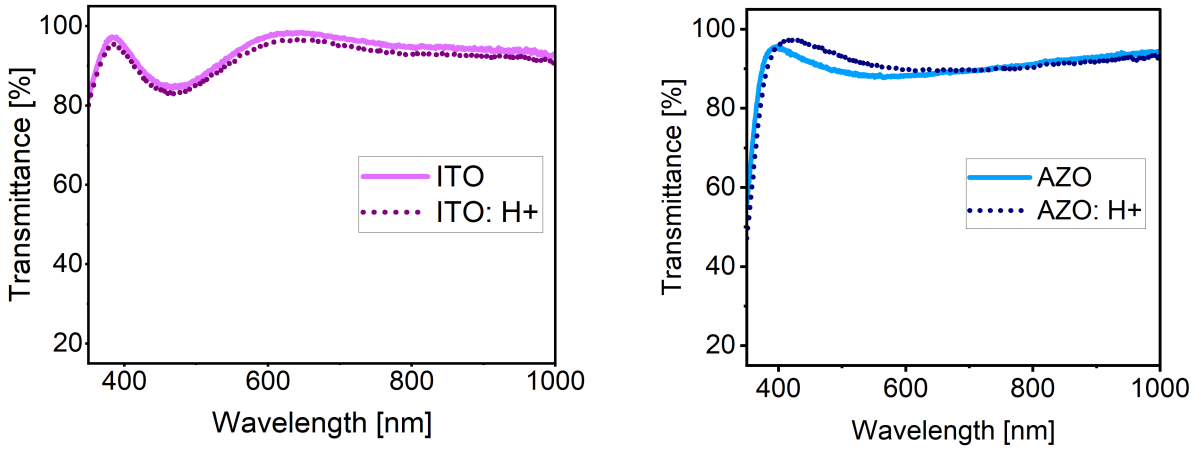

(a) (b)

Figure 5.10. Transmittance measured with spectrophotometry of (a) ITO and (b) AZO samples.

Spectroscopic ellipsometry was used to describe the optical properties, namely refractive index and extinction coefficient. The models used for TCO samples consisted of Tauc-Lorentz, Gaussian and Drude oscillators. AZO model used one oscillator of each type, while ITO had one more Tauc-Lorentz oscillator. This oscillator was previously defined in Equation 4.3.3, while Drude and Gaussian oscillator are defined as follows:

$$\varepsilon_{Gaussian}(E) = Amp(\Gamma(Z^-) + \Gamma(Z^+) + i[exp(-(Z^+)^2)]) \tag{5.1}$$

Where Γ is a convergence series that produces a Kramers-Kronig relation consistent shape of the dielectric function, and Z^+ and Z^- are equivalent to Gaussian "Z-values":

$$Z^+ = (E + E_0)/\sigma_n, Z^- = (E - E_0)/\sigma_n \tag{5.2}$$

Each model consisted of three layers that were calculated with the same oscillators. For AZO the main layer - the thickest - was the middle layer in the model, in case of ITO the main layer was the bottom layer (Figure 5.12). These difference most probably originates from the different deposition methods used for each material. The ITO was obtained as a pre-manufactured product, indicating that its production process is likely more refined compared to the single-sample preparation used for AZO. Industrial manufacturing processes generally result in a better-prepared substrate surface, which explains the absence of a detectable interface in the ellipsometry measurements. The two top layers exhibit distinct characteristics: one forms due to environmental exposure after deposition, while the other represents surface roughness and adsorbates that accumulate during sample handling. For AZO, there is an interface layer between the substrate and the main film.

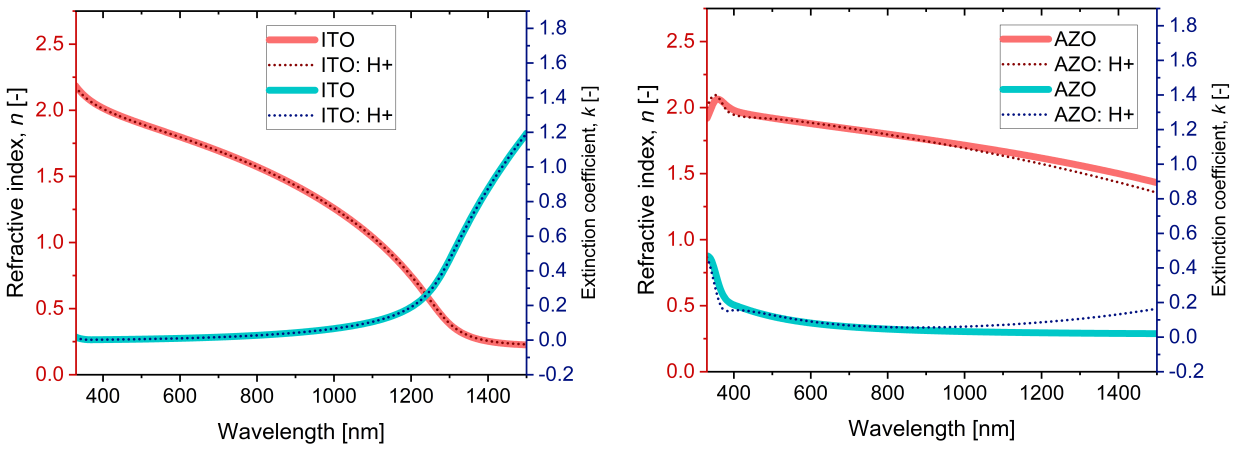

(a) (b)

Figure 5.11. Refractive index n and extinction coefficient k of (a) ITO and (b) AZO samples determined from ellipsometry data fitting.

The optical properties of the thickest layers, are shown in Figure 5.11, they were calculated for chosen representative points from map measurements. The properties of ITO remain unchanged after irradiation, whereas AZO experiences slight alterations. The most significant change occurs in the extinction coefficient at wavelengths above 1000 nm, attributed to increased free carrier absorption in the material [125]. This finding indicates that the number of carriers in AZO has increased, potentially enhancing its conductivity.

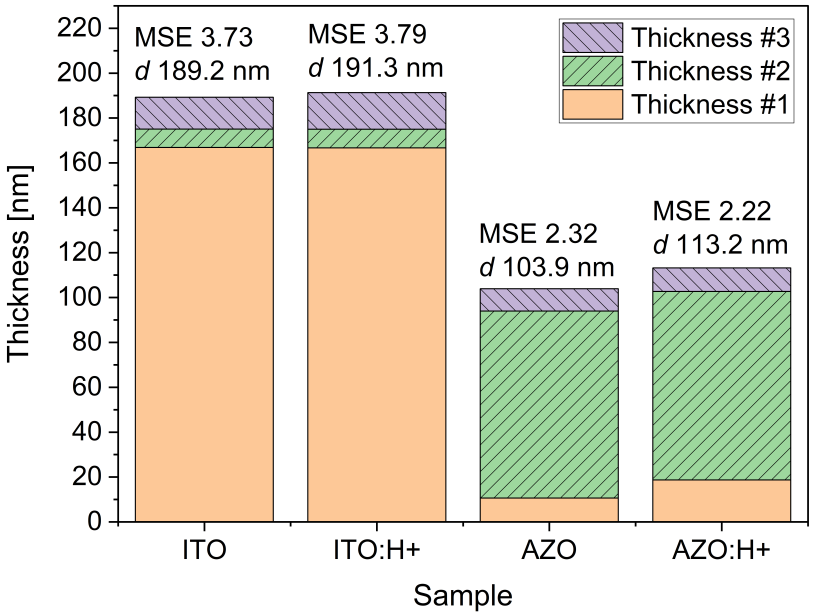

Figure 5.12. Fitting results of dielectric function model to ellipsometry data for AZO and ITO samples, the values are average of map points.

5.3.3 Surface homogeneity

Surface uniformity was assessed in a few manners. First Scanning Electron Microscopy (SEM) observations were made using Phenom microscope from Phenom-World. The SEM images are shown in Figure 5.13.

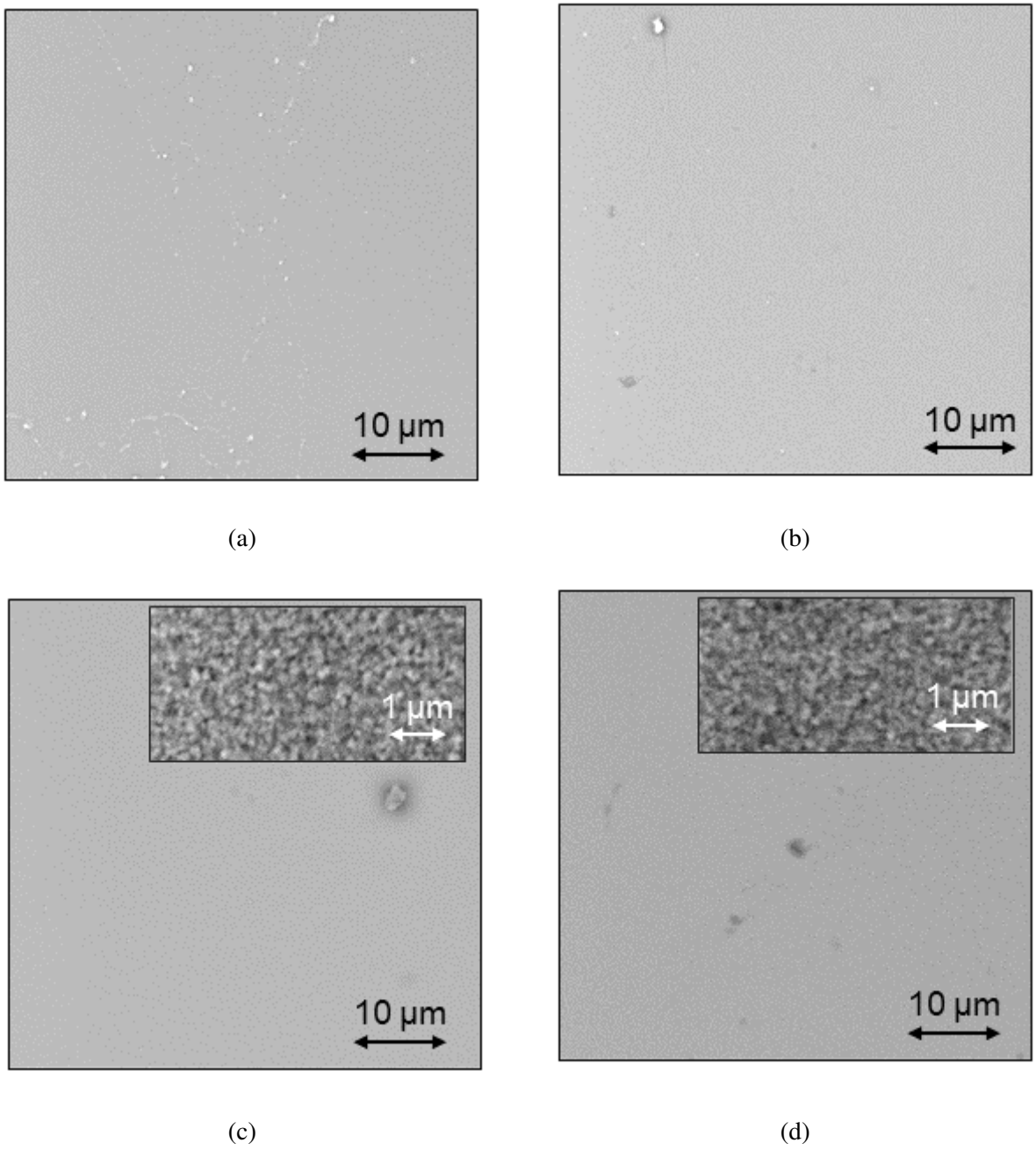

Figure 5.13. SEM images of samples (a) AZO, (b) AZO:H+, (c) ITO, (d) ITO H+.

Microscopic observations show that the films were homogeneous. AZO samples had some precipitates present on the surface. They had an increased amount of Zn, which was measured using energy dispersive spectroscopy (EDS) available within the microscope (Figure 5.14). The

irradiated sample moreover had some other precipitates and impurities (Figure 5.13b) that were not observed for non-irradiated sample (Figure 5.13a). Before and after irradiation, the ITO surface contained some impurities, though their type and quantity remained unchanged. As ITO is highly conductive, the samples were examined at higher magnification, as shown in the insets of Figures 5.13c and 5.13d. The ITO films are composed of grains measuring several hundred nm in size.

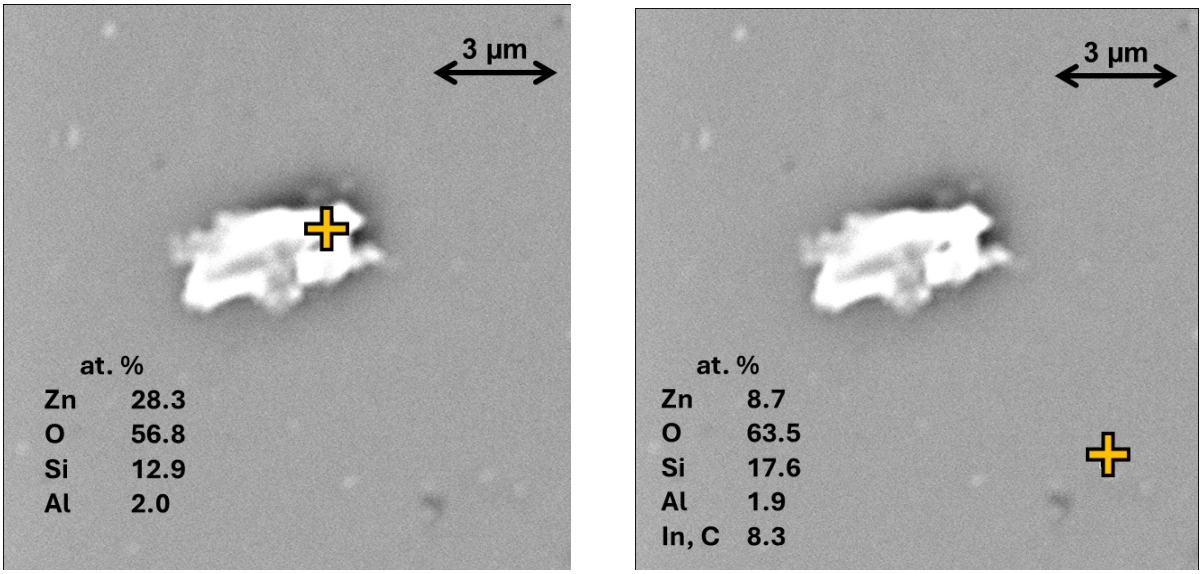

(a) (b)

Figure 5.14. SEM image of a precipitate on AZO sample surface and atomic composition measured with EDS for probing point (a) at the precipitate and (b) at the film surface.

Another way is using spectroscopic ellipsometry and mapping measurements with focusing probes in J.A.Woollam M-2000 ellipsometer. With this method two parameters can be presented: total thickness calculated by fitting model to data and the pseudo refractive index (defined in Section 4.3). Both these approaches were previously presented for copper oxides. Figure 5 shows maps of the total thickness calculated from fitting results, the models used are described in previous section. The maps fittings are very good as the value of the men square error is below 4 for ITO samples and below 3 for AZO samples. The average thickness of AZO was 103.9 ± 2.2 nm, for AZO:H+ 113.2 ± 3.0 nm. this result is close to the expected value of 100 nm. After irradiation the error and total thickness values increased. For ITO, the total thickness is 189.2 ± 0.5 nm, and for ITO:H+ 191.3 ± 1.7 nm, again after irradiation the error increased, but the total thickness increased only slightly. Maps of total thickness are shown in Figure 5.15. Pseudo refractive index is presented in two dimensional form in Figure 5.16. The parameter was calculated for different wavelength for each material, these values were chosen arbitrarily based on where transmittance of the samples changed the most (Figure 5.10), for AZO it was 450 nm and for ITO 600 nm. For both oxides the average value of $<n>$ decreased after proton irradiation but the homogeneity of the films did not change significantly.

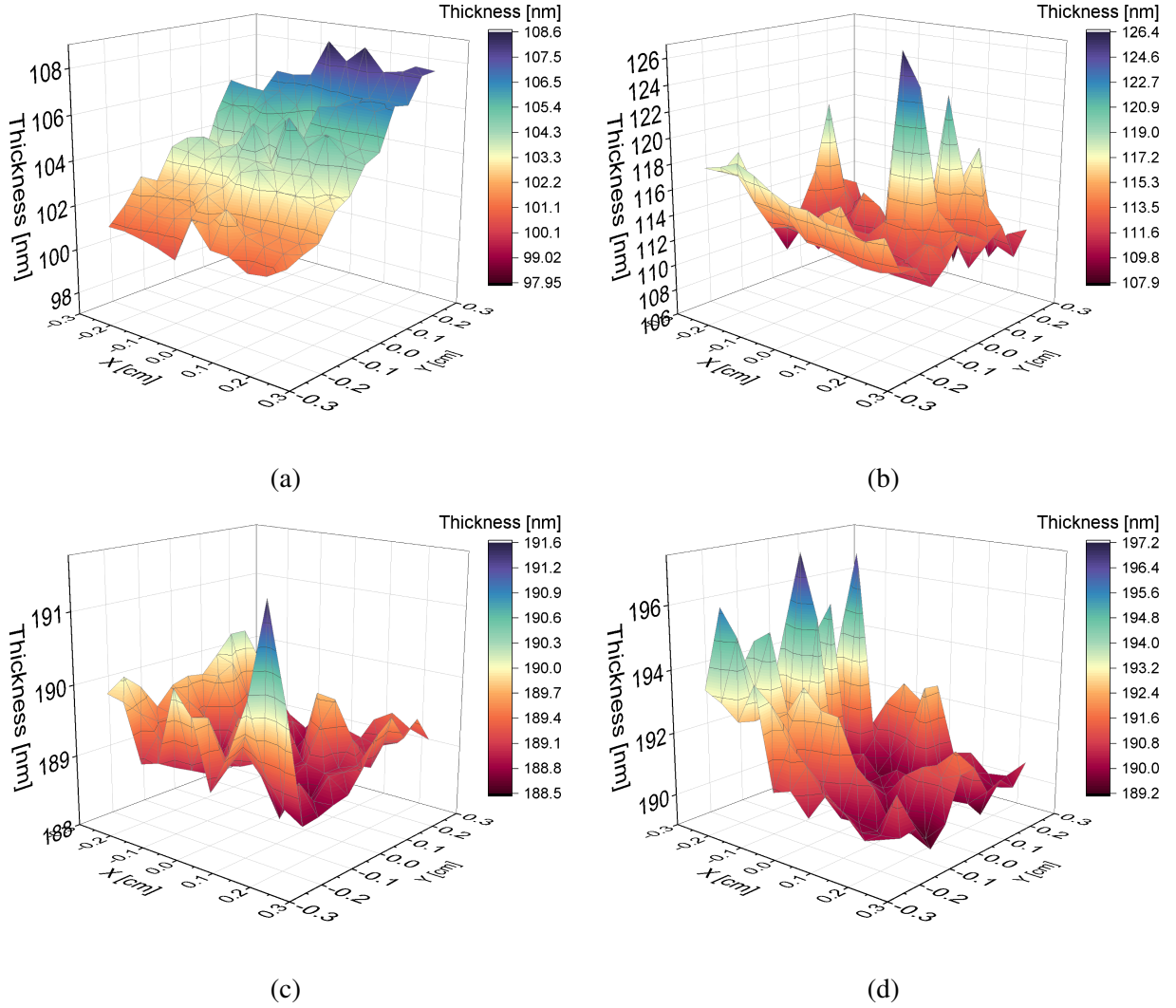

Figure 5.15. Total thickness three dimensional maps of samples (a) AZO, (b) AZO:H+, (c) ITO, (d) ITO H+.

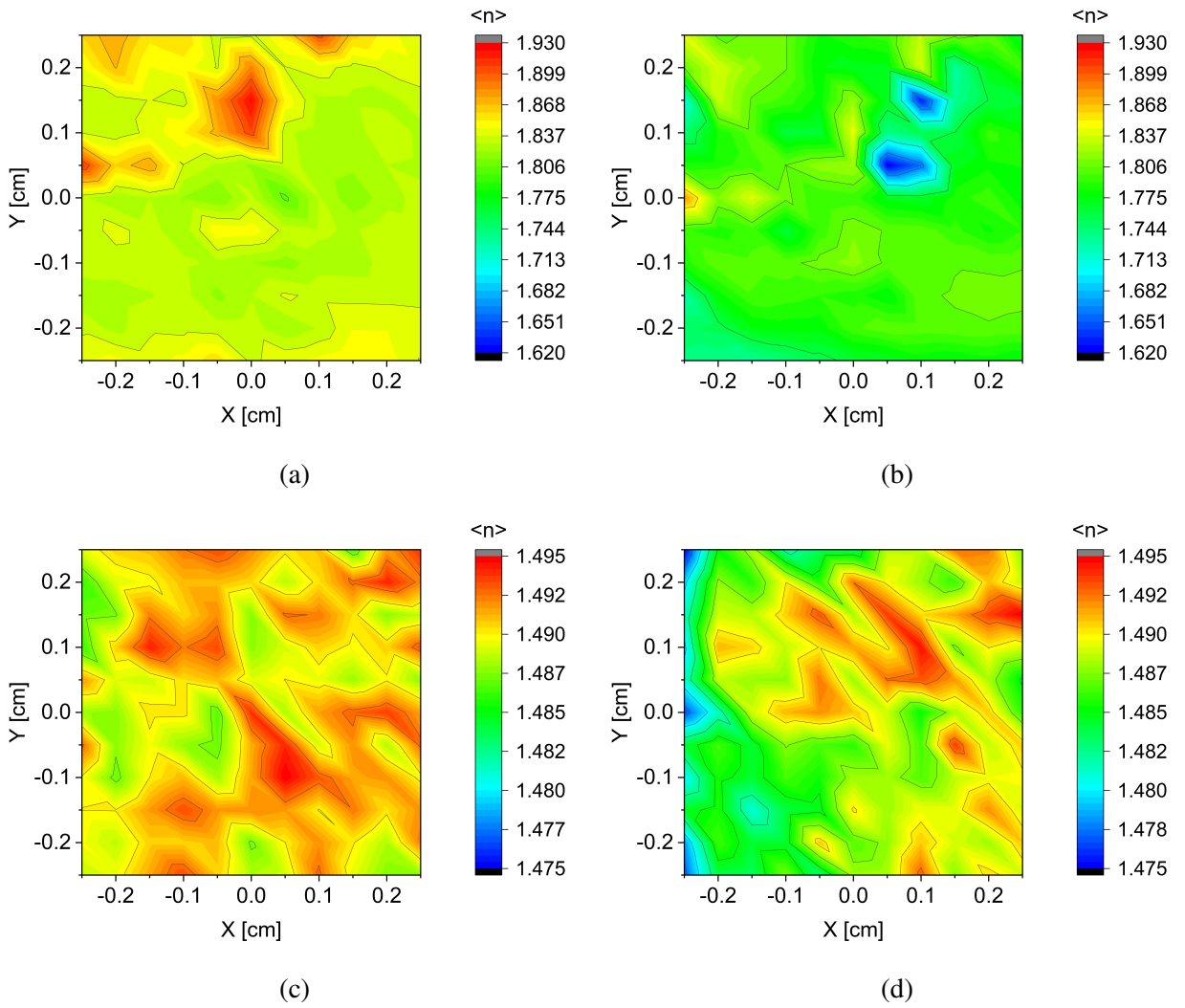

Figure 5.16. Pseudo refractive index maps of samples (a) AZO, (b) AZO:H+, (c) ITO, (d) ITO:H+.

5.3.4 Electrical properties

Electrical properties of transparent conductive oxides were assessed with measurement of sheet resistance. This parameter was measured with Jandel RM3000+ Test Unit that uses a simple four-point probe measurement method. The sheet resistance of AZO film before irradiation was 302.485 $\pm$ 4.413 $\Omega/\square$ and after irradiation 202.347 $\pm$ 0.265 $\Omega/\square$. In case of ITO, it was 9.106 $\pm$ 0.001 $\Omega/\square$ before irradiation and 9.266 $\pm$ 0.010 $\Omega/\square$ after irradiation. The conductivity of AZO increased and ITO decreased after proton irradiation with 226.5 MeV.

5.3.5 Surface chemical state

The chemical properties of the surface of TCO films were examined using X-ray photoelectron spectroscopy. The measurement was performed in an analysis chamber fitted with a 150 mm hemispherical electron energy analyser (Phoibos). The analyser operated in fixed transmission mode (FAT) with a pass energy of 20 eV. The X-ray source used was monochromatised as Al Kα with an energy of 1486.6 eV and a power of 250 W (12.5 kV $\times$ 20 mA). Charging effects were compensated using a flood gun (1 V $\times$ 0.1 mA) and by correcting the binding energy to the C 1s contamination core level at 286.4 eV. The narrow scans were collected for AZO for signals of Al 2p, Zn 2p and O 1s, for ITO for In 3d, Sn 3d and O 1s. They are presented in Figure 5.17 with fitted lines and designated components of signals.

All fittings were conducted in Igor Pro using the Voigt function, which combines Gaussian and Lorentzian functions [112]. In all spectra, the main contribution to the lattice component is associated with lower binding energies, while at higher binding energies (with a difference of approximately 1 eV), surface components are observed, originating from surface defects caused by under-coordinated bonds.

For AZO, the components were attributed as follows: the lattice components are linked to Al 2p at approximately 73.6 eV and Zn 2p at around 1021.4 eV. For O 1s, the binding energies (*BE*) of Al-O and Zn-O are distinguishable, with Zn-O around 530 eV and Al-O at about 531.5 eV. A component with binding energy between these two values is associated with under-coordinated bonds at the surface [126, 127]. Table 5.2 shows the relative contribution of different types of bonds in each spectrum. Surface adsorbates are bound by AlO_x, and since the surface sensitivity of Al is much lower than that of Zn (the Al 2p signal originates from the topmost 7.5 nm, while the Zn 2p signal comes from the topmost 3 nm), it can be assumed that the surface is dominated by AlO_x. This assumption is further supported by the increase in the AlO_x lattice signal after irradiation and the increase in the Al-O component in the O 1s spectrum, while the Zn contribution associated with the lattice component decreases.

The shift of the signal to higher binding energies is linked to the decrease in surface conductivity, as more energy is required to extract a core-level electron. After irradiation, the main

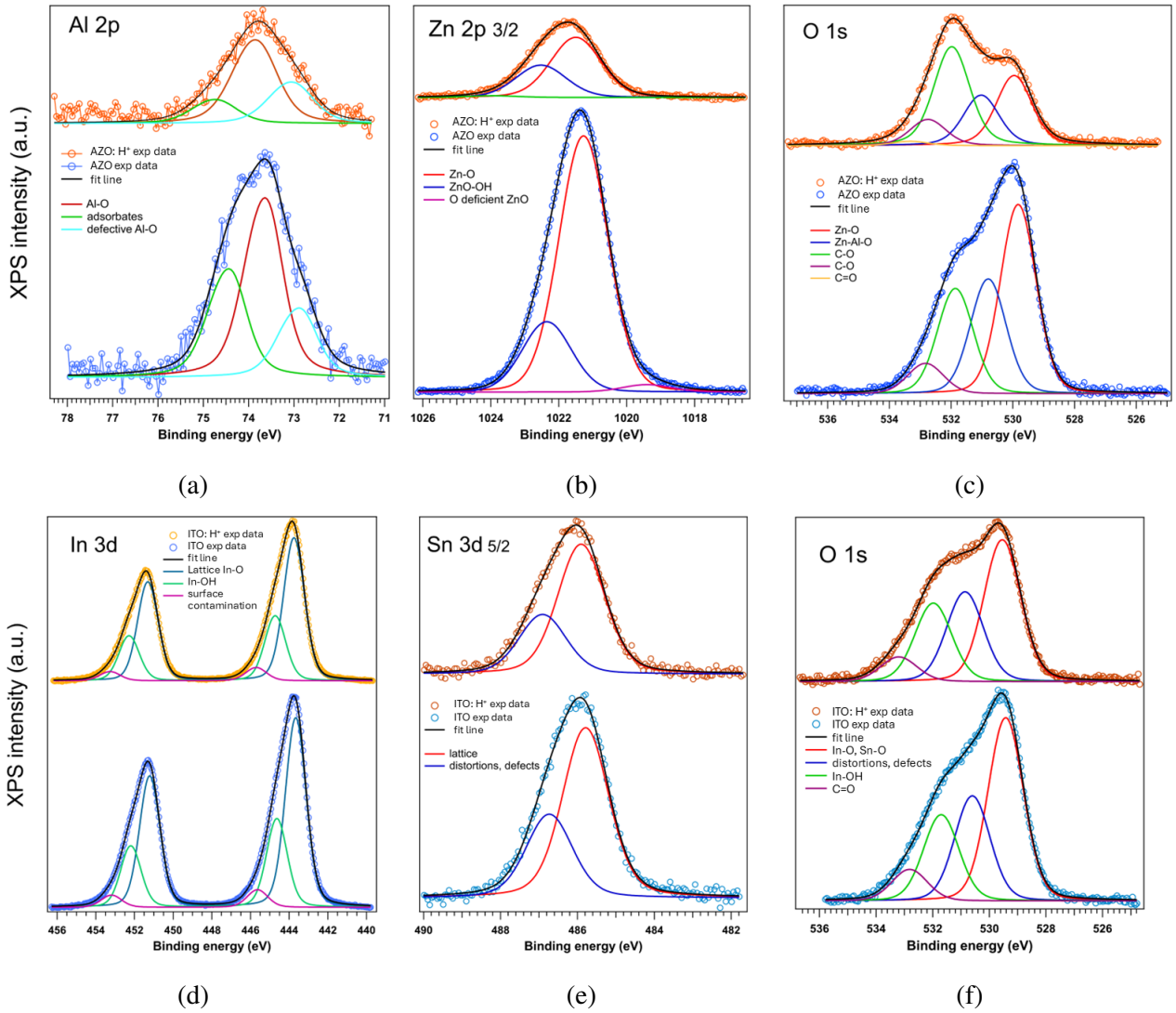

Figure 5.17. Narrow XPS scans with fit lines and distinguished components for AZO samples (a) Al 2p, (b) Zn 2p $_{3/2}$, (c) O 1s and for ITO samples (d) In 3d, (e) Sn 3d $_{5/2}$ (f) O 1s. In all figures the bottom graph is for non irradiated sample and graph in the top for irradiated sample.

component of Al 2p shifted from 73.6 eV binding energy to 73.8 eV, and the main component of Zn 2p shifted from 1021.3 eV binding energy to 1021.5 eV. For O 1s, the Zn-O component shifted from 529.8 eV to 530 eV, and the Al-O component shifted from 531.8 eV to 532 eV. All secondary components of Al 2p, Zn 2p, and O 1s also shifted to higher energies. This suggests that the resistance of AZO is likely to increase after proton irradiation. This behaviour is consistent with a surface dominated by AlO_x, which is a high band gap insulator [128].

In contrast, for ITO, irradiation does not appear to alter the surface, as there is no notable shift in the binding energy of the core levels, nor any change in the surface composition. The only change observed is a slight decrease in the intensity of the O 1s component associated with the In_2O_3 lattice (Figure 5.17f). For ITO, information about the relative concentrations of Sn and In

Table 5.2. The relative contribution of components for Zn 2p, Al 2p, In 3d, Sn 3d and O 1s lines for transparent conductive oxides films before and after proton irradiation.

		Relative contribution [%]		
Sample	Component	Zn 2p	Al 2p	O 1s
AZO	lattice	76.4	50.3	41.3 Zn-O
				23.7 Al-O
	surface	21.3	30.4	
	defects	2.3	19.2	26.8
	adsorbates			8.3
AZO: H+	lattice	64.8	56.5	27.2 Zn-O
				39 Al-O
	surface	33.5	15.7	
	defects		27.8	20.2
	adsorbates	1.7		13.7
	Component	In 3d	Sn 3d	O 1s
ITO	lattice	64.1	67.2	45.1
	surface	30	32.8	25.9
	defects			29
	adsorbates	5.9		
ITO: H+	lattice	64.4	68.1	41.7
	surface	29.5	31.9	27
	defects			31.3
	adsorbates	6.1		

can be derived from XPS because the kinetic energies of the species of interest are similar, resulting in comparable surface sensitivities. Both samples exhibit an In:Sn ratio of 10:1.

5.4 Conclusions

ITO, AZO and CuO thin films were irradiated with 226.5 MeV proton beam of 1x10^{11} cm^{-2} fluence. The experiment simulated space environment on low Earth orbit. XRD characterisation proved that no structural changes were induced by irradiation for all materials. The optical properties of each material changes slightly, for CuO the absorption decreased for higher wavelengths, for ITO and AZO the absorption increased. Analysis of optical properties (refractive index and extinction coefficient) with spectroscopic ellipsometry showed that CuO and ITO properties did not change while AZO properties changed noticeably for wavelengths lower than 400 nm and higher

than 1000 nm. Transparent conductive oxides films were additionally studied with SEM observations and map measurements with ellipsometer. Microscopic observations showed that ITO did not change with irradiation, whereas on the surface of AZO new defects and larger precipitates emerged. From maps of calculated total thickness, it is concluded that the homogeneity of the films worsened after irradiation, but the maps of pseudo refractive index do not confirm this observation.

XPS was used to examine the surface of all studied materials, and for all the same observation was made that irradiated sample had more defects and adsorbates on the surface, tough this effect was much less significant in ITO case. The peaks of all components in AZO shifted to higher binding energies, which indicates an increase of resistivity. Sheet resistance was measured for all samples. The resistance of CuO increased by 20 %, and ITO resistance increased slightly by less than 2 %. Whereas the sheet resistance of AZO decreased after irradiation. This is with agreement that the absorption by free carrier increased, but contrary to XPS result. The contradiction of XPS and sheet resistivity measurements may be due to a different depth of the material that is probed. In case of XPS only a few nanometres of surface are inspected, while electrodes in the four-point probe measurement can penetrate the surface.

This research shows that the high-energy proton environment has a scarce negative influence on properties of transparent conductive oxide and copper oxide thin films, proving they are good candidates as functional layers in space applications.

Chapter 6

Design of all-oxide photovoltaic systems

The last project was to create a working thin film solar cell. In this chapter the methodology of preparing a cell is presented, where the deposition methods described in Chapter 3 were applied.

6.1 Solar cell system preparation

The cells were prepared in a so-called superstrate configuration, where all the functional layers are deposited on glass, and for the light to reach the cell it must come through the glass first. The first step was preparation of glass substrate with transparent electrode layer on it. ITO covered glass was bought from Merck, with thickness about 200 nm, AZO was deposited with ALD to thickness of about 100 nm. Some area of the electrode had to be etched off to ensure that top and bottom electrodes do not short. The etching was done with bromic acid for ITO and acetic acid for AZO, the masking materials were nail polish and Kapton tape, respectively. Next step was ZnO and CuO deposition, both using magnetron sputtering with no heating of the substrate. The last step was deposition of top metallic electrode with Al evaporation. The process of cell preparation is presented as scheme in Figure 6.1. Each deposition process was performed in a different apparatus.

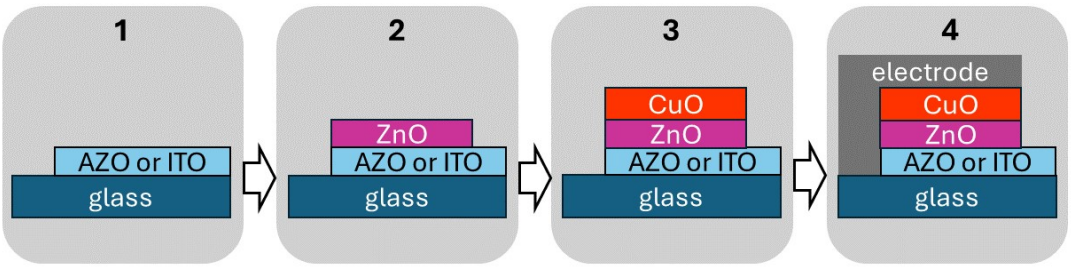

Figure 6.1. Scheme of solar cell preparation.

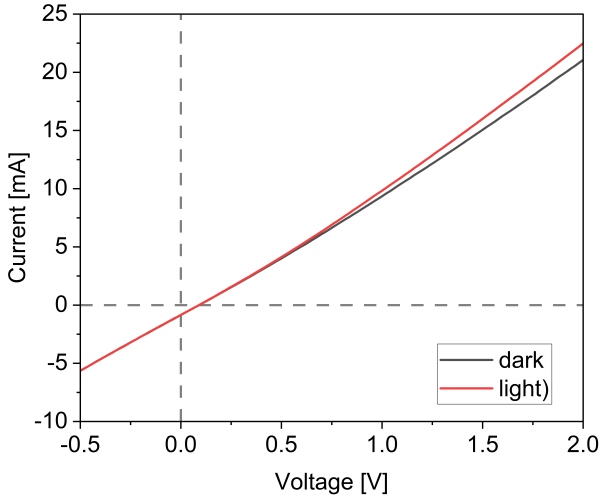

Figure 6.2. I-V curve for cell no 36 measured in dark and under illumination.

More than 40 cells were made in this work, but unfortunately none was a working one, or it was not possible to be measured. To test the cells the SS-X200R Solar Simulator from Enlitech, Taiwan was used. It is equipped with Keysight B2901A SMU meter that was the one used in measurements. Cell no. 36 (ITO/ZnO 100nm/CuO 500nm/Al) which was annealed (400 °C, 6 hours in air) before Al deposition, was used to test the measuring device. Two measurements were performed, one in dark and one with the lamp of solar simulator on. The resulting I-V curves are shown in Figure 6.2. It is clear that no photovoltaic effect is present, moreover the sample does not give a diode characteristic. What is crucial, from these two measurements, is the presence of a current offset of about 0.5 mA and the fact that measurements with this device cannot be considered reliable.

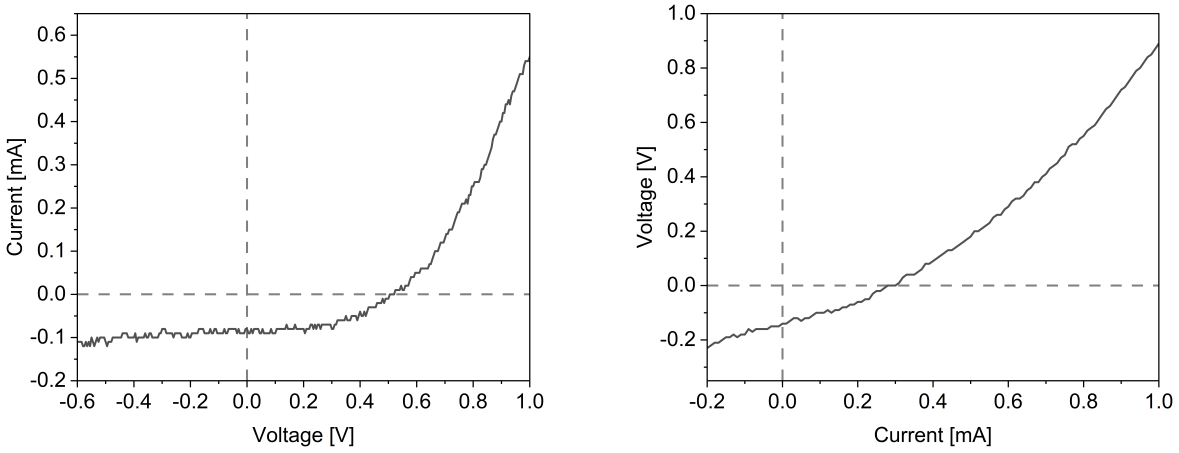

(a) (b)

Figure 6.3. I-V curves for cells no. (a) 2 and (b) 27.

Out of the 40 fabricated samples, only two exhibited diode-like I-V characteristics: cell no. 2 (ITO/ZnO 80 nm/CuO 130 nm/Al) and no. 27 (ITO/ZnO 100 nm/CuO 500 nm/Al). From the I-V

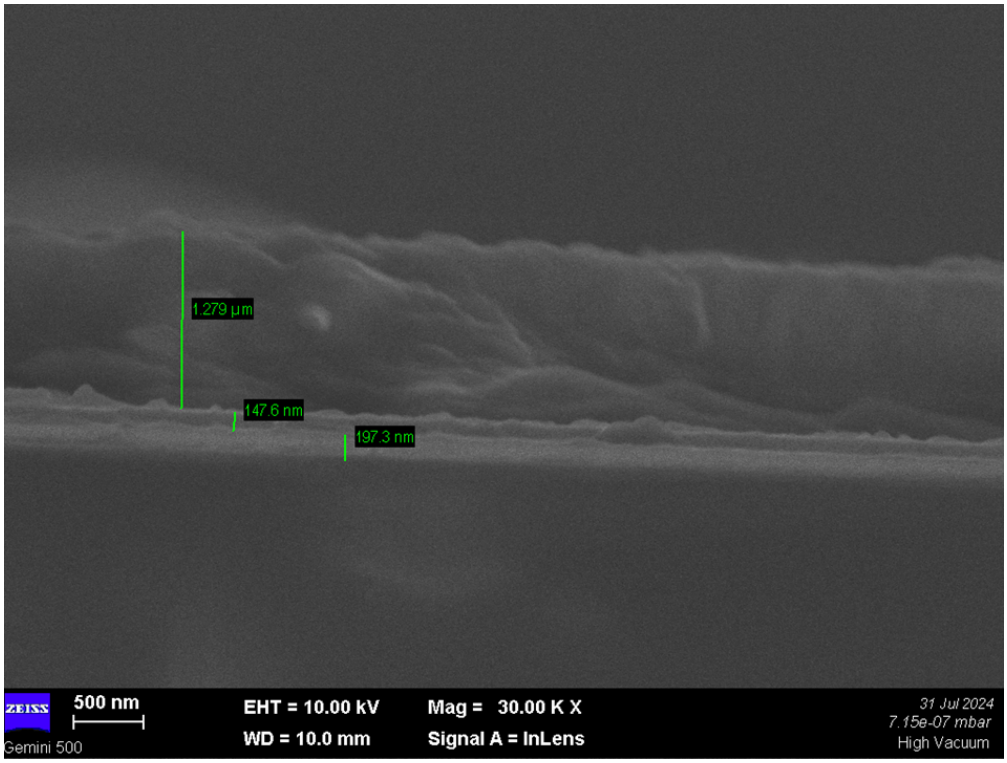

Figure 6.4. SEM image of cell 27 cross section.

curve of cell no. 2 (Figure 6.3a) following photovoltaic parameters can be determined: V_{oc} = 0.5 V, I_{sc} = 0.08 mA, η = 0.18 %, FF = 52 %, but as previously discussed this result is not certain. For sample no. 27 the parameters derived from I-V curve (Figure 6.3b) are as follows: V_{oc} = 0.74 V, I_{sc} = 0.327 mA, η = 0.0975 %, FF = 32.23 %. This result is likely inaccurate, as the open circuit current is lower than the offset determined in Figure 6.2. To further investigate, the cross-section of sample no. 27 was analysed using a ZEISS Gemini SEM 500 field-emission scanning electron microscope, equipped with an EDS detector. EDS measurement provided only one insight into the picture, that the thickest visible layer had much more Al than the other ones. In the SEM image, three distinct layers on the substrate were observed: a 197.3 nm-thick layer (identified as the ITO layer), a 147.6 nm-thick middle layer (likely the ZnO layer), and a top layer measuring 1297 µm (identified as the Al electrode). Notably, the CuO film, expected to be 500 nm thick, was absent. This may indicate that in this specific cross-section, the CuO layer was not deposited, possibly due to the masking of certain areas during the deposition process to leave a clear ITO region for I-V measurements.

6.2 Conclusions

The attempts to create functional thin-film solar cells yielded limited success, with only two out of 40 samples (cells no. 2 and 27) displaying diode-like I-V characteristics. However, the photovoltaic parameters obtained from these cells are uncertain. A test of device measurement with a sample in dark and in light conditions proved that there is a measurement current offset. For cell no. 27 its I-V curve showed a short circuit current smaller than the observed measurement offset, and therefore this measurement and other are not reliable. SEM analysis revealed the absence of the CuO layer in cell no. 27, suggesting incomplete deposition during fabrication or a wrong part of the sample was chosen for observations. Overall, the results highlight significant challenges in the cell fabrication process, impacting the reliability of the measurements and device performance. The fact that each functional layer is deposited in a different apparatus significantly influences the quality of prepared system.

Chapter 7

Summary

With growing energy needs in the world, especially for renewable and clean energy, there is a great need in exploration and research of new and existing materials for energy generation. Particularly in the interest of this work is photovoltaic energy conversion, where in this field it is important to develop alternative materials to silicon technology, especially in form of thin films, which offer the advantages of lower mass and material consumption, as well as flexibility in application.

The research in this work explores a few aspects (i) modification of copper oxides with chromium ion implantation to improve their properties as absorbers for photovoltaics cells, (ii) study of space environment influence on thin film materials (transparent electrodes and copper oxide) via proton irradiation experiment, (iii) preparation of all-oxide thin film solar cells.

(i) The first study considered thin films of CuO, Cu_2O, and Cu_4O_3 deposited with reactive magnetron sputtering. The implantation effect was first simulated with SRIM software and then implanted samples were characterised with many methods. The key findings of this work are listed below.

- SRIM simulations showed that a peak of Cr concentration should occur at about 10 nm in depth of CuO, this peak position determined from SNMS and XPS measurement was between 20 and 30 nm; XPS study of annealed sample proved that the Cr distribution peak was no more present after thermal treatment;

- ion implantation had great impact on the structural properties of thin films, especially up to 60 nm in depth, with total amorphisation in case of the thinnest samples, this was the case for CuO and Cu_4O_3 samples; there were significant changes observed in diffractograms after both implantation and annealing but no clear dependence could be determined;

- ion implantation caused decrease of absorption of CuO and Cu_2O thin films, and annealing restored the absorption;

- sheet resistance of films increased after ion implantation and decreased after annealing;

- good and reliable models of dielectric function were prepared to analyse spectroscopic ellipsometry data, they based on energy transitions that occur in the studied materials which in the model were represented with Tauc-Lorentz oscillators;

- results of fitting ellipsometry data with multilayered models concluded that implantation had great impact on material properties up to 40 nm which agrees with SRIM simulations results;

- surface homogeneity studies with spectroscopic ellipsometry and AFM showed that implantation reduced the uniformity of copper oxides thin films; ellipsometry measurements after annealing proved that homogeneity improved after this process;

- one sample had better properties than a non-implanted oxide: CuO 130 nm implanted with 10 keV energy Cr ions of 1x10^{14} cm^{-2} dose; the absorption and conductivity of this film were superior compared to annealed non-implanted CuO;

- XPS studies of CuO showed that surface of implanted oxide has many more defects and adsorbates than non-implanted sample, and annealing even increased that amount; study of Cu_2O showed an interesting result, that the Cr ion implantation stabilised the oxide, after annealing non-implanted sample had mostly signal from CuO, while implanted samples only from Cu_2O;

- DFT calculations show that with Cr doping CuO has smaller energy band gap, it absorbs light in the larger spectrum range, and finally behaves metallic at doping level of 1 Cr atom per 7 Cu atoms, the results indicate that with Cr doping the conductivity of CuO should improve.

(ii) In addition to Cr ion implantation, the research also investigated the potential of CuO, ITO, and AZO thin films for space applications. The films were subjected to proton irradiation to simulate the conditions experienced in low Earth orbit. The results showed that these materials exhibited strong resilience to high-energy (226.5 MeV) proton exposure:

- there were no significant changes in the crystal structure, as confirmed by XRD measurements;

- optical and surface properties were slightly affected: the absorption of CuO decreased at higher wavelengths, while ITO and AZO showed slight changes in their transmittance spectra;

- the sheet resistance of CuO increased by about 20 %, for AZO decreased and for ITO did not change;

- AZO films after irradiation had more defects and adsorbates, as confirmed with XPS and SEM techniques, the increase of defects amount may be the reason of increased film conductivity;

(iii) The final part of the research focused on the fabrication of thin-film oxide-based solar cells. Despite preparing more than 40 cells, only two samples exhibited diode-like I-V characteristics, though the photovoltaic parameters obtained from these samples were uncertain. There is place for improvement in the technology of cells preparation especially the handling of the samples between different deposition processes.

In summary, Cr ion implantation and subsequent annealing, with optimised energy and dose of ions, can improve the optical and electrical properties of CuO thin films, which confirms the first thesis. SNMS and XPS analyses supported the second thesis, showing a peak in Cr concentration in the implanted CuO layer. After annealing, the Cr distribution became uniform throughout the depth of the sample. The research also revealed that ion implantation could potentially stabilise Cu_2O and prevent its reduction to CuO, which is an important finding for improving the interface quality between Cu_2O and n-type layers in solar cell structures. While the research demonstrated the potential of Cr ion implantation to enhance the properties of copper oxide films, further optimisation and refinement of the fabrication process are necessary to achieve reliable and efficient thin-film solar cells. The proton irradiation experiment showed that transparent conductive oxides and copper oxide films demonstrated good stability under irradiation, indicating their potential for space-based solar energy applications, which confirms the last thesis. All the theses stated before were confirmed with conducted research.

Bibliography

[1] Loiy Al-Ghussain. “Global warming: review on driving forces and mitigation”. In: *Environmental Progress & Sustainable Energy* 38.1, SI (2019), pp. 13–21. ISSN: 1944-7442. DOI: 10.1002/ep.13041.

[2] Alessandro Dosio et al. “Extreme heat waves under 1.5°C and 2°C global warming”. In: *Environmental Research Letters* 13.5 (Apr. 2018), p. 054006. DOI: 10.1088/1748-9326/aab827. URL: https://dx.doi.org/10.1088/1748-9326/aab827.

[3] K. Ungeheuer and K. W. Marszalek. “Pozyskiwanie energii słonecznej w XXI wieku - bezkrzemowe, cienkowarstwowe ogniwa fotowoltaiczne”. In: *Technologie XXI wieku - aktualne problemy i nowe wyzwania.* Lublin: Wydawnictwo Naukowe TYGIEL sp. z o.o., 2021, pp. 7–28. ISBN: 978-83-67104-07-4.

[4] Renewable Energy Division in the Directorate of Energy Markets and Security. *Renewables 2023: Analysis and forecast to 2028*. Tech. rep. International Energy Agency, Paris, 2024.

[5] Fraunhofer Institute for Solar Energy Systems. *Photovoltaics Report, updated: 21 February 2023*. Tech. rep. International Energy Agency, Paris, 2023.

[6] Lucio Claudio Andreani et al. “Silicon solar cells: toward the efficiency limits”. In: *Advances in Physics: X* 4.1 (2019), p. 1548305. DOI: 10.1080/23746149.2018.1548305.

[7] Jizheng Wang. “Open-circuit voltage, fill factor, and heterojunction band offset in semiconductor diode solar cells”. In: *EcoMat* 4.6 (2022), e12263. DOI: 10.1002/eom2.12263.

[8] Takahiro Mishima et al. “Development statusofhigh-efficiencyHITsolarcells”. In: *Solar Energy Materials & Solar Cells* 95 (2011), pp. 18–21.

[9] Jonas Pettersson, Tobias Torndahl, and Charlotte Platzer-Bjorkman. “The Influence of Absorber Thickness on Cu(In,Ga)Se2 Solar Cells With Different Buffer Layer”. In: *IEEE Journal of Photovoltaics* 3.4 (2013), pp. 1376–1382. DOI: 10.1109/JPHOTOV.2013.2276030.

[10] Jeyakumar Ramanujama et al. “Flexible CIGS, CdTe and a-Si:H based thin film solar cells: A review”. In: *Progress in Materials Science* 110 (2020), p. 100619.

[11] Marco Barbato et al. “CdTe solar cells: technology, operation and reliability”. In: *Journal of Physics D: Applied Physics* 54.33 (June 2021), p. 333002. DOI: 10.1088/1361-6463/ac04e3. URL: https://dx.doi.org/10.1088/1361-6463/ac04e3.

[12] L. El Chaar, L. A. Iamont, and N. El Zein. “Review of photovoltaic technologies”. In: *Renewable and Sustainable Energy Reviews* (2011).

[13] A. Lakshmanan, Zachariah C. Alex, and S.R. Meher. “Recent advances in cuprous oxide thin film based photovoltaics”. In: *Materials Today Sustainability* 20 (2022), p. 100244. DOI: 10.1016/j.mtsust.2022.100244.

[14] E. Dunlop et al. *Guidelines for PV Power Measurement in Industry*. Tech. rep. European Commission Joint Research Centre, 2010. DOI: 10.2788/90247.

[15] Mojtaba Gilzad Kohan, Isabella Concina, and Alberto Vomiero. “Chapter Six - All-oxide solar cells”. In: *Solar Cells and Light Management*. Ed. by Francesco Enrichi and Giancarlo C. Righini. Elsevier, 2020, pp. 229–246. ISBN: 978-0-08-102762-2. DOI: https://doi.org/10.1016/B978-0-08-102762-2.00006-9.

[16] Amador Pérez-Tomás et al. “Chapter 8 - Metal Oxides in Photovoltaics: All-Oxide, Ferroic, and Perovskite Solar Cells”. In: *The Future of Semiconductor Oxides in Next-Generation Solar Cells*. Ed. by Monica Lira-Cantu. Metal Oxides. Elsevier, 2018, pp. 267–356. ISBN: 978-0-12-811165-9. DOI: https://doi.org/10.1016/B978-0-12-811165-9.00008-9. URL: https://www.sciencedirect.com/science/article/pii/B9780128111659000089.

[17] M. Coll et al. “Towards Oxide Electronics: a Roadmap”. In: *Applied Surface Science* 482 (2019). Roadmap for Oxide Electronics, pushed forward by the TO-BE EU Cost action, pp. 1–93. ISSN: 0169-4332. DOI: https://doi.org/10.1016/j.apsusc.2019.03.312. URL: https://www.sciencedirect.com/science/article/pii/S0169433219309432.

[18] Monica Morales-Masis nad Stefaan De Wolf et al. “Transparent Electrodes for Efficient Optoelectronics”. In: *Advanced Electronic Materials* 3 (2017), p. 1600529. DOI: 10.1002/aelm.201600529.

[19] Anna Isabel Hofmann, Eric Cloutet, and Georges Hadziioannou. “Materials for Transparent Electrodes: From Metal Oxides to Organic Alternatives”. In: *Advanced Electronic Materials* 4 (2018), p. 1700412. DOI: 10.1002/aelm.201700412.

[20] Theodoros Dimopoulos. “Chapter 11 - All-Oxide Solar Cells”. In: *The Future of Semiconductor Oxides in Next-Generation Solar Cells*. Ed. by Monica Lira-Cantu. Metal Oxides. Elsevier, 2018, pp. 439–480. ISBN: 978-0-12-811165-9. DOI: https://doi.org/10.1016/B978-0-12-811165-9.00011-9. URL: https://www.sciencedirect.com/science/article/pii/B9780128111659000119.

[21] T. C. Collins and R. J. Hauenstein. “Fundamental Properties of ZnO”. In: *Zinc Oxide Materials for Electronic and Optoelectronic Device Applications*. Ed. by Cole W. Litton, Donald C. Reynolds, and Thomas C. Collins. John Wiley & Sons, Ltd., 2011, pp. 1–25. ISBN: 978-0-470-51971-4.

[22] Nagaraj G. et al. “Tuning the optical band Gap of pure TiO2 via photon induced method”. In: *Optik* 179 (2019), pp. 889–894. ISSN: 0030-4026. DOI: https://doi.org/10.1016/j.ijleo.2018.11.009. URL: https://www.sciencedirect.com/science/article/pii/S0030402618317534.

[23] David O. Scanlon and Graeme W. Watson. “Undoped n-Type Cu2O: Fact or Fiction?” In: *J. Phys. Chem. Lett* 1 (2010), pp. 2582–2585. DOI: 10.1021/jz100962n.

[24] Amrit Kaphle et al. “Enhancement in the performance of nanostructured CuO–ZnO solar cells by band alignment”. In: *RSC Advances* 10 (2020), p. 7839. DOI: 10.1039/c9ra10771a.

[25] A. Bhaumik et al. “Copper oxide based nanostructures for improved solar cell efficiency”. In: *Thin Solid Films* 572 (2014), pp. 126–133. DOI: 10.1016/j.tsf.2014.09.056.

[26] Abdul Kuddus and Abu Bakar Md. Ismail. “ZnO-CuO Based Inorganic Bulk Heterojunction Solar Cells: Influence of Thickness of the Spin-Coated Bulk-Heterojunction Film”. In: *Advanced Materials Research* 1165 (2021), pp. 131–144. DOI: 10.4028/www.scientific.net/AMR.1165.131.

[27] Tadatsugu Minami, Yuki Nishi, and Toshihiro Miyata. “Efficiency enhancement using a Zn1− x Ge x -O thin film as an n-type window layer in Cu2O-based heterojunction solar cells”. In: *Applied Physics Express* 9 (2016), p. 052301. DOI: 10.7567/APEX.9.052301.

[28] Soichiro Shibasaki et al. “Highly transparent Cu2O absorbing layer for thin film solar cells”. In: *Appl. Phys. Lett.* 119 (2021), p. 242102. DOI: 10.1063/5.0072310.

[29] Tadatsugu Minami, Yuki Nishi, and Toshihiro Miyata. “Heterojunction solar cell with 6% efficiency based on an n-type aluminum gallium–oxide thin film and p-type sodium-doped Cu2O sheet”. In: *Applied Physics Express* 8 (2015), p. 022301. DOI: 10.7567/APEX.8.022301.

[30] Toshihiro Miyata et al. “Photovoltaic properties of low-damage magnetron-sputtered n-type ZnO thin film/p-type Cu2O sheet heterojunction solar cells”. In: *Thin Solid Films* 697 (2020), p. 137825. DOI: 10.1016/j.tsf.2020.137825.

[31] Y. Ievskaya et al. “Fabrication of ZnO/Cu2O heterojunctions in atmospheric conditions: Improved interface quality and solar cell performance”. In: *Solar Energy Materials & Solar Cells* 145 (2015), pp. 43–48. DOI: 10.1016/j.solmat.2014.09.018.

[32] Vinod Kumar et al. “Role of Al doping in morphology and interface of Al-doped ZnO/CuO film for device performance of thin film-based heterojunction solar cells”. In: *Hybrid Advances* 5 (2024), p. 100148. ISSN: 2773-207X. DOI: https://doi.org/10.1016/j.hybadv.2024.100148. URL: https://www.sciencedirect.com/science/article/pii/S2773207X24000095.

[33] Amit Kumar Rana et al. “A transparent photovoltaic device based on Cu2O/ZnO/AZO for see-through applications”. In: *Materials Letters* 255 (2019), p. 126517. ISSN: 0167-577X. DOI: https://doi.org/10.1016/j.matlet.2019.126517. URL: https://www.sciencedirect.com/science/article/pii/S0167577X19311322.

[34] A.E. Rakhshani. “Preparation, characteristics and photovoltaic properties of cuprous oxide—a review”. In: *Solid-State Electronics* 29.1 (1986), pp. 7–17. ISSN: 0038-1101. DOI: https://doi.org/10.1016/0038-1101(86)90191-7. URL: https://www.sciencedirect.com/science/article/pii/0038110186901917.

[35] Markus Heinemann, Bianca Eifert, and Christian Heiliger. “Band structure and phase stability of the copper oxides Cu_2O, CuO, and Cu_4O_3”. In: *Phys. Rev. B* 87 (11 Mar. 2013), p. 115111. DOI: 10.1103/PhysRevB.87.115111. URL: https://link.aps.org/doi/10.1103/PhysRevB.87.115111.

[36] A. H. Pfund. “The Light Sensitiveness of Copper Oxide”. In: *Phys. Rev.* 7 (3 Mar. 1916), pp. 289–301. DOI: 10.1103/PhysRev.7.289. URL: https://link.aps.org/doi/10.1103/PhysRev.7.289.

[37] L. O. Grondahl. “A new electronic rectifier”. In: *Journal of the American Institute of Electrical Engineers* 46 (1927), pp. 215–22.

[38] L. O. Grondahl. “The Copper-Cuprous-Oxide Rectifier and Photoelectric Cell”. In: *Rev. Mod. Phys.* 5 (1933), p. 141. DOI: 10.1103/RevModPhys.5.141.

[39] B. K. Meyer et al. “Binary copper oxide semiconductors: From materials towards devices”. In: *Physica Status Solidi (b)* 249.8 (2012), pp. 1487–1509. DOI: https://doi.org/10.1002/pssb.201248128.

[40] M.R. Alfaro Cruz, D. Sanchez-Martinez, and L.M. Torres-Martínez. "CuO thin films deposited by DC sputtering and their photocatalytic performance under simulated sunlight". In: *Materials Research Bulletin* 122 (2020), p. 110678. ISSN: 0025-5408. DOI: https://doi.org/10.1016/j.materresbull.2019.110678. URL: https://www.sciencedirect.com/science/article/pii/S0025540819308451.

[41] C. E. Ekuma et al. "Electronic structure and spectra of CuO". In: *The European Physical Journal B* 87 (2014). DOI: 10.1140/epjb/e2013-40949-5.

[42] Dahlang Tahir and Sven Tougaard. "Electronic and optical properties of Cu, CuO and Cu2O studied by electron spectroscopy". In: *Journal of Physics: Condensed Matter* 24 (2012), p. 175002. DOI: 10.1088/0953-8984/24/17/175002.

[43] Yaping Zhang et al. "Metal-insulator transition in ferromagnetic Mn-doped CuO thin films". In: *Journal of Applied Physics* 105.8 (Apr. 2009), p. 086103. ISSN: 0021-8979. DOI: 10.1063/1.3116508. eprint: https://pubs.aip.org/aip/jap/article-pdf/doi/10.1063/1.3116508/13295314/086103_1_online.pdf. URL: https://doi.org/10.1063/1.3116508.

[44] Bruno K. Meyer et al. "Chapter Six - The Physics of Copper Oxide (Cu2O)". In: *Oxide Semiconductors*. Ed. by Bengt G. Svensson, Stephen J. Pearton, and Chennupati Jagadish. Vol. 88. Semiconductors and Semimetals. Elsevier, 2013, pp. 201–226. DOI: https://doi.org/10.1016/B978-0-12-396489-2.00006-0. URL: https://www.sciencedirect.com/science/article/pii/B9780123964892000060.

[45] P. Sawicka-Chudy et al. "Optical and structural properties of Cu2O thin film as active layer in solar cells prepared by DC reactive magnetron sputtering". In: *Archives of Metallurgy and Materials* 64.1 (2019), pp. 243–250. DOI: 10.24425/amm.2019.126244. URL: http://www.czasopisma.pan.pl/Content/110157/PDF/AMM-2019-1-35-Sawicka.pdf.

[46] Shogo Ishizuka, Takahiro Maruyama, and Katsuhiro Akimoto. "Thin-Film Deposition of Cu2O by Reactive Radio-Frequency Magnetron Sputtering". In: *Japanese Journal of Applied Physics* 39 (2000), p. L786. DOI: 10.1143/JJAP.39.L786.

[47] P A Korzhavyi and B. Johansson. *Literature review on the properties of cuprous oxide Cu2O and the process of copper oxidation*. Tech. rep. Department of Materials Science, Engineering Royal Institute of Technology, Svensk Kärnbränslehantering AB Swedish Nuclear Fuel, and Waste Management Co, 2011.

[48] Liping Yu and Alex Zunger. "Identification of Potential Photovoltaic Absorbers Based on First-Principles Spectroscopic Screening of Materials". In: *Phys. Rev. Lett.* 108 (2012), p. 068701. DOI: https://doi.org/10.1103/PhysRevLett.108.068701.

[49] Aleksandar Živkovi ć, Alberto Roldan, and Nora H. de Leeuw. “Density functional theory study explaining the underperformance of copper oxides as photovoltaic absorbers”. In: *Phys. Rev. B* 99 (3 Jan. 2019), p. 035154. DOI: 10.1103/PhysRevB.99.035154. URL: https://link.aps.org/doi/10.1103/PhysRevB.99.035154.

[50] L. Debbichi et al. “Vibrational Properties of CuO and Cu4O3 from First-Principles Calculations, and Raman and Infrared Spectroscopy”. In: *The Journal of Physical Chemistry C* 116.18 (2012), pp. 10232–10237. DOI: 10.1021/jp303096m.

[51] Shogo Ishizuka et al. “Nitrogen Doping into Cu2O Thin Films Deposited by Reactive Radio-Frequency Magnetron Sputtering”. In: *Jpn. J. Appl. Phys.* 40 (2001), pp. 2765–2768. DOI: 10.1143/JJAP.40.2765.

[52] Claudia Malerba, Fabio Biccari, Andrea Mittiga, et al. “Effects of nitrogen doping on the optical and electrical properties of Cu2O thin films for intermediate band solar cell applications”. In: *Solar Energy Materials and Solar Cells* 105 (2012), pp. 192–195.

[53] Zohra Nazir Kayani and Hira Aslam. “Investigation of structural, optical, antibacterial, and dielectric properties of V-doped copper oxide thin films: Comparison with undoped copper oxide thin films”. In: *Advanced Powder Technology* 32.9 (2021), pp. 2345–2358.

[54] S. Nithya et al. “Ni doping in CuO: A highly sensitive electrode for sensing ammonia in ppm level using lanthanum gallate based electrolyte”. In: *Materials Research Bulletin* 118 (2019), p. 110478.

[55] S. Pelegrini et al. “Electrodeposited Cu2O doped with Cl: Electrical and optical properties”. In: *Journal of Applied Physics* 123 (2018), p. 161567.

[56] Luo Yu, Liangbin Xiong, and Ying Yu. “Cu2O Homojunction Solar Cells F-Doped n-type Thin Film and Highly Improved Efficiency”. In: *J. Phys. Chem. C* 119 (2015), 22803−22811.

[57] Artur Rydosz and Aleksandra Szkudlarek. “Gas-Sensing Performance of M-Doped CuO-Based Thin Films Working at Different Temperatures upon Exposure to Propane”. In: *Sensors* 15.8 (2015), pp. 20069–20085. ISSN: 1424-8220. DOI: 10.3390/s150820069. URL: https://www.mdpi.com/1424-8220/15/8/20069.

[58] Aleksandra Szkudlarek et al. “Electronic sensitization of CuO thin films by Cr-doping for enhanced gas sensor response at low detection limit”. In: *Mater. Res. Express* 5 (2018), p. 126406. DOI: 10.1088/2053-1591/aae0d8.

[59] Kang-Min Kim et al. “Selective Detection of NO2 Using Cr-Doped CuO Nanorods”. In: *Sensors* 12.6 (2012), pp. 8013–8025. ISSN: 1424-8220. DOI: 10.3390/s120608013. URL: https://www.mdpi.com/1424-8220/12/6/8013.

[60] S. Bhuvaneshwari and N. Gopalakrishnan. “Enhanced ammonia sensing characteristics of Cr doped CuO nanoboats”. In: *Journal of Alloys and Compounds* 654 (2016), pp. 202–208. ISSN: 0925-8388. DOI: https://doi.org/10.1016/j.jallcom.2015.09.046. URL: https://www.sciencedirect.com/science/article/pii/S0925838815310239.

[61] S. Baturay, I. Candan, and C. Ozaydın. “Structural, optical, and electrical characterizations of Cr-doped CuO thin films”. In: *J Mater Sci: Mater Electron* 33 (2022), pp. 7275–7287. DOI: 10.1007/s10854-022-07918-2.

[62] B. J. Sealy. “Ion implantation doping of semiconductors”. In: *International Materials Reviews* 33.1 (1988), pp. 38–52.

[63] J. S. Williams. “Ion implantation of semiconductors”. In: *Materials Science and Engineering* A253 (1998), pp. 8–15.

[64] S. Shi et al. “Argon ion irradiation induced phase transition and room temperature ferromagnetism in the CuO thin film”. In: *J. Phys. D: Appl. Phys.* 49 (2016), p. 055003.

[65] D. Wei et al. “Effect of Cr ion implantation on surface morphology, lattice deformation, nanomechanical and fatigue behavior of TC18 alloy”. In: *Applied Surface Science* 506 (2020), p. 145023.

[66] X. Wei et al. “Enhanced anticorrosion and biocompatibility of a functionalized layer formed on ZK60 Mg alloy via hydroxyl (OH-) ion implantation”. In: *Colloids and Surfaces B: Biointerfaces* 216 (2022), p. 112533.

[67] YP Li. “Ion implantation and dynamic annealing effects in perovskite oxides”. In: *IIT2002:Ion Implantation Technology, Proceedings*. Ed. by B Brown et al. 14th International Conference on Ion Implantation Technology, TAOS, NM, SEP 18-27, 2002. 2003, pp. 716–719. ISBN: 0-7803-7155-0.

[68] Jyoti Yadav et al. “A reversible tuning of Fermi level in BiSbTe3 thin films through ion implantation”. In: *Materials Letters* 306 (Jan. 2022). ISSN: 0167-577X. DOI: 10.1016/j.matlet.2021.130923.

[69] R. V. Hariwal et al. “Favourable tuning of optical absorbance, bandgap and surface roughness of ZnO thin films by C ion implantation at the critical angle”. In: *Applied Surface Science Advances* 7 (2022), p. 100189.

[70] F. Liu et al. “Lattice structures and optical properties of Ce:LYSO crystal waveguides with implanted C, Si and Cu ions”. In: *Journal of Luminescence* 242 (2022), p. 118559.

[71] Mandeep Kaur, Sanjeev Gautam, and Navdeep Goyal. “Ion-implantation and photovoltaics efficiency: A review”. In: *Materials Letters* 309 (2022), p. 131356. DOI: https://doi.org/10.1016/j.matlet.2021.131356.

[72] Jun Luo et al. “Improved photovoltaic performance of dye-sensitized solar cells by carbon-ion implantation of tri-layer titania film electrodes”. In: *Rare metals* 34.1 (2015), pp. 34–39.

[73] J.F. Ziegler, M.D. Ziegler, and J.P. Biersack. “SRIM—The Stopping and Range of Ions in Matter”. In: *Nuclear Instruments and Methods in Physics Research Section B: Beam Interactions with Materials and Atoms* 268.11 (2010), pp. 1818–1823.

[74] S. Bailey and R. Raffaelle. “Practical Handbook of Photovoltaics”. In: Elsevier Ltd., 2012. Chap. Operation of Solar Cells in a Space Environment.

[75] D.M. Murphy et al. “Thin-film and crystalline solar cell array system performance comparisons”. In: *Conference Record of the Twenty-Ninth IEEE Photovoltaic Specialists Conference, 2002.* 2002, pp. 782–787. DOI: 10.1109/PVSC.2002.1190687.

[76] Walter Schimmerling. “The Space Radiation Environment: An Introduction”. In: 2011. URL: https://api.semanticscholar.org/CorpusID:149756669.

[77] Feida Chen et al. “Degradation characteristics and equivalent analysis of InGaAsP space solar cells under proton and neutron irradiation”. In: *Microelectronics Reliability* 151 (2023), p. 115249. ISSN: 0026-2714. DOI: https://doi.org/10.1016/j.microrel.2023.115249. URL: https://www.sciencedirect.com/science/article/pii/S0026271423003499.

[78] G.P. Summers et al. “A new approach to damage prediction for solar cells exposed to different radiations”. In: *Proceedings of 1994 IEEE 1st World Conference on Photovoltaic Energy Conversion - WCPEC (A Joint Conference of PVSC, PVSEC and PSEC)*. Vol. 2. 1994, 2068–2075 vol.2. DOI: 10.1109/WCPEC.1994.521828.

[79] Naruhide Kato and Mutsumi Sugiyama. “Proton irradiation effects on NiO/ZnO visible-light-transparent solar cells for space applications”. In: *Japanese Journal of Applied Physics* 60 (2021), p. 048001. DOI: 10.35848/1347-4065/abea54.

[80] Dae-Weon Kim et al. “Influence of MeV protons on mechanical properties of ITO/aluminum-coated Kapton designed for space missions”. In: *Nuclear Instruments and Methods in Physics Research Section B: Beam Interactions with Materials and Atoms* 266.14 (2008), pp. 3263–3274. ISSN: 0168-583X. DOI: https://doi.org/10.1016/j.nimb.2008.02.011. URL: https://www.sciencedirect.com/science/article/pii/S0168583X08001572.

[81] Q. Wei et al. “Optical and Electrical Properties of Transparent Conductive ITO Thin Films under Proton Radiation with 100 keV”. In: *PRICM-5*. Vol. 475. Materials Science Forum. Trans Tech Publications Ltd, Jan. 2005, pp. 3697–3700. DOI: 10.4028/www.scientific.net/MSF.475-479.3697.

[82] R. Kh. Khasanshin and L. S. Novikov. “The Influence of Proton Irradiation on Properties of Glass with ITO Coating”. In: *Optical Materials* 127 (2019), pp. 888–893. DOI: 10.1134/S0030400X19110146.

[83] Bosco Oryema et al. “Effects of 7 MeV proton irradiation on microstructural, morphological, optical, and electrical properties of fluorine-doped tin oxide thin films”. In: *Surfaces and Interfaces* 28 (2022), p. 101693. DOI: 10.1016/j.surfin.2021.101693.

[84] R. Pietruszka et al. “Abrasion resistance of ZnO and ZnO:Al films on glass substrates by atomic layer deposition”. In: *Surface and Coatings Technology* 319 (2017), pp. 164–169. ISSN: 0257-8972. DOI: https://doi.org/10.1016/j.surfcoat.2017.04.007. URL: https://www.sciencedirect.com/science/article/pii/S0257897217303523.

[85] Natalia Nosidlak et al. “The thermo-optical and optical properties of thin ZnO and AZO films produced using the atomic layer deposition technology”. In: *Journal of Alloys and Compounds* 900 (2022), p. 163313. ISSN: 0925-8388. DOI: https://doi.org/10.1016/j.jallcom.2021.163313. URL: https://www.sciencedirect.com/science/article/pii/S092583882104723X.

[86] L Zhu, G Shao, and J K Luo. “Numerical study of metal oxide heterojunction solar cells”. In: *Semiconductor Science and Technology* 26 (2011), p. 085026. DOI: 10.1088/0268-1242/26/8/085026.

[87] L Zhu, G Shao, and J K Luo. “Numerical study of metal oxide hetero-junction solar cells with defects and interface states”. In: *Semiconductor Science and Technology* 28 (2013), p. 055004. DOI: 10.1088/0268-1242/28/5/055004.

[88] Miho Yasaka. “X-ray thin-film measurement techniques V. X-ray reflectivity measurement”. In: *The Rigaku Journal* 26.2 (2010). ISSN: 2187-9974.

[89] Rekha Yadav et al. “Defect-Induced Phase Transformations in CuO Thin Films by Ag Ion Implantation and Their Gas-Sensing Applications”. In: *The Journal of Physical Chemistry C* 127.24 (2023), pp. 11438–11447. DOI: 10.1021/acs.jpcc.3c01917.

[90] D. Powell et al. “Raman-scattering study of ion-implantation-produced damage in Cu_2O”. In: *Phys. Rev. B* 12 (1 July 1975), pp. 20–25. DOI: 10.1103/PhysRevB.12.20. URL: https://link.aps.org/doi/10.1103/PhysRevB.12.20.

[91] A. Compaan. “Surface damage effects on allowed and forbidden phonon raman scattering in cuprous oxide”. In: *Solid State Communications* 16.3 (1975), pp. 293–296. ISSN: 0038-1098. DOI: https://doi.org/10.1016/0038-1098(75)90171-4. URL: https://www.sciencedirect.com/science/article/pii/0038109875901714.

[92] H. Solache-Carranco et al. “Raman scattering and photoluminescence studies on Cu2O”. In: *2008 5th International Conference on Electrical Engineering, Computing Science and Automatic Control*. 2008, pp. 421–424. DOI: 10.1109/ICEEE.2008.4723375.

[93] P. Hohenberg and W. Kohn. “Inhomogeneous electron gas”. In: *Phys. Rev.* 136 (1964), B864–B871.

[94] W. Kohn and L. Sham. “Self-consistent equations including exchange and correlation effects”. In: *Phys. Rev.* 140 (1965), A1133–A1138.

[95] K. Ungeheuer et al. “DFT electronic structure investigation of chromium ion-implanted cupric oxide thin films dedicated for photovoltaic absorber layers”. In: *Scientific Reports* 14.19830 (2024). DOI: https://doi.org/10.1038/s41598-024-70442-2.

[96] Peter Blaha et al. *WIEN2k an augmented plane wave plus local orbitals program for calculating crystal properties user’s guide revised edition WIEN2k 23.1 (release 01/16/2023)*. Vienna University of Technology, 2023. ISBN: 3-9501031-1-2.

[97] J. Perdew K. Burke and M. Ernzerhof. “Generalized gradient approximation made simple”. In: *Phys. Rev. Lett.* 77 (1996), pp. 3865–3868.

[98] P. Novák et al. “Electronic structure of the mixed valence system (YM)2BaNiO5(M=Ca,Sr)”. In: *Phys. Rev. B* 63.235114 (2001).

[99] Y. Raydugin, V. Naish, and E. Turov. “On the magnetic structure of cupric oxide (CuO): 1. The antiferromagnetism in the lowtemperature”. In: *J. Magn. Magn. Mater.* 102 (1991), pp. 331–338.

[100] J. Ghijsen et al. “Electronic structure of Cu_2O and CuO”. In: *Phys. Rev. B* 38 (16 Dec. 1988), pp. 11322–11330. DOI: 10.1103/PhysRevB.38.11322.

[101] F. Marabelli, G. B. Parravicini, and F. Salghetti-Drioli. “Optical gap of CuO”. In: *Phys. Rev. B* 52 (3 July 1995), pp. 1433–1436. DOI: 10.1103/PhysRevB.52.1433.

[102] Y. P. Varshni. “Temperature dependence of the energy gap in semiconductors”. In: *Physica* 341 (1967), pp. 149–154.

[103] Claudia Ambrosch-Draxl and Jorge O. Sofo. “Linear optical properties of solids within the full-potential linearized augmented planewave method”. In: *Computer Physics Communications* 175.1 (2006), pp. 1–14. ISSN: 0010-4655. DOI: https://doi.org/10.1016/j.cpc.2006.03.005. URL: https://www.sciencedirect.com/science/article/pii/S0010465506001299.

[104] Hiroyuki Fujiwara. *spectroscopic ellipsometry pronciples and applications*. John Wiley & Sons, Ltd, 2003. ISBN: 4 621 07253 6.

[105] *CompleteEASE software manual*. J.A. Woolam Co., Inc., 2024.

[106] T. Ito et al. “Optical properties of CuO studied by spectroscopic ellipsometry”. In: *Journal of the Physical Society of Japan* 67 (1998), pp. 3304–3309. DOI: 10.1143/JPSJ.67.3304.

[107] Katarzyna Ungeheuer and Konstanty Waldemar Marszalek. “Optical properties of copper oxide thin films implanted with chromium ions”. In: *Journal of Vacuum Science and Technology B* 41 (2023). DOI: 10.1116/6.0003135.

[108] Suprakas Sinha Ray. “3 - Structure and Morphology Characterization Techniques”. In: *Clay-Containing Polymer Nanocomposites*. Ed. by Suprakas Sinha Ray. Amsterdam: Elsevier, 2013, pp. 39–66. ISBN: 978-0-444-59437-2. DOI: https://doi.org/10.1016/B978-0-444-59437-2.00003-X. URL: https://www.sciencedirect.com/science/article/pii/B978044459437200003X.

[109] Katarzyna Ungeheuer et al. “Influence of Cr Ion Implantation on Physical Properties of CuO Thin Films”. In: *International Journal of Molecular Sciences* 23.9 (2022). ISSN: 1422-0067. DOI: 10.3390/ijms23094541. URL: https://www.mdpi.com/1422-0067/23/9/4541.

[110] John F. Moulder, William F. Stickle, and Peter E. Sobol andKenneth D. Bomben. *Handbook of X-ray Photoelectron Spectroscopy*. Perkin-Elmer Corporation, 1992. ISBN: 0-9627026-2-5.

[111] Fred A. Stevie and Carrie L. Donley. “Introduction to x-ray photoelectron spectroscopy”. In: *Journal of Vacuum Science Technology A* 38 (2020), p. 063204. DOI: 10.1116/6.0000412.

[112] C.M. Teodorescu et al. “An approximation of the Voigt I profile for the fitting of experimental X-ray absorption data”. In: *Nuclear Instruments and Methods in Physics Research Section A: Accelerators, Spectrometers, Detectors and Associated Equipment* 345.1 (1994), pp. 141–147. ISSN: 0168-9002. DOI: https://doi.org/10.1016/0168-9002(94)90983-0. URL: https://www.sciencedirect.com/science/article/pii/0168900294909830.

[113] A. I. Stadnichenko, A. M. Sorokin, and A. I. Boronin. “XPS, UPS, and STM studies of nanostructured CuO films”. In: *Journal Structural Chemistry* 49 (2008), pp. 341–347. DOI: 10.1007/s10947-008-0133-1.

[114] Katarzyna Ungeheuer et al. “Influence of proton irradiation on CuO thin films properties”. In: *Przegląd Elektrotechniczny* (accepted for publication).

[115] *Empirically derived set of atomic sensitivity factors for XPS*. XPS atomic sensitivity factors. URL: http://staff.ustc.edu.cn/~mams/escalab/sfactors.html.

[116] Katarzyna Ungeheuer et al. “Cuprous Oxide Thin Films Implanted with Chromium Ions—Optical and Physical Properties Studies”. In: *International Journal of Molecular Sciences* 23.15 (2022). ISSN: 1422-0067. DOI: 10.3390/ijms23158358. URL: https://www.mdpi.com/1422-0067/23/15/8358.

[117] T. Ito et al. “Optical Properties of Cu2O Studied by Spectroscopic Ellipsometry”. In: *Journal of the Physical Society of Japan* 67 (1998), pp. 2125–2131. DOI: 10.1143/JPSJ.67.2125.

[118] Katarzyna Ungeheuer et al. “Spectroscopic ellipsometry modelling of Cr+ implanted copper oxide thin films”. In: *Scientific Reports* 13 (2023). DOI: 10.1038/s41598-023-49133-x.

[119] Mark C. Biesinger. “Advanced analysis of copper X-ray photoelectron spectra”. In: *Surface and Interface Analysis* 49 (2017), pp. 1325–1334. DOI: 10.1002/sia.6239.

[120] Xingyi Deng et al. “Surface Chemistry of Cu in the Presence of CO2 and H2O”. In: *Langmuir* 24.17 (2008), pp. 9474–9478. DOI: 10.1021/la8011052.

[121] Sang Woon Lee et al. “Improved Cu2O-Based Solar Cells Using Atomic Layer Deposition to Control the Cu Oxidation State at the p-n Junction”. In: *Advanced Energy Materials* 4.1301916 (11 2014). DOI: https://doi.org/10.1002/aenm.201301916.

[122] Jatinder Kaur et al. “All-oxide solar cells based on electrodeposited Cu2O absorber and atomic layer deposited ZnMgO on precious-metal-free electrode”. In: *Solar Energy Materials & Solar Cells* 161 (2017), pp. 449–459. ISSN: 0927-0248. DOI: https://doi.org/10.1016/j.solmat.2016.12.017. URL: https://www.sciencedirect.com/science/article/pii/S0927024816305384.

[123] Yuki Nishi, Toshihiro Miyata, and Tadatsugu Minami. “Effect of inserting a thin buffer layer on the efficiency in n-ZnO/p-Cu2O heterojunction solar cells”. In: *Journal of Vacuum Science & Technology A* 30.4 (Apr. 2012), p. 04D103. ISSN: 0734-2101. DOI: 10.1116/1.3698596. eprint: https://pubs.aip.org/avs/jva/article-pdf/doi/10.1116/1.3698596/14814502/04d103_1_online.pdf. URL: https://doi.org/10.1116/1.3698596.

[124] S. Poulston et al. “Surface Oxidation and Reduction of CuO and Cu2O Studied Using XPS and XAES”. In: *Surface and Interface Analysis* 24 (12 1996), pp. 811–820. DOI: https://doi.org/10.1002/(SICI)1096-9918(199611)24:12<811::AID-SIA191>3.0.CO;2-Z.

[125] H. Fujiwara and R. W. Collins. *Spectroscopic Ellipsometry for Photovoltaics Volume 1: Fundamental Principles and Solar Cell Characterization*. Springer Cham, 2019. ISBN: 978-3-319-75377-5. DOI: https://doi.org/10.1007/978-3-319-75377-5.

[126] Ao Liu et al. “Eco-friendly water-induced aluminum oxide dielectrics and their application in a hybrid metal oxide/polymer TFT”. In: *RSC Adv.* 5 (105 2015), pp. 86606–86613. DOI: 10.1039/C5RA15370K. URL: http://dx.doi.org/10.1039/C5RA15370K.

[127] Zongyi Yue et al. “Excellent crystalline silicon surface passivation by transparent conductive Al-doped ZnO/ITO stack”. In: *Applied Surface Science* 645 (2024), p. 158845. ISSN: 0169-4332. DOI: https://doi.org/10.1016/j.apsusc.2023.158845. URL: https://www.sciencedirect.com/science/article/pii/S0169433223025254.

[128] Takafumi Kamimura et al. “Band alignment and electrical properties of Al2O3/B-Ga2O3 heterojunctions”. In: *Applied Physics Letters* 104.19 (May 2014), p. 192104. ISSN: 0003-6951. DOI: 10.1063/1.4876920. eprint: https://pubs.aip.org/aip/apl/article-pdf/doi/10.1063/1.4876920/10149195/192104_1_online.pdf. URL: https://doi.org/10.1063/1.4876920.

List of publications and conferences

Published articles

- K. Ungeheuer, K. Marszałek, *Pozyskiwanie energii słonecznej w XXI wieku – bezkrzemowe, cienkowarstwowe ogniwa fotowoltaicznej*, **Technologie XXI wieku - aktualne problemy i nowe wyzwania, T. 3**, e-ISBN: 978-83-67104-07-4. — S. 7–28., 2021, Wydawnictwo Naukowe TYGIEL, **20 pkt.**

- K. Ungeheuer, K.W. Marszalek, M. Mitura-Nowak, M. Perzanowski, P. Jelen, M. Marszalek, M. Sitarz, *Influence of Cr ion implantation on physical properties of CuO thin films*, **International Journal of Molecular Sciences**, ISSN 1422-0067. — 2022 vol. 23 iss. 9 art. no. 4541, s. 1–14., DOI: 10.3390/ijms23158358, **140 pkt.**

- K. Ungeheuer, K.W. Marszalek, M. Mitura-Nowak, M. Perzanowski , P. Jelen, Marszalek M., M. Sitarz, *Cuprous oxide thin films implanted with chromium ions—optical and physical properties studies*, **International Journal of Molecular Sciences**, ISSN 1422-0067. — 2022 vol. 23 iss. 15 art. no. 8358, s. 1-13., DOI: 10.3390/ijms23094541, **140 pkt.**

- K. Ungeheuer, K.W. Marszalek, M. Mitura-Nowak, Z. Kakol, *Modification of semiconducting copper oxide thin films using ion implantation* , **Przegląd Elektrotechniczny** / Stowarzyszenie Elektryków Polskich ; ISSN 0033-2097. — 2022 R. 98 nr 9, s. 255–258. — Bibliogr. s. 258, **70 pkt.**

- K. Ungeheuer, K.W. Marszalek, *Strukturalne i optyczne właściwości wygrzewanych cienkich warstw ZnO — Structural and optical properties study of annealed ZnO thin films*, **Materiały Ceramiczne = Ceramic Materials** / Polskie Towarzystwo Ceramiczne, Kraków ; ISSN 1644-3470. — Tytuł poprz.: Ceramika. Materiały Ogniotrwałe ; ISSN: 1505-1269. — 2022 t. 74 nr 1, s. 18–22., **20 pkt.**

- K. Ungeheuer, K.W. Marszalek, *Optical properties of copper oxides thin films implanted with chromium ions*, **Journal of Vacuum Science and Technology B** 41, 062208 (2023), https://doi.org/10.1116/6.0003135, **70 pkt.**

- K. Ungeheuer, K.W. Marszalek, M. Mitura-Nowak, A. Rydosz, *Spectroscopic ellipsometry modelling of Cr+ implanted copper oxide thin films*, **Scientific Reports** (2023) 13:22116, https://doi.org/10.1038/s41598-023-49133-x, **140 pkt.**

- K. Ungeheuer, K.W. Marszalek, W. Tokarz, et al. *DFT electronic structure investigation of chromium ion-implanted cupric oxide thin films dedicated for photovoltaic absorber layers*, **Scientific Reports** 14, 19830 (2024). https://doi.org/10.1038/s41598-024-70442-2, **140 pkt.**

to be published

- K. Ungeheuer, A.E. Bocirnea, D.A. Pikulski, K.W. Marszałek, A.C. Galca, J. Chojenka, T. Fodor, K. Vad, *Influence of proton irradiation on CuO thin films properties*, **Przegląd Elektrotechniczny**, 2024, **70 pkt.**, (accepted for publication)

- K. Ungeheuer, J. Rybak, A.E. Bocirnea, D.A. Pikulski, A.C. Galca, K.W. Marszalek, *Influence of proton irradiation on thin films of AZO and ITO transparent conductive oxides – simulation of space environment*, (submitted to **Applied Surface Science**)

Conferences

- K. Ungeheuer, Hajduk G., Kurczyna D., *Projekt i wytworzenie sportowej łodzi napędzanej energią słoneczną*, T**YGIEL 2021 „interdyscyplinarność kluczem do rozwoju" : XIII interdyscyplinarna konferencja naukowa**, 25-28th March 2021, online, **poster**

- K. Ungeheuer, K.W. Marszalek, Mitura-Nowak M., *Modification of semiconducting copper oxide thin films using ion implantation*, **VIII Congress of the Polish Vacuum Society**, July 6–7th 2022, Cracow, Poland, **poster**

- K. Ungeheuer, K.W. Marszalek, *Optical properties of copper oxides thin films implanted with chromium ions*, X**II Konferencja Techniki Próżni**, 19-21st April 2023, Ryn, Poland, **oral presentation**

- K. Ungeheuer, K.W. Marszalek, S*tructural and optical properties study of annealed ZnO thin films*, **XIII konferencja i zjazd Polskiego Towarzystwa Ceramicznego**, 25–27th November 2022, Zakopane, Poland, poster

- K. Ungeheuer, *Cr implantation of copper oxides thin films - simulation and measurements comparison*, **E-MRS Fall Meeting 2023**, 18-21st September 2023, Warsaw, Poland, **poster**

- K. Ungeheuer,, Rybak J., K.W. Marszalek, *Badania właściwości fizycznych elementów cienkowarstwowego ogniwa fotowoltaicznego do zastosowań kosmicznych*, **I Konferencja Naukowa Energetyki Rozproszonej KNER'2023**, 26th September 2023, Kraków, Poland, **oral presentation**

- G. Lewińska, K. Ungeheuer, K.W. Marszalek, *Potrójne organiczne ogniwa słoneczne – alternatywa dla krzemowych i cienkowarstwowych ogniw fotowoltaicznych*, **I Konferencja Naukowa Energetyki Rozproszonej KNER'2023**, 26th September 2023, Kraków, Poland, **poster**

- K. Ungeheuer, Rybak J., Bocirnea A.E., K.W. Marszalek, *Wpływ promieniowania protonowego na właściwości cienkich warstw tlenków metali do zastosowań w układach fotowoltaicznych*, **Szkoła Inżynierii Materiałowej, SIM 2024**, 8-9th May 2024, Kraków, Poland, **oral presentation**

- G. Lewinska, K. Ungeheuer, J. Sanetra, K.W. Marszalek, *Cupric oxide thin films as a supporting layer in binary and ternary organic cells*, **International Conference on Hybrid and Organic Photovoltaics (HOPV24)**, 13-15th May 2024, València, Spain, **poster**

- K. Ungeheuer, K.W. Marszalek, Bocirnea A.E., Galca A.C., *Thin film cupric oxide as absorbing layer for solar cells in space applications*, 1**0th International Conference On Advanced Materials ROCAM 2024**, 15-18th July 2024, Bucarest, Romania, **oral presentation**

- K. Ungeheuer, A.E. Bocirnea, K.W. Marszałek, A.C. Galca, J. Chojenka, T. Fodor, K. Vad, *Wpływ promieniowania protonowego na właściwości cienkich warstw CuO*, **XIII Konferencja Techniki Próżni**, 19-20th September 2024, Warszawa, **oral presentation**

List of Figures

2.1 Generations of photovoltaic technologies [3] 6
2.2 Band gap diagram of p-n junction (a) in dark; (b) after illumination. *E*c - conduction band, E_{v} - valence band, E_f - fermi energy level, E_{fp} - quasi-Fermi level of p-type semiconductor, E_{fn} - quasi-Fermi level of n-type semiconductor. 7
2.3 Structures of typical photovoltaic cells based on (a) crystalline Si, (b) copper indium gallium selenide (CIGS), (c) cadmium telluride (CdTe), and (d) amorphous Si. 9
2.4 Best research-cell efficiency chart by National Renewable Energy Laboratory from 2024. This plot is courtesy of the National Renewable Energy Laboratory, Golden, CO. 10

2.5 Current-voltage and power-voltage curves of a solar cell with marked maximum power point and basic parameters: I_{SC}, V_{OC}, I_{mpp}, V_{mpp}. 11
2.6 Basic structure of an all-oxide solar cell. 12
2.7 Conduction bands (orange) and valence band (blue) of commonly used oxides in all-oxide solar cells featuring two transparent electrodes, two absorber materials, and two window layer materials. 13
2.8 Pressure-temperature phase stability diagram of Cu-Cu_2O-CuO system. [34] 16
2.9 Unit cells of (a) CuO and (b) Cu_2O. 16
2.10 (a) Electronic band structure and density of states of CuO, Cu_2O and Cu_4O_3; (b) experimental Raman spectra of CuO, Cu_2O and Cu_4O_3 marked with the most important vibrational modes [49] [50]. 17
2.11 Diagram of ion implantator apparatus. 21
2.12 Diagram showing processes caused by ion implantation in the target material. . . . 22
2.13 The Air Mass Zero spectrum and the Air Mass 1.5 spectrum. 25
2.14 Normalised energy spectrum of trapped electron and proton radiation environment at Jupiter, compared to Earth [74] 26

3.1 Scheme of vacuum installation in TWINPISK stand. P1, P2, P3 - vacuum probes, DV - electromagnetic valves for dosing gases, BP - by-pass manual valves, AV - venting valves, POV - electropneumatic valves. 29
3.2 (a) Copper target with visible erosion area, (b) inside of TWINPISK deposition chamber B. 30
3.3 (a) Magnetron with mounted ZnO target and outer cover taken off, (b) plasma created during ZnO deposition. 32

4.1 Illustration of recoil cascades from two neighbouring ion beams overlapping each other. Coloured balls represent atoms of different elements: red and yellow - Cu, blue and green - O, grey - Cr. 34
4.2 Depth distribution of Cr ions and ionisation induced by ions and recoils in (a) CuO implanted with Cr ions of 15 keV energy, (b) Cu_2O implanted with Cr ions of 10 keV energy, (c) Cu_4O_3 implanted with Cr ions of 15 keV energy. 35
4.3 Visualisation of recoil cascades for CuO implanted with 15 keV Cr ions for (a) 10, (b) 100, and (c) 1000 simulated ions. Balls represent atoms: red - Cu, blue - O, grey - Cr. 36
4.4 Reflectivity curves of CuO samples (a) with different thickness before and after implantation and (b) before and after annealing. The sample implanted with 10 keV was implanted with dose of $1x10^{15}$ cm^{-2}. 37

4.5 Diffractograms of CuO samples (a) of different thickness implanted with 15 keV Cr ions, (b) all 130 nm implanted with 10 keV Cr ions of different doses. 39
4.6 Diffractograms of CuO 130 nm samples after implantation and annealing. 39
4.7 Raman spectra of 1550 nm thick CuO (a) as deposited, (b) after implantation. . . . 41
4.8 Structures used in DFT calculations (a) $Cu_{15}CrO_{16}$ and (b) Cu_7CrO_8 [95]. 42
4.9 Density of states calculated for (a) pure CuO and doped (b) $Cu_{15}CrO_{16}$, (c) Cu_7CrO_8 [95]. 43
4.10 Absorption of light calculated for (a) pure CuO and doped (b) $Cu_{15}CrO_{16}$, (c) Cu_7CrO_8 [95]. 44
4.11 Optical properties of CuO thin films implanted with Cr ions of different dose and energy: (a) absorbance of CuO films after Cr ion implantation; (b) Tauc plot for CuO films implanted with 10 keV Cr ions. (c) Absorbance of CuO after implantation and/or annealing, (d) Tauc plot of implanted and annealed CuO. The dashed line in (c) marks wavelength used to prepare plots in Figure 4.18 46
4.12 Flowchart of data analysis in spectroscopic ellipsometry [105]. 47
4.13 Model results after fitting for chosen CuO samples. Bottom layer represents interface between deposited layer and the substrate, top layer with roughness are layers that were influenced by implantation. 48
4.14 Absorption coefficient calculated from fitted model. Results for non-implanted CuO and implanted with 15 keV energy ions. 49
4.15 Refractive index and extinction coefficient of CuO thin films (a) main layer and (b) top layer of the model for sample implanted with 15 keV energy ions. 50
4.16 Psi and Delta data obtained at 70°incidence angle for samples with different dose of implantation of 10 keV energy ions (a) before and (b) after annealing. 50
4.17 Optical properties, refractive index *n* and extinction coefficient *k*, for (a) main layer and (b) top layer of non-implanted and implanted with dose $1x10^{14}$ cm^{-2} before and after annealing. 51
4.18 Pseudo refractive index maps of CuO samples before annealing (a) non-implanted CuO, implanted with 10 keV ions of dose (b) $1x10^{14}$ cm^{-2}, (c) $5x10^{14}$ cm^{-2}, (d) $1x10^{15}$ cm^{-2} [107]. 53
4.19 Pseudo refractive index maps of CuO samples after annealing (a) non-implanted CuO, implanted with 10 keV ions of dose (b) $1x^{14}$ cm^{-2}, (c) $5x10^{14}$ cm^{-2}, (d) $1x10^{15}$ cm^{-2}. 54
4.20 Maps fittings average results of CuO samples (a) before and (b) after annealing. . . 54
4.21 Total thickness three dimensional maps of CuO samples before annealing (a) non-implanted CuO, implanted with 10 keV ions of dose (b) $1x10^{14}$ cm^{-2}, (c) $5x10^{14}$ cm^{-2}, (d) $1x10^{15}$ cm^{-2}. 56

4.22 Total thickness three dimensional maps of CuO samples before annealing (a) non-implanted CuO, implanted with 10 keV ions of dose (b) 1x10^{14} cm^{-2}, (c) 5x10^{14} cm^{-2}, (d) 1x10^{15} cm^{-2}. 57
4.23 Atomic force microscopy 3D surface micrographs of CuO samples (a) non-implanted, implanted with 10 keV Cr ions of doses (b) 1x10^{14} cm^{-2}, (c) 5x10^{15} cm^{-2} and (d) 1x10^{15} cm^{-2} [109]. 58
4.24 XPS wide scans of CuO as deposited, annealed, and implanted with 10 keV energy ions of dose 1x10^{15} cm^{-2} and annealed. 59
4.25 XPS narrow spectra of (a) Cu 2p and (b) O 1s signals for samples, from bottom to top: CuO as deposited, CuO annealed, CuO implanted and annealed. 60
4.26 SNMS depth distribution of elements in CuO implanted sample[114] 62
4.27 Relative atomic concentration determined from XPS depth measurements of implanted sample and implanted annealed sample of (a) Cu, Cr and Si, (b) only Cu and Cr. 63
4.28 Depth measurements of implanted CuO for signals of (a) Si 2p, (b) Cu 2p, (c) Cr 2p. 63
4.29 Depth measurements of implanted and annealed CuO for signals of (a) Si 2p, (b) Cu 2p, (c) Cr 2p. 64
4.30 Diffractograms of Cu_2O samples non-implanted and implanted with three different doses. 66
4.31 Diffractograms of Cu_2O samples before and after annealing in Ar (a) non-implanted sample, implanted with (b) dose 1, (c) dose 2, (d) dose 3. 67
4.32 Diffractograms of various thickness Cu_4O_3 thin films before and after implantation with Cr ions. 67
4.33 X-ray reflectivity curves for (a) Cu_2O and (b) Cu_4O_3 samples. 68
4.34 Optical properties of Cu_2O thin films implanted with Cr ions of different dose and energy: (a) absorbance of Cu_2O films after Cr ion implantation; (b) Tauc plot for Cu_2O films implanted with 10 keV Cr ions, and after annealing (c) absorbance of implanted films and two spots of non-implanted sample, (d) Tauc plot for implanted and annealed samples. 69
4.35 Fit results of SE data for Cu_2O samples deposited at silicon (a) for representative points and (b) for the whole maps [109]. The data points connected with solid line represent the mean square error (MSE) values. 70
4.36 (a) Refractive index and (b) extinction coefficient calculated from model fitting at representative points of Cu2O samples, the data is for main layer #2 [116]. 71
4.37 3D maps of total thickness parameter calculated Cu_2O samples (a) non-implanted, (b) dose 1, (c) dose 2, and (d) dose 3 [116] 72

4.38 SE measurement data, Psi and Delta, for Cu_2O samples (a) before and (b) after annealing measured at 65°angle. (c) Psi and (d) Delta for non-implanted sample measured at various angles. 73
4.39 (a) Spectroscopic ellipsometry model fitting results for Cu_4O_3, and determined (b) absorption coefficient, refractive index and extinction coefficient for (c) main and (d) top layer of the model [118]. 75
4.40 Maps of pseudo refractive index parameter for Cu_2O samples (a) non-implanted and implanted with (b) dose 1, (c) dose 2, (d) dose 3 [107]. 76
4.41 SE measurement data, Psi and Delta, for Cu_2O samples (a) before and (b) after annealing measured at 65°angle. (a) Psi and (b) Delta for non-implanted sample measured at various angles. 77
4.42 Total thickness three dimensional maps of Cu_4O_3 (a) non-implanted and (b) implanted samples. 78
4.43 Atomic force microscopy 3D surface micrographs of Cu_2O samples (a) non-implanted, implanted with 10 keV Cr ions of doses (b) $1x10^{14}$ cm^{-2}, (c) $5x10^{14}$ cm^{-2} and (d) $1x10^{15}$ cm^{-2}[109]. 78
4.44 Wide XPS scans for Cu_2O samples, the most important signals from detected elements are marked on the figure. 79
4.45 Cu LMM Auger spectra for Cu_2O samples. 80
4.46 (a) Cu 2p and (b) O 1s spectra for Cu_2O samples. 81

5.1 Diffractograms of as deposited CuO and sample irradiated with protons CuO:H+, the most important peaks for CuO are identified. 84
5.2 Raman spectra for as deposited CuO and irradiated sample CuO:H+, for each film three vibrational modes are assigned. 85
5.3 Absorbance of CuO thin films before and after proton irradiation. 85
5.4 Spectroscopic ellipsometry data (a) Psi and (b) Delta for CuO samples before and after proton irradiation. 86
5.5 Refractive index *n* and extinction coefficient *k* of as deposited CuO and irradiated sample CuO:H+. 86
5.6 Spectroscopic ellipsometry data (coloured lines) and fit lines (dotted lines) for (a) as deposited CuO and (b) irradiated sample CuO:H+. 87
5.7 XPS wide scan of CuO and CuO:H+ samples. 88
5.8 Narrow scan for Cu 2p (a) and O 1s (b) signal with fitted line and components. Bottom line is for non-irradiated sample, line in the top part for irradiated sample. . 89
5.9 X-ray diffractograms of ITO and AZO thin film before and after proton irradiation. 90
5.10 Transmittance measured with spectrophotometry of (a) ITO and (b) AZO samples. 91

5.11 Refractive index *n* and extinction coefficient *k* of (a) ITO and (b) AZO samples determined from ellipsometry data fitting. 92
5.12 Fitting results of dielectric function model to ellipsometry data for AZO and ITO samples, the values are average of map points. 92
5.13 SEM images of samples (a) AZO, (b) AZO:H+, (c) ITO, (d) ITO H+. 93
5.14 SEM image of a precipitate on AZO sample surface and atomic composition measured with EDS for probing point (a) at the precipitate and (b) at the film surface. . 94
5.15 Total thickness three dimensional maps of samples (a) AZO, (b) AZO:H+, (c) ITO, (d) ITO H+. 95
5.16 Pseudo refractive index maps of samples (a) AZO, (b) AZO:H+, (c) ITO, (d) ITO:H+. 96
5.17 Narrow XPS scans with fit lines and distinguished components for AZO samples (a) Al 2p, (b) Zn 2p $_{3/2}$, (c) O 1s and for ITO samples (d) In 3d, (e) Sn 3d $_{5/2}$ (f) O 1s. In all figures the bottom graph is for non irradiated sample and graph in the top for irradiated sample. 98

6.1 Scheme of solar cell preparation. 101
6.2 I-V curve for cell no 36 measured in dark and under illumination. 102
6.3 I-V curves for cells no. (a) 2 and (b) 27. 102
6.4 SEM image of cell 27 cross section. 103

List of Tables

2.1 Structure and performance of chosen all-oxide solar cells. 15
2.2 Calculated frequencies of all vibrational modes for Cu_2O and CuO, and only allowed modes for Cu_4O_3 [50]. 18

3.1 Copper oxides thin films deposition parameters. 31

4.1 Parameters of ion implantation experiments and samples that were implanted. . . . 34
4.2 Thickness of CuO films determined from X-ray reflectivity measurements. 38
4.3 Calculated lattice parameters of CuO samples after Cr ion implantation and annealing. 40
4.4 Energy band gap determined using Tauc plot method for CuO samples. 45
4.5 Energy of transitions in CuO and fitted positions of oscillators. 49

4.6 Spectroscopic ellipsometry data fitting results for samples after implantation with 10 keV energy Cr ions and/or annealing. 52
4.7 The relative contribution of components for O 1s signal for CuO as deposited, after annealing and after implantation and annealing. 61
4.8 Sheet resistance of CuO thin film samples. 62
4.9 Transition energies of Cu_4O_3 and fitted Tauc-Lorentz oscillators position energies [118]. 74
4.10 The relative contribution of components for O 1s signal for Cu_2O annealed samples. 80

5.1 The relative contribution of components for O 1s signal for CuO as before and after proton irradiation. 88
5.2 The relative contribution of components for Zn 2p, Al 2p, In 3d, Sn 3d and O 1s lines for transparent conductive oxides films before and after proton irradiation. . . 99